MATHEMATICAL AND COMPUTATIONAL MODELING IN BIOMEDICAL ENGINEERING

by

Patrick A. Giolando

A Thesis

Submitted to the Faculty of Purdue University

In Partial Fulfillment of the Requirements for the degree of

Master of Science in Mechanical Engineering

School of Mechanical Engineering

West Lafayette, Indiana

August 2021

THE PURDUE UNIVERSITY GRADUATE SCHOOL
STATEMENT OF COMMITTEE APPROVAL

Dr. Steven T. Wereley, Chair

School of Mechanical Engineering

Dr. Tamara L. Kinzer-Ursem

Weldon School of Biomedical Engineering

Dr. Arezoo M. Ardekani

School of Mechanical Engineerin

Approved by:

Dr. Nicole L. Key

ACKNOWLEDGMENTS

First, a special thank you to my advisor Dr. Kinzer-Ursem for her years of guidance and wisdom, as well as the warm welcome into her lab group. My love for mathematical and computational modeling would have not developed as it had without her guidance. I would also like to give many thanks to my advisor Dr. Wereley, I always enjoyed our duality of the experimentalist and the numericist. I would also like to thank Dr. Grafenstein for his support in the earliest years of my academic career, and his encouragement in the development of my first mathematical and computational model. I would like to thank my research professors Dr. Solorio for both his support through my academic development and guidance through these trying research projects. I would like to thank my committee members Dr. Kinzer-Ursem, Dr. Wereley, and Dr. Ardekani on their insightful advice on the development of this thesis.

I would also like to thank Dr. Rayz and Dr. Babbs for their helpful and inspirational conversations on fluid mechanics. I would like to thank my first academic sibling Barrett whom I have spent way too many over-caffeinated late nights preparing posters and talks with. I will certainly miss the insanity of it all. I would also like to thank my colleagues Hui and Kelsey without their hard work and dedication these research projects would have not been possible. I would like to thank my parents Dr. Giolando and Dr. Kirschbaum for their unwavering support of my health and academic career. I have a great respect for them. Finally, I would like to thank Sabrina for maintaining my sanity through the never-ending late nights these past few years.

Without a doubt I have been extremely fortunate to be surrounded by such a collaborative community of scientists and engineers, and it has been my honor to work with and for them.

TABLE OF CONTENTS

LIST OF TABLES

LIST OF FIGURES

ABSTRACT

Mathematical and computational modeling allow for the rationalization of complex phenomenon observed in our reality. Through the careful selection of assumptions, the intractable task of simulating reality can be reduced to the simulation of a practical system whose behavior can be replicated. The development of computational models allow for the full comprehension of the defined system, and the model itself can be used to evaluate the results of thousands of simulate experiments to aid in the rational design process.

Biomedical engineering is the application of engineering principles to the field of medicine and biology. This discipline is composed of numerous diverse subdisciplines that span from genetic engineering to biomechanics. Each of these subdisciplines is concerned with its own complex and seemingly chaotic systems, whose behavior is difficult to characterize. The development and application of computational modeling to rationalize these systems is often necessary in this field and will be the focus of this thesis.

This thesis is centered on the development and application of mathematical and computational modeling in three diverse systems in biomedical engineering. First, computational modeling is employed to investigate the behavior of key proteins in the post-synapse centered around learning and memory. Second, computational modeling is utilized to characterize the drug release rate from implantable drug delivery depots, and produce a tool to aid in the tailoring of the release rate. Finally, computational modeling is utilized to understand the motion of particles through an inertial focusing microfluidics chip and optimize the size selective capture efficiency.

1. INTRODUCTION

Computational modeling is the use of computer algorithms to simulate complex systems, whose behavior may be difficult or impossible to predict. However, in developing a computational model it is necessary to first carefully define the system whose behavior is to be simulated and derive a well posed mathematical model to capture the behavior. Although computational models are developed for numerous reasons, this work is mainly concerned with two motives: to enhance the understanding of the behavior of a complex system, and to develop a tool for the acceleration of the rational design process.

Mathematical modeling is the utilization of mathematical principles to capture the behavior of observed phenomenon. Although, our observable reality is often extraordinarily complex, carefully chosen assumptions allow for the complexity of the system to be reduced to a practical form. With the necessary assumptions considered, the system can often be represented by a system of mathematical equations formulated from fundamental principles. The process of building these mathematical models requires an iterative approach of increasing complexities until the behavior of the observed system is fully captured. The process of developing the model often provides numerous insights to the modeler on the underlying behavior of the system that may not be intuitive when simply observing the system. The final product of mathematical modeling is often a large system of equations whose behavior is less intuitive than even the observed phenomenon and cannot be solved analytically.

When the analytical solution is difficult or even impossible to derive, numerical methods are employed to evaluate the discrete form of the continuous equations. Numerical methods are a family of techniques to evaluate mathematical expressions a few examples include: approximation theory; interpolation and extrapolation; linear algebra; optimization of nonlinear equations; quadrature and orthogonal polynomial; ordinary and partial differential equations; and integral equations [1]. Of particular interest is the use of numerical methods to convert a system of ordinary and partial differential equations into a system of algebraic equations. The large system of algebraic equations can then be solved with linear algebra, however, crunching these equations by hand is impracticable. To build and solve these massive systems of algebraic equations computational models are developed.

Although computational algorithms have greatly accelerated the development and use of numerical methods in the last century, numerical methods significantly predate the invention of computers by several millennium. One of the earliest uses of numerical algorithms includes a root finding algorithm recorded on the Ahmes Papyrus dated 1800-1600 BCE [2]. The field of numerical methods continued to grow over the next few millennia, however, many of the greatest advancements occurred in the 18^{th} and 19^{th} centuries due to a handful mathematical giants. Of these giants the most notable are Gottfried Wilhelm Leibniz, Isaac Newton, Leonhard Euler, Joseph-Louis Lagrange, Carl Friedrich Gauss, and Carl Gustav Jacob Jacobi for whom many important modern numerical algorithms are named after.

With the development of calculus in the 17^{th}-18^{th} century mathematical modeling was greatly expanded in numerous fields of physics, science, and engineering. Numerical methods for the approximation of ordinary and partial differential equations allowed for the modeling of more complex phenomenon. The finite difference approximations of derivatives introduced by Brook Taylor became an integral tool in approximating the solution for these numerical differential equations [3]. The use of finite difference methods to evaluate models in the 19^{th} century led to the successful modeling of solid mechanics, diffusion, heat transfer, and electricity/magnetism. With the work of Olga Ladyzhenskaya and Alexandre Chorin in the late 20^{th} century this was expanded to include complete models of fluid mechanics [4].

Mathematical and computational modeling allows for the full comprehension of complex systems through the iterative process of model development. The final product is a computational model, which is used to accelerate the rational design process. The process begins with the observation of a complex phenomenon in reality, which prompts the careful selection of assumptions to reduce the system to a tractable form. Next fundamental principles, often conservation laws, are utilized to develop constitutive equations that describe the reduced system. Based on the governing physics relevant numerical methods are selected and a computational model is built. However, this computational model is no more than an educated guess for the behavior of the observed system. The accuracy of the model must be verified by quantitatively comparing the model to experimental data relevant to the observed phenomenon.

If the computational model captures the behavior of the observed system than the model is complete. However, if the computational model does not capture the behavior of the observed system, then the modeler must return to the definition of the reduced system and either relax the

assumptions or expand the system by considering the new aspects of the phenomenon. This begins the cycle of modeling anew. Notably, when modeling complex phenomenon it is often necessary to create subcomponents, or portions of the observed phenomenon that can be independently developed and verified prior to a substantial increase in model complexity.

The discipline of biomedical engineering and the application of engineering principles to biology and medicine produces numerous complex systems that evade comprehension. These seemingly chaotic systems require the application of mathematical and computational modeling to fully understand the nature of their behavior.

In this body of work, we evaluate multiple complex systems that have either evaded intuitive comprehension or whose behavior is difficult to predict. Through the formulation of mathematical models and development of computational models a deeper understanding of the system is developed along with a tool for potential design optimization.

This dissertation is organized into three parts:

Chapter 2: We develop a computational model for the interactions of postsynaptic proteins involved in neuronal plasticity, as well as the impact of genetic mutation of a key synaptic protein, synGAP. Although, the detrimental effect of a synGAP mutation has been observed by a couple of research groups, there is a deficiency of computational modeling to fully understand the impact of a synGAP knockdown. Our model was not only able to predict the impact of synGAP regulation on the ability of the synapse to regulate its connectivity, but the model was also able to suggest therapeutic targets to restore the bidirectionality of the system.

Chapter 3: We developed a mathematical and computational model for predicting the drug release rate from implantable bioresorbable drug delivery depots. Building upon decades of research on the modeling of degrading/swelling polymer implants, the current study progresses previous models in four aspects: (a) consideration of the impact of phase inversion on the drug release of both microspheres and ISFIs; (b) investigation of observable phenomena such as complex implant geometries, nonuniform drug distribution, and swelling of larger implants; (c) explicit modeling of the production and transport of H^+ ions, which catalyze the degradation and diffusion of acid as

separate processes; (d) inclusion of a full probability model for the distribution of oligomers produced from random chain scission as proposed by Flory.

Chapter 4: We developed computational modeling for the simulation of the inertial focusing of particles in a microfluidics chip. Advanced numerical methods were utilized to model the two-way coupled interaction between the particle and the fluid domain to capture the inertial focusing behavior of the particles. The model was used to investigate the behavior in an expanded channel microfluidics chip, which utilizes the formation of microvortices to size selectively capture particles. The computational model was verified and used to aid in the design process of optimizing the capture efficiency of the microvortices.

1.1 References

[1] C. Brezinski and L. Wuytack, "Numerical Analysis," ed: Elsevier B.V, 2001, pp. 1-40.

[2] G. Robins, *The Rhind mathematical papyrus : an ancient Egyptian text*. New York: Dover, 1990.

[3] K. Andersen, *Brook Taylor's Work on Linear Perspective: A Study of Taylor's Role in the History of Perspective Geometry. Including Facsimiles of Taylor's Two Books on Perspective*. Springer, 2012.

[4] A. J. Chorin, "Numerical Solution of the Navier-Stokes Equations," *Mathematics of computation*, vol. 22, no. 104, pp. 745-762, 1968, doi: 10.1090/S0025-5718-1968-0242392-2.

2. CaM/CaMKII MEDIATED REMODELING OF PDZ DOMAINS AND THE INHIBITORY INFLUENCE OF SYNGAP IN THE POST-SYNAPTIC DENSITY

2.1 Abstract

Approximately, 1 in every 60 children in the United States have been diagnosed with Autism Spectrum Disorder (ASD) [1]. Of the hundreds of genes associated with ASD, those most highly correlated with the disorder produce proteins involved in neuronal synapse function, including the mutation of SYNGAP1 gene. Equally highly expressed is the scaffolding protein PSD-95 a major constituent of the post-synapse, comprised of three PDZ-domain binding "slots", which anchor transsynaptic protein domains and anchor mobile AMPA receptors to the postsynaptic density. The Ras-GTPase activating protein synGAP has been found to occupy up to 10-15% of the scaffold's PDZ-domains at any time, potentially restricting the binding of other proteins to these sites including TARPs, Neuroligin, and LRRTM proteins involved in regulating synaptic functions. The binding of synGAP to PDZ domains is regulated by Ca^{2+} activated Calmodulin and Ca^{2+}/calmodulin-dependent protein kinase II (CaMKII). Although, the phenotypical impact of SYNGAP1 loss-of-function mutations have been observed by several labs, there still lacks computational modeling work to fully understand the impact of a synGAP knockdown on the system. To gain a full understanding on how synGAP competes with other synaptic proteins for binding to PDZ domains, we designed a computational model that captures the frequency dependent binding of synGAP and other key synaptic proteins (TARP, LRRTM, and Neuroligin) with the PDZ domains of PSD-95. Our model predicts that SYNGAP1 loss-of-function mutations result in the dysregulation of the competition for PSD-95 and leads to an over saturation of TARP anchored to PSD-95 at the post-synaptic density. Phenotypically, this has been observed as an uncontrolled enlargement of excitatory synapses without a mechanism for down regulation. Furthermore, the model suggests that the bidirectionality of the system can be recovered through the introduction of a PSD-95 inhibitor.

2.2 Introduction

Formation and development of memory relies on the structuring of neuronal connections and their ability to strengthen and weaken. Neuronal plasticity requires the synaptic connection between individual neurons to be able to both strengthen and weaken in response to varying external stimuli [1, 2]. The strength of a synaptic connection is often controlled on the molecular level by the rearrangement of key proteins in the post-synaptic density (PSD) [3, 4]. The recruitment and activation of N-methyl-D-aspartate receptor (NMDAR) and α-amino-3-hydroxyl-5-methyl-4-isoxazole propionic acid receptor (AMPAR) is necessary for the modulated response of the post synapse [4].

The continual strengthening of a synaptic connection (long-term potentiation or LTP) and weakening (long-term depression or LTD) is a calcium dependent mechanism. During LTP and LTD, the NMDARs are activated and allow for an influx of calcium, originating from the pre-synapse, into the post-synapse which heavily impacts the upregulation and downregulation of signaling pathways in the post-synapse. While both pathways require the increase of calcium concentration in the PSD from basal conditions, they have opposing mechanisms and outcomes, which are regulated by the exact frequency of the calcium stimulation. A low frequency stimulation of calcium representative of LTD will lead to a decrease in AMPARs located at the head of the PSD, while a high frequency calcium stimulation representative of LTP will lead to an increase in AMPARs, Fig 1.

Recruitment of AMPAR includes the insertion of the receptor into the post-synaptic membrane, the diffusion across the membrane, and the trapping of the receptor at the head of the synapse where it functions to regulate ion conductance. The anchoring of AMPARs occurs through the binding of its auxiliary Transmembrane AMPAR Regulatory Protein (TARP), which has a high affinity for AMPAR, to PSD-95 a major scaffolding protein constitutively located in the PSD. The binding of TARP to PSD-95 acts to reduce the mobility of the complex and anchor the complex to the PSD. PSD-95 also acts to bind and localize other synaptic regulatory proteins including Leucine Rich Repeat TransMembrane (LRRTM) and Neuroligins to the PSD. PSD-95 has three PDZ binding domains highly competed for. The composition of proteins bound to these PDZ domains dictate the strength of the synaptic connection.

SynGAP is found in the post-synapse at high concentrations and has a high binding affinity for the PDZ domains of PSD-95, experimental studies have found synGAP binding up to 15% of

these domains at a time [5, 6]. SynGAP severely reduces the ability for other proteins, especially TARPs, to bind to the PSD-95 through competitive inhibition. Two calcium dependent mechanisms for reducing the amount of synGAP bound to PSD-95 have been studied by Kennedy et al. [7, 8]. The binding of Ca^{2+}/Calmodulin (Ca^{2+}/CaM) to synGAP has been found to reduce synGAP's binding affinity for PDZ domains, and the phosphorylation of synGAP by Ca^{2+}/Calmodulin-Dependent Protein Kinase II (CaMKII) results in a massive decrease in synGAPs ability to bind to PSD-95 [7]. This decrease in affinity for PSD-95 results in a dispersion of synGAP from the PSD [9]. Additionally, Choquet et al. have observed that the phosphorylation of the C-tail on TARP leads to an increase in its binding affinity of PSD-95 [10].

The relevant kinase and phosphatase cascades involved in the upregulation and downregulation of TARP bound to PSD-95 include the involvement of seven other CaM binding proteins (Adenylyl Cyclase type I (AC1), Adenylyl Cyclase type VIII N-terminus (AC8-Nt), Adenylyl Cyclase type VII C_{2b} domain (AC8-Ct), calcineurin (PP2B), Myosin Light Chain Kinase (MLCK), Neurogranin (Ng), Nitric Oxide Synthase (NOS), and Phosphodiesterase type I (PDE1); as well as Phosphodiesterase type IV (PDE4), Protein Phosphatase 1 (PP1), Inhibitor 1 (I1), Protein Kinase A (PKA), and Protein Phosphatase 2 (PP2A), see Fig 4.

The deregulation of the mechanisms behind the recruitment of AMPAR have been linked to several disease states. The most relevant to this study are the loss-of-function mutation of SYNGAP1 as well as the dysregulation of SYNGAP1. Deregulation of synGAP leads to a loss of the excitatory/inhibitory balance, which has been linked to developmental disorders including intellectual disability (ID) and autism spectrum disorder (ASD) [11-16]. Kennedy et al. independently evaluated the impact of synGAP's GAP domain and the PDZ domain-binding motif on spine formation in a synGAP knockout (ko). The synGAP ko led to premature development of dendritic spine synapses. The ability for synGAP to compete for PSD-95 binding domains was found to be necessary in the development of this abnormality [7, 17].

To understand how frequency-dependent Ca^{2+} flux influences the system, we designed a computational model that captures the dynamic activation of kinase and phosphatase cascades and the impact on the remodeling of the proteins bound to the PDZ domains of PSD-95. Of particular interest is synGAP's regulation of the ability for TARP to bind and anchor AMPA receptors at the PSD. The model is also used to predict the impact of loss-of-function mutation and dysregulation

of SYNGAP1 on the system, and the subsequent loss of typical LTP and LTD reactions to characteristic calcium frequency stimulations.

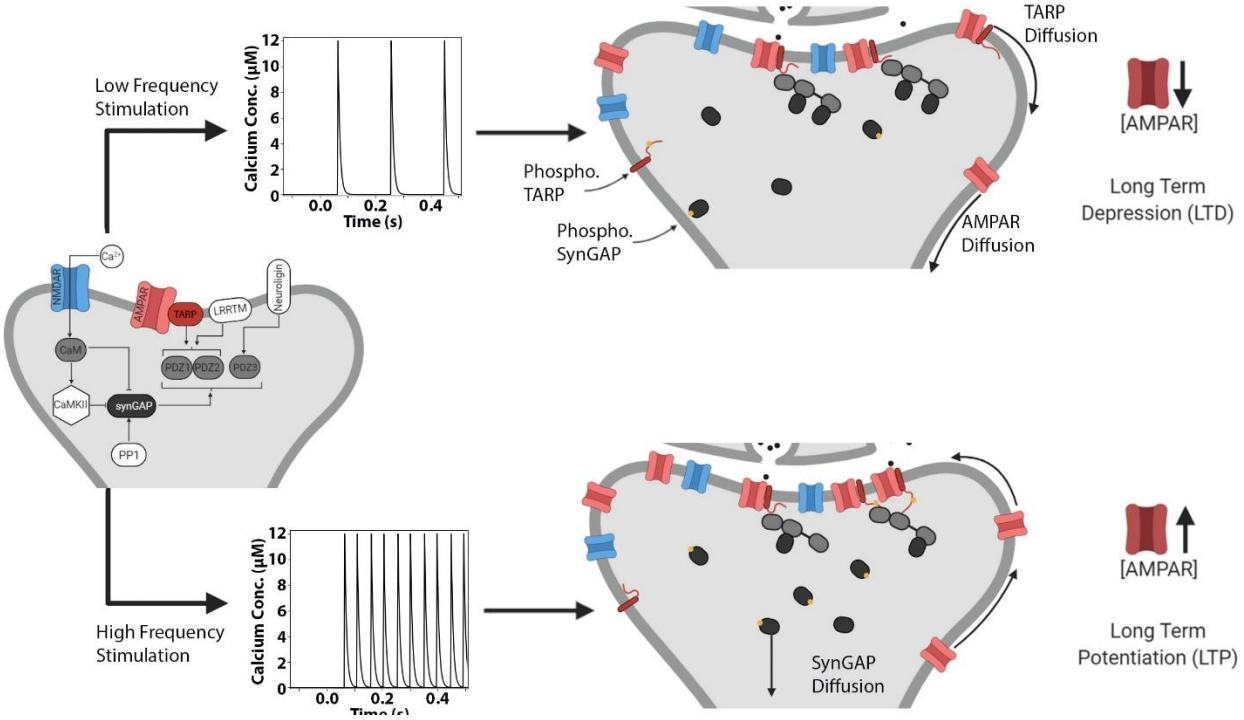

Figure 2.1. Neuronal Plasticity. During low frequency stimulations (upper pathway) lower concentrations of TARP are bound to PSD-95 and subsequently fewer AMPARs are anchored at the PSD resulting in the diffusion out of the PSD, characteristic of LTD. During high frequency stimulations (lower pathway) higher concentrations of TARP are bound to PSD-95 and subsequently more AMPARs are anchored at the PSD, characteristic of LTD.

2.3 Materials and Methods

2.3.1 Model Development

The dynamic system's interactions were modeled deterministically according to mass action kinetics. The resulting system of ordinary differential equations (ODEs) was numerically solved in Python 3.7. The model is parameterized using literature values. Model code is included in supplement and has been archived at [Purdue Archive].

2.3.2 Frequency Stimulation

To simulate low frequency (10 Hz) and high frequency (100 Hz) stimulations, calcium was introduced into the model by the time-dependent forcing function

$$A * e^{-d(t)} = III_T(t)$$

where A is the amplitude, d is the decay rate of a single calcium spike, * indicates the mathematical operator for convolution and III_T describes the sampling function for a period T.

Calcium stimulations were varied by frequency, and consequently duration. The total amount of calcium entering the system was maintained constant. The peak widths of individual calcium spikes were simulated as 30 ms [18, 19], Fig 2.

2.3.3 Sensitivity Analysis

Model Output

As a primary model output, we evaluated the change in concentration of TARP bound to PSD-95 at any of the scaffolding protein's three PDZ domains over time. This metric was chosen as an analogue for short term LTP/LTD by way of AMPAR localization within PSD.

Two scoring regimes were developed to fully understand the impact of knocking down synGAP on the rearrangement of proteins bound to PSD-95, specifically TARP:

Score 1: Change in TARP bound to PSD-95 normalized to the steady state concentration of TARP bound to PSD-95 for wildtype (WT) conditions.

$$Score1_{[SG]} = \frac{\frac{\sum_0^N [TA{:}\,PSD-95]}{N} - \mu_{SS,WT}}{\mu_{SS,WT}}$$

Score 2: Change in TARP bound to PSD-95 normalized to the steady state concentration of TARP bound to PSD-95 for knockdown conditions.

$$Score2_{[SG]} = \frac{\frac{\sum_0^N [TA{:}\,PSD-95]}{N} - \mu_{SS,[SG]}}{\mu_{SS,[SG]}}$$

The concentration of TARP bound to PSD-95 was integrated over a time window of 100 seconds for consistency between vary frequencies of stimulation. Score 1 gives insight into the impact of synGAP mutation on the overall increase and decrease of the concentration of TARP

bound. Meanwhile, Score 2 gives insight into the impact of synGAP mutation on the frequency dependent increase and decrease of TARP bound to PSD-95.

Analysis Methods

Time varying sensitivity indices for key protein concentrations and kinetic rates were calculated locally by derivative-based sensitivity analysis. Sensitivity indices were also calculated globally by partial rank correlation coefficient (PRCC) determination [20] and the variance based Sobol method [21].

In the absence of independent parameter verification by at least two sources, the upper and lower bounds for a given species' concentration were set at a factor of two (2) above and below our best estimate. For kinetic and catalytic rates, the upper and lower uncertainty bounds were set at a factor of five (5) above and below our best estimate. For local sensitivity analysis, model parameters were linearly sampled along the range of uncertainty. For the PRCC and Sobol methods, parameter spaces were defined by uniform Latin hypercube sampling (LHS) and Saltelli low-discrepancy sampling [22], respectively.

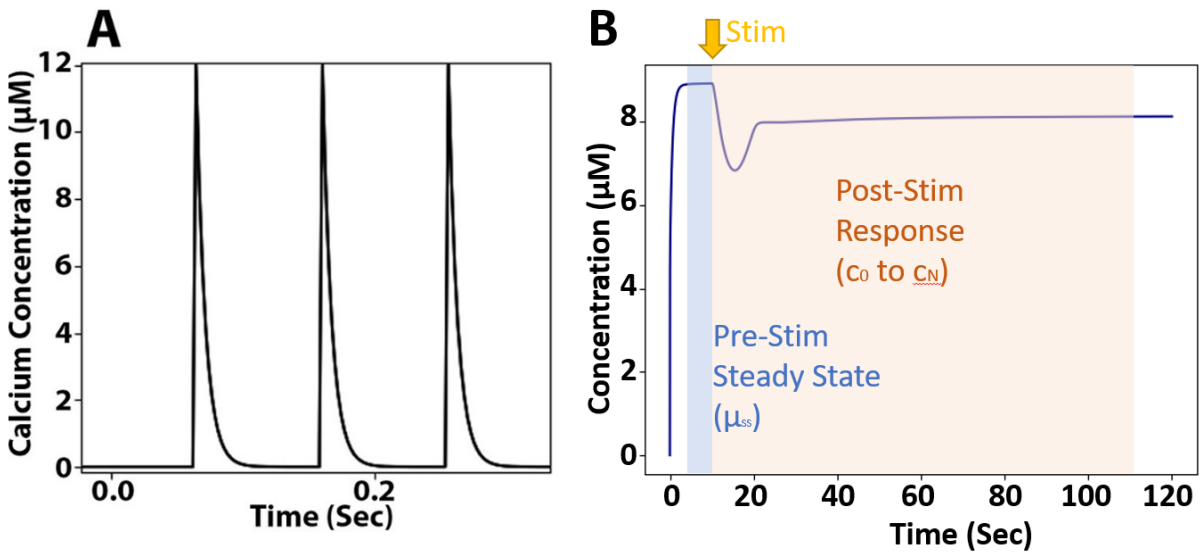

Figure 2.2. Defining LTP and LTD. (A) Input function for a 10 Hz calcium stimulation; stimulation continues for a 100 pulses. (B) Example of the response of the concentration of TARP bound to PSD-95 due to a 10 Hz stimulation. Both scoring mechanisms include an integration of the concentration of TARP bound to PSD-95 in the Post-Stim Response window, labeled above. The key difference in the scoring mechanisms is whether the concentration is normalized to the Pre-Stim Steady State (μ_{SS}) of the WT or of the disease state.

2.4 Results

2.4.1 Model Structure

CaM binds up to four Ca^{2+} ions, which occurs through cooperative binding, and has the direct impact of inducing a conformational change. Depending on the saturation level the binding rate of CaM for different binding partners varies dramatically. A nine-state model would be required to monitor each Ca^{2+} ion, however, Romano et al., determined that due to the highly cooperative binding of calcium the nine-state model could be reduced to a four-state model with negligible error [23]. This project continues the work from Romano et al. with a four state model of CaM.

CaMKII's dodecameric structure allows the holoenzyme to bind and phosphorylate up to twelve proteins at a time with each subunit of CaMKII containing a kinase, regulatory, and hub domain. While CaMKII has a low phosphorylation rate in its closed conformation it has two mechanisms for activation: short term activation is induced by the binding of Ca^{2+}/CaM to the regulatory domain and long term activation is generated by the phosphorylation of the Thr-286 site in the regulatory domain. This phosphorylation is often the product of autophosphorylation by another kinase domain on the holoenzyme. Monitoring the position and state of each subunit leads to a combinatorial nightmare to model, however, Romano et al. developed an ODE model that does not account for space and a simplification can be made [23]. The model assumes that CaMKII can be modeled as a population of monomers that have the ability to exist in each of the above states. The model does not consider physical restrictions in the autophosphorylation process and assumes a homogeneous mixture of these units.

Modeling efforts centered around first simulating *in vitro* data sets focused on quantifying the impact of CaM and CaMKII on synGAP's ability to bind to PSD-95, and then on simulating *in vivo* conditions to predict synGAP's role in regulating the binding of TARP to PSD-95. The *in vitro* model was parameterized with previously determined rates from literature, or previous computational work [7, 23, 24]. The model was then expanded to include significant proteins involved in binding to either CaM or PSD-95, as well as those regulating kinase and phosphatase activity, in the PSD, Fig 4. This *in vivo* model was parameterized with rates determined empirically in previous literature, calculated using thermodynamic principle of microscopic reversibility in previous studies, or from previous computational work [7, 23, 24].

2.4.2 In Vitro Model

In Vitro Modeling

Recent work by the Kennedy lab produced a series of *in vitro* experiments relating to the binding of synGAP to PSD-95, as well as data for the impact of binding and phosphorylation by CaM and CaMKII on synGAP's affinity for PSD-95. Our study utilized the empirical data to parameterize the model for the interactions between synGAP, CaM, CaMKII, and PSD-95 [7, 8, 23, 24]. Then we verified our *in vitro* model with additional data sets from Kennedy et al. [7].

In Vitro Model Parameterization

We first designed a model to replicate several *in vitro* experiments with CaM, synGAP, CaMKII, and Ca^{2+}, Fig 3a, to verify the accuracy of our synGAP model. The bulk of the model was parameterized by previous studies [7, 8], however, kinetic rates for the binding of CaMKII/CaM with synGAP, and the phosphorylation of synGAP by CaMKII was unknown. The rate for CaMKII/CaM binding to synGAP was approximated by our best approximation, which was the measured binding rate for pS831GluR1 and CaMKII/CaM. The phosphorylation rate of synGAP was evaluated empirically by reacting synGAP with Ca^{2+}/CaM/CaMKII and measuring the phosphate concentration over a time course of ten minutes [7]. The experimental setup was replicated *in silico*, and the rate constant was found with the least squares method, see Fig 3b.

In Vitro Model Verification

Following the parameterization, we sought to verify the impact of CaM binding and CaMKII phosphorylation on the binding affinity of synGAP for PDZ domains by replicating the empirical data, Fig 3 [7]. Experimental data for the association of synGAP was collected with three different setups. SynGAP was either incubated in CaM/Ca^{2+}, CaM/Ca^{2+} and CaMKII, or alone as a control before being introduced to PDZ domains [7], see Fig 3c. The model was able to predict the impact of CaM with a relative error of 3.144%, and the impact of CaM/CaMKII with a relative error of 7.994%, which is well within experimental error.

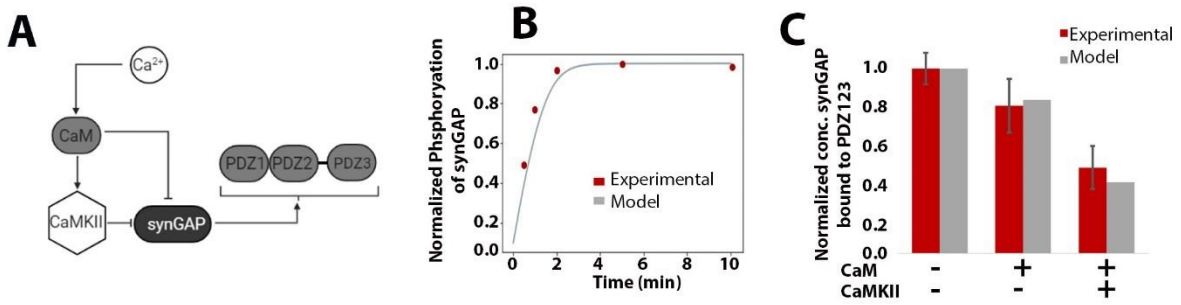

Figure 2.3. *In Vitro* Modeling. (A) Model design reflecting empirical setup to verify the accuracy of the synGAP model. (B) Model parameterization of the phosphorylation rate of synGAP [7]. (C) Simulation was compared to experimental data collected by Kennedy et al. for the impact of the CaM and CaM/CaMKII on the ability of synGAP to bind with PDZ domains [7]. The concentration of synGAP bound to the PDZ domains was normalized by the control, which quantified the concentration of synGAP bound to PDZ123 with neither CaM or CaMKII in the solution.

2.4.3 In Vivo Model

In Vivo Modeling

With the synGAP model parameterized and verified the model was expanded to replicate in vivo conditions. The addition of twelve highly expressed proteins in the PSD involved in several kinase and phosphatase cascades as well as three highly expressed transmembrane proteins that compete with synGAP for the binding of PSD-95 required a full parameterization from literature, see Fig 4.

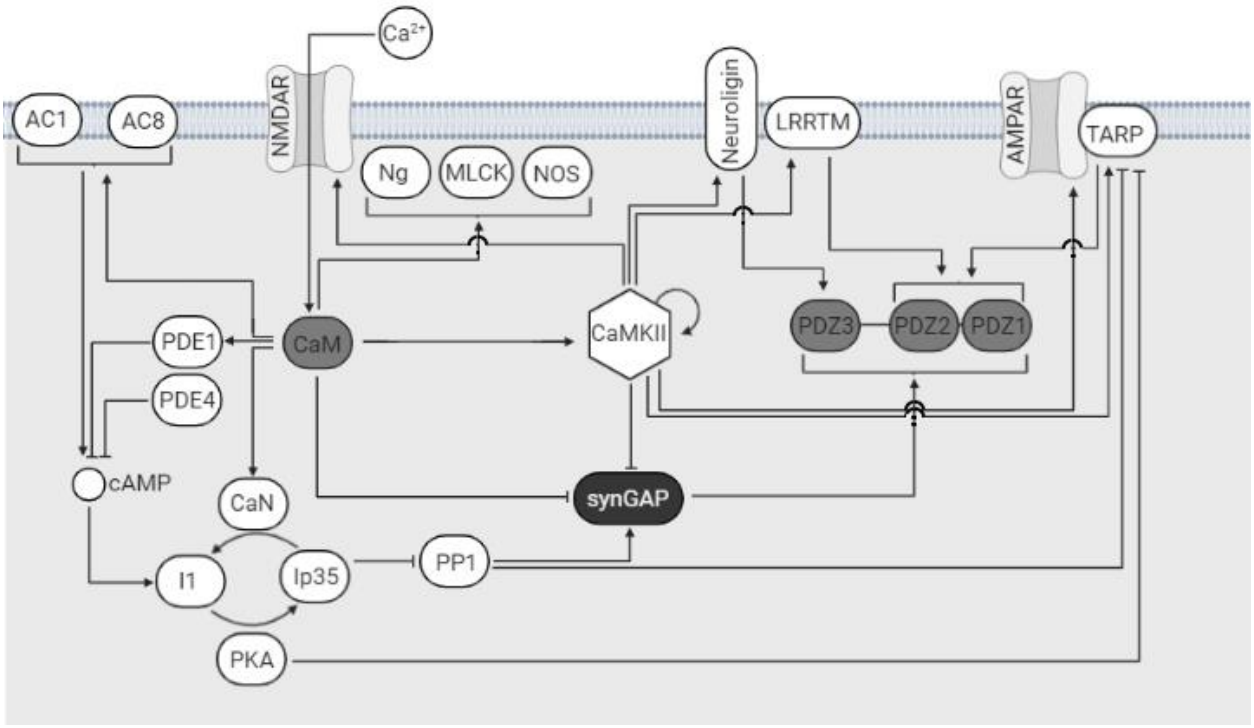

Figure 2.4. ***In Vivo*** **Modeling**. Schematic of the protein interaction among eighteen abundant PSD proteins. Interactions are modeled with a system of ODEs derived from mass action law, reaction rates are assumed linear. Not shown in the figure is the phosphorylation of AMPAR by CaMKII and PKA.

In Vivo Model Parameterization

An extensive literature review was conducted to populate the mode. Initial concentration of each of the proteins in Fig 4 are displayed in Table 1. Parameter values for kinetic rates are displayed in Table S1.

Table 2.1. Initial concentration of unbound proteins.

Species Abbrev.	Concentration (μM)	Ref.
ATP	2000	[25]
CaM	10	[25]
AC1	42 2	[23] [26-28]
AC8	42 2	[23] [26-28]
CaN	4 0.5 1 3	[25] [23] [29] [26, 30, 31]
KII	20 20-50	[25] [32-35]
MLCK	5	[23]
NG	52	[23]
NOS	1	[23]
GluA1	11.6 9.5136	[23] [24]
PSD-95	100	[36]
SG	100 30-50	[3] [7]
TA	19	[37, 38]
LR	11.6	[37]
NE	7.1 16.6	[37] [39]
PP1	5 0.556 2	[25] [40] [41, 42]
I1	0.507	[40]
AMP	0.495	[40]
cAMP	0.1	[24]
PKA	1.2 1 1.763	[25] [29] [40]
PKAi	0.259 2	Hao 2006 [43], Colledge 2000
PDE1	4 2.25 3.45-4	[25] [29, 40]
PDE4	2 3 2.76	[25] [40]

In Vivo Model Verification

With the full *in vivo* model developed and parameterized the model was verified with a set of empirical data involving concentration of proteins bound to PSD-95 under basal conditions. Kennedy et al. collected experimental data on the impact of a heterozygous deletion (HET) of synGAP by quantifying the concentration and type of protein bound to PSD-95 for WT and HET synGAP [7]. The model was first set to mimic the basal conditions of a WT neuron (Fig 5a) and was able to predict the concentrations of synGAP, TARP, LRRTM, and NLGN1 with a relative error of 12.107%, 6.087%, 25.843%, and 11.500%, well within experimental error. The model then mimicked the heterozygous deletion of synGAP (Fig 5b) and predicted the concentrations of synGAP, TARP, LRRTM, and NLGN1 with a relative error of 12.952%, 0.719%, 31.482 %, and 10.849%, well within experimental error.

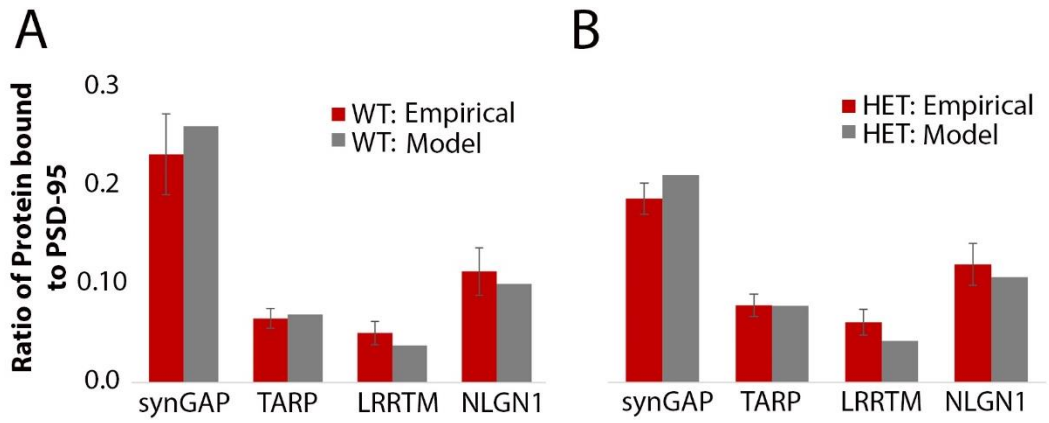

Figure 2.5. *In Vivo* Model Verification. (A) Model prediction of the composition of proteins bound to PSD-95 during basal conditions of a synGAP$^{+/+}$ mouse. (B) Model prediction of protein rearrangement due to a heterozygous deletion of synGAP [7].

2.4.4 Sensitivity Analysis

Quantifying the impact of each parameter on the model is critical when there is uncertainty in the exact parameter value. Understanding which parameters have the most significant impact on the model output informs experimentalist where to focus their efforts and accelerates the design of a fully comprehensive model.

The sensitivity of the model to perturbations in kinetic rate (Table 2) and protein concentrations (Table 3) was independently quantified using Partial Rank Correlation Coefficients

(PRCC) studies. Each study utilized the concentration of TARP bound to PSD-95 over a time course of 60 seconds as the model output. To fully understand the system robustness the studies were also compared with low (10 Hz) and high (100 Hz) frequency stimulations.

The study for the significance of kinetic rates found that the binding rate for PKATARP as well as CaMKII:TARP have a strong impact on the model output. Less intuitive, the study also found that the binding rates for PDE4:PKA were significant. The study for the significance of initial protein concentration found that the concentrations of CaMKII, CaM, and PP1 had the greatest impact on the model output. Efforts in developing computational models for the synapse would greatly benefit from a careful experimental characterization of these values.

Table 2.2. PRCC Values of outliers for varied kinetic rates. Partial Rank Correlation Coefficient (PRCC) values for variations in the kinetic rates used in the model. Values for 10 and 100 Hz are included.

Frequency	**[Varied Input Parameter]**			
	PRCC Value			
10 Hz	[onPKA_mem]	[oncamSGcamKII]	[oncamCpKIITA]	[onPKAcGA1]
	-0.817	-0.288	0.095	0.115
100 Hz	[onPKA_mem]	[oncamSGcamKII]	[oncamCpKIITA]	[onPKAcGA1]
	-0.820	-0.129	0.109	-0.085
10 Hz	[onBPDZ]	[catPKA_mem]	[joinPKAc]	[onPKAPDE4]
	0.336	-0.282	0.237	0.102
100 Hz	[onBPDZ]	[catPKA_mem]	[joinPKAc]	[onPKAPDE4]
	0.475	-0.649	0.444	0.105

Table 2.3. PRCC Values of outliers for varied protein concentration. Partial Rank Correlation Coefficient (PRCC) values for variations in the initial concentrations used in the model. Values for 10 and 100 Hz are included.

Frequency	**[Varied Input Parameter]**			
	PRCC Value			
10 Hz	[LR]	[CaMKII]	[R2C2]	[cycAMP]
	-0.133	0.523	-0.260	-0.130
100 Hz	[LR]	[CaMKII]	[R2C2]	[cycAMP]
	-0.129	0.562	-0.514	0.133
10 Hz	[PP1]	[CaM]	[synGAP]	[PSD-95]
	0.028	0.492	-0.401	0.163
100 Hz	[PP1]	[CaM]	[synGAP]	[PSD-95]
	0.226	0.116	0.272	-0.228
10 Hz	[AC1]	[TARP]	[PDE1]	[PDE4]
	-0.169	-0.0374	0.110	0.113
100 Hz	[AC1]	[TARP]	[PDE1]	[PDE4]
	-0.076	0.231	0.079	0.088

2.4.5 Emergent Activity Dependent Effects

Calcium Dependent Tuning

With the *in vivo* model parameterized and verified for accuracy of steady state conditions the model was focused on the transients of the system. In particular, the impact of varying the frequency of calcium stimulations on the rearrangement of proteins bound to PSD-95.

Kinase/Phosphatase Cascades

The preferential activation of phosphatase or kinase cascades was crucial in determining the response of the system to specific frequencies of calcium stimulations. With a predominant activation of the kinase cascades both synGAP and the C-tail of TARP become more heavily phosphorylated, leading to an increase in TARP bound to PSD-95, Fig 6a (red pathway). However, if the phosphatase cascades are dominant fewer synGAP and TARP are phosphorylated, leading to a decrease in TARP bound to PSD-95, Fig 6a (blue pathway).

The calcium dependent nature of the system originates from the variability of the calcium saturation levels of CaM and its preference for binding different proteins at different saturation levels, Fig 6b. Lower frequency stimulations of calcium saturated the N-terminus of CaM, while higher frequency stimulations of calcium saturated both the C and N-terminus of CaM.

At a lower range frequency stimulation CaM became saturated at the N-terminus and preferentially bound PDE1, and CaN, Fig 6b. This increased PDE1s activity and reduced the concentration of cAMP in the system and consequently lowers the activity of PKA. With a lowered PKA activity, less of Ip35 is active and therefore more PP1 was active. The binding of CaM to CaN increased CaNs ability to dephosphorylate and deactivate Ip35 thereby increasing the concentration of active PP1. With more active PP1 in the system the amount of phosphorylated synGAP and TARP decreased having the cooperative effect of decreasing the concentration of bound TARP, Fig 7a.

At higher range frequency stimulations CaM became preferentially saturated at both the C and N terminus; fully saturated CaM preferentially bound to CaMKII, AC subunits, and synGAP, Fig 6b. The binding of CaM to AC subunits increased the production of cAMP and therefore the activity of PKA. PKA increased the concentration of Ip35 and therefore decreased the concentration of active PP1. Meanwhile the binding of CaM to CaMKII increased its activity rate and phosphorylated both, synGAP and TARP. The phosphorylation of which increased the concentration of TARP bound to PSD-95, Fig 7a.

Frequency Dependent Phosphorylation of TARP

Binding of TARP to PSD-95 is highly regulated by the frequency of the calcium stimulation, through kinase activity. However, TARP is phosphorylated by both PKA and CaMKII at different sites along the cytosolic C-tail. PKA phosphorylates TARP at the T321 site and prevents TARP from binding to the PDZ domains of PSD-95. CaMKII phosphorylates several serine sites along TARP's C-tail giving the C-tail and overall negative charge and allowing the tail to dissociate from the membrane. This effectively elongates the tail and is then able to bind with deeper PDZ domains of PSD-95 [10, 44-47].

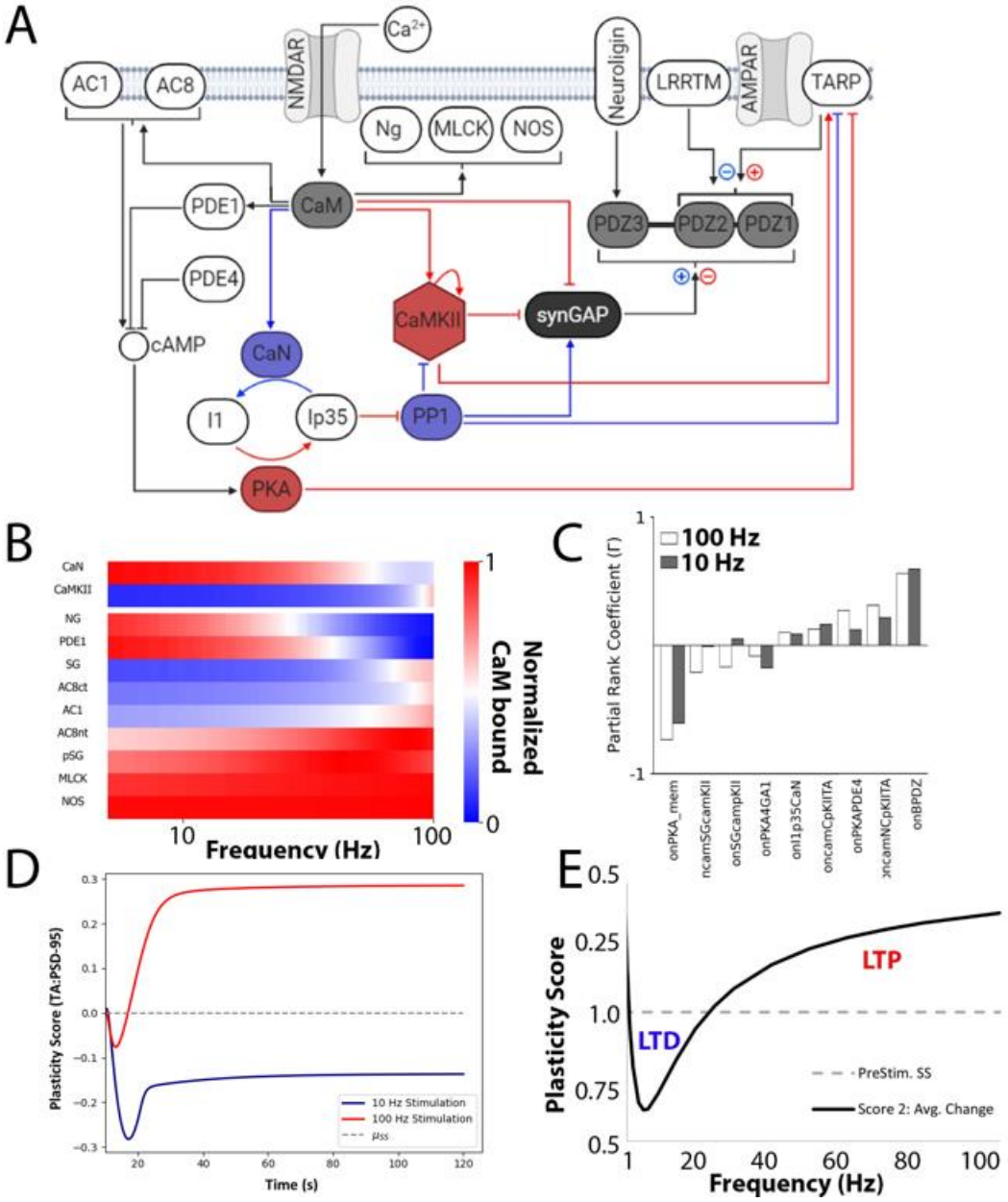

Figure 2.6. Frequency Tuning. (A) Protein interaction schematic displaying preferential activation based on frequency of calcium stimulation. Kinase pathways (CaMKII, PKA) resulting in an increase of bound TARP are displayed in red, while the phosphatase pathways (CaN, PP1) resulting in a decrease of bound TARP are displayed in blue. (B) Frequency dependent binding of CaM to it's binding partners. (C) PRCC data for the correlation between binding rates and the concentration of TARP bound to PSD-95. (D) Time dependent response of the system to 10 Hz (blue line) and 100 Hz (red line) stimulations. Notably for a WT simulation the two scoring mechanisms are equivalent, and the pre-stimulation steady is indicated by the dashed grey line. (E) Response of the system to varying calcium frequencies from 1 Hz to 100 Hz.

2.4.6 Disease State

To further explore the structural role of synGAP on AMPAR insertion, we modeled the response to calcium train stimulus of synGAP homozygous knockout ($SG^{-/-}$) and heterozygous knockdown ($SG^{+/-}$), Fig 7a. To account for the influence of any regulatory mechanisms in gene expression, Fig 7b/c shows the predicted LTP/LTD scores for a system from x0 to x2 synGAP concentration over a frequency range of 10-100 Hz to mimic conditions seen across LTD and LTP stimulation. The equivalent was also shown for LRRTM (Fig 7d) and neuroligin (Fig 7e).

Model Predictions and synGAP Mutants

Studies conducted by the Kennedy lab greatly improved the understanding of synGAP's role as a major inhibitor in the recruitment of AMPA receptors in the PSD [17]. Mutant mice were produced with homozygous knockouts of synGAP, which led to an accelerated development of neurons including the increase in size of spines. The mutant neurons elicited larger frequency and amplitudes of mESPCs reflecting an increased neuronal strength. Notably, the reintroduction of a synGAP mutant without GAP activity decreased the size of the spines, however both the PDZ binding motif and GAP activity were required to fully recover the WT phenotype [17]. Huganir et al. reaffirmed that a synGAP knockout leads to an increase in synaptic transmission, but also found that an overexpression of synGAP led to a decrease in surface AMPAR [48].

Our model fully characterized the inhibitory role of synGAP on the ability for synaptic proteins to bind with PSD-95 by sweeping the concentration of synGAP from x0 to x2 and the frequency of calcium stimulation from 1 to 100 Hz, Fig 7c-e. The sweeps defined regions for which all frequencies of stimulation lead to either an increase or decrease in TARP bound to PSD-95, Fig 7c. The model replicated the heterozygous synGAP ko and found that there was a large shift of the concentration of TARP bound to PSD-95, which was not recoverable by low frequency LTD stimulations, Fig7c. Moreover, the ability to modulate the concentration of TARP bound to PSD-95 was greatly damaged, as low frequency stimulations had a reduced effect on reducing the concentration of TARP bound, Fig 7a/b. The model also replicated the homozygous synGAP ko and found an even more dramatic shift of the concentration of TARP bound to PSD-95. Moreover, the system almost completely lost it's ability to modulate the concentration of TARP bound to PSD-95, Fig 7a/b.

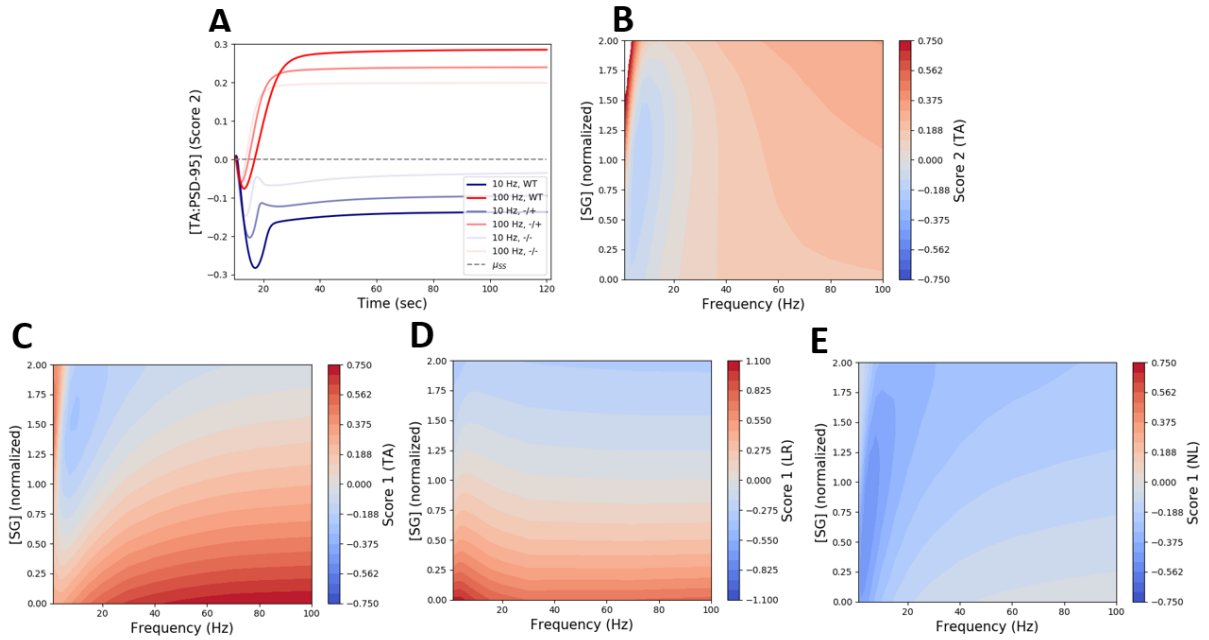

Figure 2.7. Autistic state. (A) Time dependent concentration of TARP bound to PSD-95 (Score 2) for a 10 Hz (navy line) and 100 Hz (red line) calcium stimulation with WT, -/+, and -/- synGAP. (B) Model prediction for the impact of decreasing or increasing the concentration of synGAP on the concentration of TARP bound to PSD-95 (Score 2) over varying frequency of calcium stimulations. (C-E) Model prediction for the impact of decreasing or increasing the concentration of synGAP on the composition of the proteins bound to PSD-95 over varying frequency of calcium stimulations (Score 1). (C) TARP bound to PSD-95. (D) LRRTM bound to PSD-95. (E) Neuroligin bound to PSD-95.

Therapeutic Targets

While the reintroduction of WT synGAP with both its PDZ binding and GAP domain intact is ideal for recovery of the disease state, the model allowed us to investigate other possible therapeutic targets. These targets are aimed at restoring the competition for PSD-95, but cannot restore the dysregulation of the ERK signaling pathway caused by the loss of synGAP. Four therapeutic targets were evaluated: a phosphodiesterase, CaMKII, PKA, and PSD-95 inhibitor.

CaMKII inhibitors have been investigated for their ability to reduce or prevent miniature excitatory postsynaptic currents [49, 50]. Reducing the concentration of CaMKII in the synapse could lead to a decrease in TARP bound to PSD-95, by reducing the concentration of phosphorylated TARP and synGAP. Our simulations show that the inhibition of CaMKII leads to

a recovery of the LTD response, however, after ~20% knockdown of CaMKII the system looses it's ability to increase the concentration of TARP bound to PSD-95, Figa-c.

Inhibition of phosphodiesterase has been used for the reduction of overactive neurons by increasing the cAMP-PKA signaling [51], thereby increasing TARP phosphorylation by PKA and reducing TARPs ability to bind to PSD-95. However, this also has the potential to increase PP1 activity and increase the concentration of TARP and synGAP bound to PSD-95. Our simulations show that while an inhibition of PDE4 leads to a decrease in TARP bound to PSD-95 a ~70% inhibition would be required, and it would not recover the bell shaped curve characteristic of low frequency stimulations, Fig 8d-f.

Upregulating transcription of PKA offered another avenue for decreasing the concentration of TARP bound to PSD-95 through the increased phosphorylation of TARP's 321 site. Our simulations suggest that an upregulation would return the system to WT conditions, however, the concentration of available PKA would have to be increased ~100%, Fig 8g-i.

Drugs targeting the PDZ interactions have also been investigated as a means to control disease related protein signaling [52, 53]. Inhibition of PSD-95 led to not only a decrease in TARP bound to PSD-95, but also returned the bidirectionality of the system's response to varying frequency stimulations, Fig 8j-l.

Of these potential therapeutic drug targets, only a PSD-95 inhibitor was able to completely restore the bidirectionality of the systems response to varying calcium frequencies, Fig 8j-l.

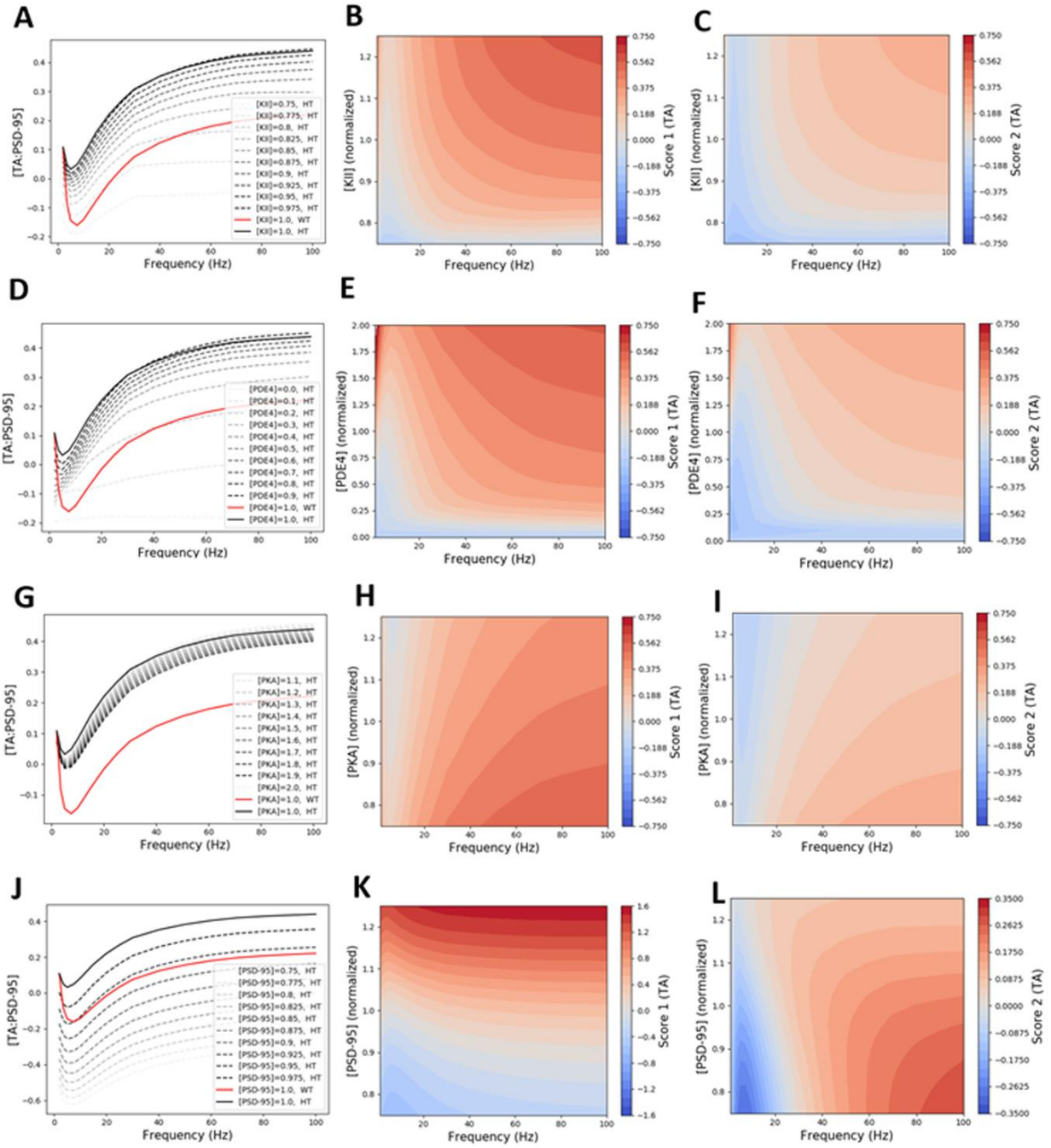

Figure 2.8. Therapeutic drug targets. (A-L) Impact of varying critical protein concentrations, to mimic the impact of inhibitors, on the response of the system. (A,D,G,J) Effect of varying key protein inhibition was compared to the plasticity score for a heterozygous ko (black line) and WT (red line) of synGAP representative of an Autistic state for calcium stimulations of varying frequency. (A-C) CaMKII (D-F) PDE 4 (G-I) PKA (J-L) PSD-95

2.5 Discussion

2.5.1 Model Parameterization

Model development produced a range of unmeasured parameters that were estimated based on previous literature and theoretical work. The impact of the uncertainty of these parameters was quantified using PRCC to establish confidence in these values, as well as identify key parameters to be investigate by new experimental work. While the model showed great parameter robustness, a few key parameters had a significant impact on the model output. The most significant protein concentrations were B-CaMKII, CaMKII, R2C2, cycAMP, PP1, CaM, AC1, synGAP, B-PSD-95, PSD-95 and TARP, see Fig S1. While the most significant kinetic rates were onPKA_mem, oncamSGcamKII, oncamSGcampKII, onPKAcGA1, and onBPDZ, Fig S2.

2.5.2 Dynamic Inhibitory Role of SynGAP

SynGAP's role as a critical inhibitory synaptic protein is only beginning to be understood, however what was missing in the field is a computational model of the system. Our project has developed a comprehensive model for the competition of the PSD-95 PDZ domains allowing for the evaluation of synGAP's role in defining the composition of proteins bound to PSD-95. The model was then used to explore possible therapeutic drug targets in the synapse. We discovered that synGAP not only modulates the composition of proteins bound to PSD-95, but also controls the calcium frequency response of the system. The knockdown of synGAP dysregulates the ability of the system to modulate the concentration of TARP bound to PSD-95 for varying frequency calcium signals.

2.5.3 Proposed Therapeutic Targets

Aid in the design of therapeutics for the treatment of disease states is a major focus of computational biomedical engineering. The mutation of synGAP has led to developmental disorders most commonly ASD and ID, which has been investigated in mice models through heterozygous and homozygous synGAP knockouts. Our model of the synapse was used to investigate four potential therapeutics for the treatment of a heterozygous synGAP knockdown: CaMKII, PDE4, PKA, and PSD-95 inhibitor. Surprisingly, only the PSD-95 inhibitor was effective at restoring the bidirectional frequency dependent response of the system, Fig 8. Reducing the

concentration of PSD-95 resulted in a decrease in TARP and synGAP bound. The excess free synGAP was then able to out compete TARP for binding with CaMKII, thereby decreasing the overall concentration of TARP phosphorylated by CaMKII. Both mechanisms led to the restoration of the system.

2.5.4 Model Predictions of PSD-95 Mutations

The model also offered a new perspective on the counter intuitive observations that the increase or decrease in the concentration of PSD-95 led to an increase in the size and maturation of the synapse. Our simulations show that an increase in the concentration of PSD-95 results in a dramatic overall increase in TARP bound to PSD-95, however, dramatically reduces the systems ability to respond to both low and high frequency stimulations. On the other hand a decrease in the concentration of PSD-95 led to a decrease in the overall concentration of TARP bound to PSD-95, and a greatly heightened ability for the system to respond to low and high frequency stimulations. Therefore, an increase in PSD-95 allows for more AMPAR to be anchored at the PSD-95, but a reduction in PSD-95 allows the synapse to quickly respond to stimulus.

This could reconcile some of the observations made by Bredt et al., who observed an increase in maturation of synapses due to an increase in PSD-95 expression [54]. While Grant et al. observed that a PSD-95 knockdown resulted in an increase in synaptic strength for all frequencies of stimulation [55].

2.5.5 Signaling Role of SynGAP and Future Works

The current model focuses on synGAPs role as an inhibitory structural protein and does not account for synGAPs role in the ERK signal pathway. Kennedy et al. determined that both synGAP structural and signaling role are crucial in maintaining the synapses excitatory and inhibitory balance, however, they regulate spine maturation through different mechanisms. SynGAP's PDZ binding motif was found to be necessary in the role of localization of PSD-95 in the PSD as well as the growth of the synapse. While, synGAP's GAP activity was found to be necessary for growth of PSD protein clusters, and contributes to the growth of the synapse through regulation of the cytoskeleton.

The current system of proteins was deemed sufficient for the current object of evaluating synGAP's role as a dynamic inhibitory protein for PSD-95. Other proteins in this system exist, however, at relatively low abundance and were not included in this model iteration. An avenue for increasing this model's predictive capabilities and clinical uses will be to grow the system to incorporate proteins in the ERK pathway and increase the timescale of the simulation. To incorporate the ERK pathway CDK, Ras, Rap, B-Raf, Mek ½, p33MAPK, and ERK will be included in the next model iteration.

Another avenue for expanding the model will be to model longer time scales and include diffusion of proteins in and out of the synapse including synGAP, AMPAR, and CaMKII. This will be coupled with a model for AMPAR endocytosis/exocytosis which will require the inclusion of EP, PKC, GRIP, PLA, AA, Raf, RKIP, and Raf-actin.

Finally, with the full model for neuronal plasticity developed AMPAR- and NMDAR-gated currents will be modeled with a Hodgkin and Huxley equation to produce the final model output. This will allow the model to be compared with a whole host of experimental data.

2.6 Conclusion

The use of computational models allows for a more developed understanding of systems biology and behaviors that otherwise might escape intuition. Developing a computational model for key post-synaptic proteins surrounding PSD-95 allowed for a more complete understanding of the role of synGAP, Ca^{2+}/CaM, and CaMKII on inhibiting or stimulating change of protein composition within the synapse. The bodies ability to dynamically regulate SynGAP's affinity for PSD-95 was determined to be essential for the system's ability to upregulate and downregulate the concentration of TARP bound to PSD-95, and by proxy the concentration of AMPAR anchored at the PSD.

The dysregulation of synGAP leads to a loss of the system's bidirectional response to vary calcium frequency stimulations, and an overall increase in the concentration of TARP bound to PSD-95. The dysregulation of the system due to a heterozygous knockdown of synGAP was recovered with the introduction of a PSD-95 inhibitor. Notably the bidirectionality of the system was recovered when the concentration of PSD-95 was reduced by 5%. Future work will be aimed at increasing the capabilities of the model by increasing the system of proteins to model the impact

of synGAP on the ERK pathway, as well as the recruitment and subsequent anchoring of AMPAR to the PSD through diffusion and endocytosis.

2.7 Appendix A: LHS/PRCC Results

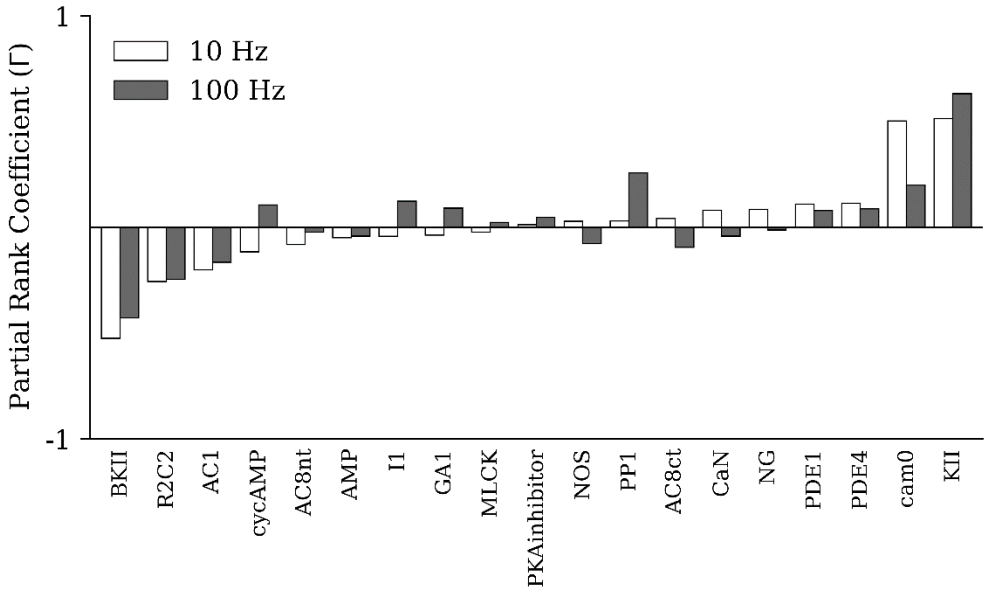

Figure S1. LHS/PRCC for protein concentration. Global sensitivity analysis investigating the impact of the initial concentration of each protein in the system on the model output (TARP bound to PSD-95).

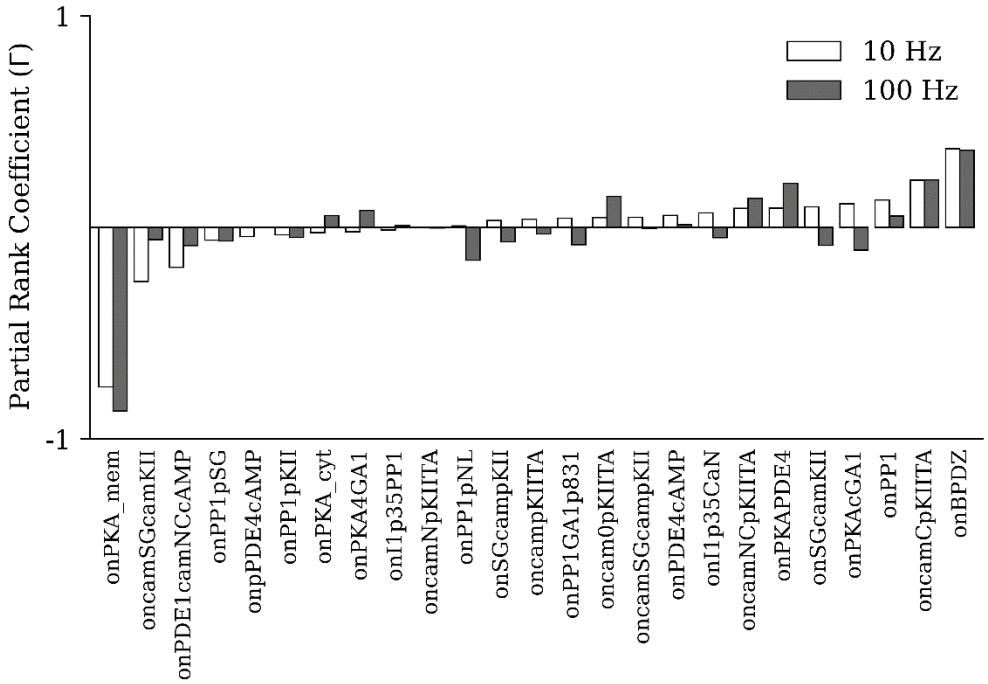

Figure S2. LHS/PRCC for kinetic rates. Global sensitivity analysis investigating the impact of the kinetic rates of each protein interatction in the system on the model output (TARP bound to PSD-95).

2.8 References

[1] D. O. Hebb, *The Organization of Behavior*. Psychology Press, 2005.

[2] S. J. Martin, P. D. Grimwood, and R. G. M. Morris, "Synaptic Plasticity and Memory: An Evaluation of the Hypothesis," *Annu Rev Neurosci,* vol. 23, no. 1, pp. 649-711, 2000, doi: 10.1146/annurev.neuro.23.1.649.

[3] M. Sheng and C. C. Hoogenraad, "The Postsynaptic Architecture of Excitatory Synapses: A More Quantitative View," *Annu Rev Biochem,* vol. 76, no. 1, pp. 823-847, 2007, doi: 10.1146/annurev.biochem.76.060805.160029.

[4] J. F. Sturgill, P. Steiner, B. L. Czervionke, and B. L. Sabatini, "Distinct Domains within PSD-95 Mediate Synaptic Incorporation, Stabilization, and Activity-Dependent Trafficking," *J Neurosci,* vol. 29, no. 41, pp. 12845-12854, 2009, doi: 10.1523/jneurosci.1841-09.2009.

[5] J. H. Kim, D. Liao, L.-F. Lau, and R. L. Huganir, "SynGAP: a Synaptic RasGAP that Associates with the PSD-95/SAP90 Protein Family," *Neuron,* vol. 20, no. 4, pp. 683-691, 1998, doi: 10.1016/s0896-6273(00)81008-9.

[6] H.-J. Chen, M. Rojas-Soto, A. Oguni, and M. B. Kennedy, "A Synaptic Ras-GTPase Activating Protein (p135 SynGAP) Inhibited by CaM Kinase II," *Neuron,* vol. 20, no. 5, pp. 895-904, 1998, doi: 10.1016/S0896-6273(00)80471-7.

[7] W. G. Walkup *et al.*, "A model for regulation by SynGAP-α1 of binding of synaptic proteins to PDZ-domain 'Slots' in the postsynaptic density," *Elife,* vol. 5, 2016, doi: 10.7554/elife.16813.

[8] W. G. Walkup, M. J. Sweredoski, R. L. Graham, S. Hess, and M. B. Kennedy, "Phosphorylation of synaptic GTPase-activating protein (synGAP) by polo-like kinase (Plk2) alters the ratio of its GAP activity toward HRas, Rap1 and Rap2 GTPases," *Biochem Biophys Res Commun,* vol. 503, no. 3, pp. 1599-1604, 2018, doi: 10.1016/j.bbrc.2018.07.087.

[9] Y. Araki, M. Zeng, M. Zhang, and Richard L. Huganir, "Rapid Dispersion of SynGAP from Synaptic Spines Triggers AMPA Receptor Insertion and Spine Enlargement during LTP," *Neuron,* vol. 85, no. 1, pp. 173-189, 2015, doi: 10.1016/j.neuron.2014.12.023.

[10] A.-S. Hafner *et al.*, "Lengthening of the stargazin cytoplasmic tail increases synaptic transmission by promoting interaction to deeper domains of PSD-95," *Neuron*, vol. 86, no. 2, pp. 475-489, 2015, doi: 10.1016/j.neuron.2015.03.013.

[11] M. H. Berryer *et al.*, "Mutations in SYNGAP1 Cause Intellectual Disability, Autism, and a Specific Form of Epilepsy by Inducing Haploinsufficiency," *Hum Mutat*, vol. 34, no. 2, pp. 385-394, 2013, doi: 10.1002/humu.22248.

[12] James P. Clement *et al.*, "Pathogenic SYNGAP1 Mutations Impair Cognitive Development by Disrupting Maturation of Dendritic Spine Synapses," *Cell*, vol. 151, no. 4, pp. 709-723, 2012, doi: 10.1016/j.cell.2012.08.045.

[13] J. P. Clement, E. D. Ozkan, M. Aceti, C. A. Miller, and G. Rumbaugh, "SYNGAP1 links the maturation rate of excitatory synapses to the duration of critical-period synaptic plasticity," *J Neurosci*, vol. 33, no. 25, pp. 10447-10452, 2013, doi: 10.1523/JNEUROSCI.0765-13.2013.

[14] F. F. Hamdan *et al.*, "Mutations in SYNGAP1 in Autosomal Nonsyndromic Mental Retardation," *N Engl J Med*, vol. 360, no. 6, pp. 599-605, 2009, doi: 10.1056/NEJMoa0805392.

[15] F. F. Hamdan *et al.*, "De Novo SYNGAP1 Mutations in Nonsyndromic Intellectual Disability and Autism," *Biol Psychiatry*, vol. 69, no. 9, pp. 898-901, 2011, doi: 10.1016/j.biopsych.2010.11.015.

[16] J. L. R. Rubenstein and M. M. Merzenich, "Model of autism: increased ratio of excitation/inhibition in key neural systems," *Genes Brain Behav*, vol. 2, no. 5, pp. 255-267, 2003, doi: 10.1034/j.1601-183x.2003.00037.x.

[17] L. E. Vazquez, H.-J. Chen, I. Sokolova, I. Knuesel, and M. B. Kennedy, "SynGAP Regulates Spine Formation," *J Neurosci*, vol. 24, no. 40, pp. 8862-8872, 2004, doi: 10.1523/JNEUROSCI.3213-04.2004.

[18] T. M. Bartol *et al.*, "Computational reconstitution of spine calcium transients from individual proteins," *Front Synaptic Neurosci*, vol. 7, pp. 17-17, 2015, doi: 10.3389/fnsyn.2015.00017.

[19] D. X. Keller, K. M. Franks, J. T. M. Bartol, and T. J. Sejnowski, "Calmodulin activation by calcium transients in the postsynaptic density of dendritic spines," *PLoS One*, vol. 3, no. 4, pp. e2045-e2045, 2008, doi: 10.1371/journal.pone.0002045.

[20] S. Marino, I. B. Hogue, C. J. Ray, and D. E. Kirschner, "A methodology for performing global uncertainty and sensitivity analysis in systems biology," *J Theor Biol,* vol. 254, no. 1, pp. 178-196, 2008, doi: 10.1016/j.jtbi.2008.04.011.

[21] I. M. Sobol′, "Global sensitivity indices for nonlinear mathematical models and their Monte Carlo estimates," *Mathematics and computers in simulation,* vol. 55, no. 1-3, pp. 271-280, 2001, doi: 10.1016/s0378-4754(00)00270-6.

[22] A. Saltelli, P. Annoni, I. Azzini, F. Campolongo, M. Ratto, and S. Tarantola, "Variance based sensitivity analysis of model output. Design and estimator for the total sensitivity index," *Computer physics communications,* vol. 181, no. 2, pp. 259-270, 2010, doi: 10.1016/j.cpc.2009.09.018.

[23] D. R. Romano, M. C. Pharris, N. M. Patel, and T. L. Kinzer-Ursem, "Competitive tuning: Competition's role in setting the frequency-dependence of Ca2+-dependent proteins," *PLoS Comput Biol,* vol. 13, no. 11, pp. e1005820-e1005820, 2017, doi: 10.1371/journal.pcbi.1005820.

[24] R. F. Oliveira, M. Kim, and K. T. Blackwell, "Subcellular location of PKA controls striatal plasticity: stochastic simulations in spiny dendrites," *PLoS Comput Biol,* vol. 8, no. 2, pp. e1002383-e1002383, 2012, doi: 10.1371/journal.pcbi.1002383.

[25] M. Lindskog, M. Kim, M. A. Wikström, K. T. Blackwell, and J. H. Kotaleski, "Transient calcium and dopamine increase PKA activity and DARPP-32 phosphorylation," *PLoS Comput Biol,* vol. 2, no. 9, pp. e119-e119, 2006, doi: 10.1371/journal.pcbi.0020119.

[26] H. Urakubo, M. Honda, R. C. Froemke, and S. Kuroda, "Requirement of an Allosteric Kinetics of NMDA Receptors for Spike Timing-Dependent Plasticity," *J Neurosci,* vol. 28, no. 13, pp. 3310-3323, 2008, doi: 10.1523/JNEUROSCI.0303-08.2008.

[27] N. Mons, D. M. F. Cooper, and J. W. Karpen, "Adenylyl cyclases and the interaction between calcium and cAMP signalling," *Nature,* vol. 374, no. 6521, pp. 421-424, 1995, doi: 10.1038/374421a0.

[28] H. Wang, G. C. K. Chan, J. Athos, and D. R. Storm, "Synaptic concentration of type-I adenylyl cyclase in cerebellar neurons," *J Neurochem,* vol. 83, no. 4, pp. 946-954, 2002, doi: 10.1046/j.1471-4159.2002.01206.x.

[29] G. Antunes, A. C. Roque, and F. M. Simoes-de-Souza, "Stochastic Induction of Long-Term Potentiation and Long-Term Depression," *Sci Rep,* vol. 6, no. 1, pp. 30899-30899, 2016, doi: 10.1038/srep30899.

[30] S. Halpain, A. Hipolito, and L. Saffer, "Regulation of F-Actin Stability in Dendritic Spines by Glutamate Receptors and Calcineurin," *J Neurosci,* vol. 18, no. 23, pp. 9835-9844, 1998, doi: 10.1523/JNEUROSCI.18-23-09835.1998.

[31] L. L. Gomez, S. Alam, K. E. Smith, E. Horne, and M. L. Dell'Acqua, "Regulation of A-Kinase Anchoring Protein 79/150–cAMP-Dependent Protein Kinase Postsynaptic Targeting by NMDA Receptor Activation of Calcineurin and Remodeling of Dendritic Actin," *J Neurosci,* vol. 22, no. 16, pp. 7027-7044, 2002, doi: 10.1523/jneurosci.22-16-07027.2002.

[32] J. Lisman, H. Schulman, and H. Cline, "The molecular basis of CaMKII function in synaptic and behavioural memory," *Nat Rev Neurosci,* vol. 3, no. 3, pp. 175-190, 2002, doi: 10.1038/nrn753.

[33] N. E. Erondu and M. B. Kennedy, "Regional distribution of type II Ca2+/calmodulin-dependent protein kinase in rat brain," *J Neurosci,* vol. 5, no. 12, pp. 3270-3277, 1985, doi: 10.1523/jneurosci.05-12-03270.1985.

[34] J. M. Bradshaw, K. Yoshi, M. Tobias, and S. Howard, "An Ultrasensitive Ca2+/Calmodulin-Dependent Protein Kinase II-Protein Phosphatase 1 Switch Facilitates Specificity in Postsynaptic Calcium Signaling," *Proc Natl Acad Sci U S A,* vol. 100, no. 18, pp. 10512-10517, 2003, doi: 10.1073/pnas.1932759100.

[35] J. D. Petersen, X. Chen, L. Vinade, A. Dosemeci, J. E. Lisman, and T. S. Reese, "Distribution of Postsynaptic Density (PSD)-95 and Ca2+/Calmodulin-Dependent Protein Kinase II at the PSD," *J Neurosci,* vol. 23, no. 35, pp. 11270-11278, 2003, doi: 10.1523/JNEUROSCI.23-35-11270.2003.

[36] C. Xiaobing *et al.*, "Mass of the postsynaptic density and enumeration of three key molecules," *Proc Natl Acad Sci U S A,* vol. 102, no. 32, pp. 11551-11556, 2005, doi: 10.1073/pnas.0505359102.

[37] M. S. Lowenthal, S. P. Markey, and A. Dosemeci, "Quantitative Mass Spectrometry Measurements Reveal Stoichiometry of Principal Postsynaptic Density Proteins," *J Proteome Res,* vol. 14, no. 6, pp. 2528-2538, 2015, doi: 10.1021/acs.jproteome.5b00109.

[38] C. Bats, L. Groc, and D. Choquet, "The Interaction between Stargazin and PSD-95 Regulates AMPA Receptor Surface Trafficking," *Neuron,* vol. 53, no. 5, pp. 719-734, 2007, doi: 10.1016/j.neuron.2007.01.030.

[39] E. R. Graf, Y. Kang, A. M. Hauner, and A. M. Craig, "Structure function and splice site analysis of the synaptogenic activity of the neurexin-1 beta LNS domain," *J Neurosci,* vol. 26, no. 16, pp. 4256-4265, 2006, doi: 10.1523/JNEUROSCI.1253-05.2006.

[40] A. Chay, I. Zamparo, A. Koschinski, M. Zaccolo, and K. T. Blackwell, "Control of βAR- and N-methyl-D-aspartate (NMDA) Receptor-Dependent cAMP Dynamics in Hippocampal Neurons," *PLoS Comput Biol,* vol. 12, no. 2, pp. e1004735-e1004735, 2016, doi: 10.1371/journal.pcbi.1004735.

[41] S. Strack, M. A. Barban, B. E. Wadzinski, and R. J. Colbran, "Differential Inactivation of Postsynaptic Density-Associated and Soluble Ca2+/Calmodulin-Dependent Protein Kinase II by Protein Phosphatases 1 and 2A," *J Neurochem,* vol. 68, no. 5, pp. 2119-2128, 2002, doi: 10.1046/j.1471-4159.1997.68052119.x.

[42] J. R. Bordelon, Y. Smith, A. C. Nairn, R. J. Colbran, P. Greengard, and E. C. Muly, "Differential localization of protein phosphatase-1alpha, beta and gamma1 isoforms in primate prefrontal cortex," *Cereb Cortex,* vol. 15, no. 12, pp. 1928-1937, 2005.

[43] D. W. Carr, R. E. Stofko-Hahn, I. D. Fraser, R. D. Cone, and J. D. Scott, "Localization of the cAMP-dependent protein kinase to the postsynaptic densities by A-kinase anchoring proteins. Characterization of AKAP 79," *J Biol Chem,* vol. 267, no. 24, p. 16816, 1992.

[44] "The role of stargazin and TARP phosphorylation in synaptic plasticity," ed, 2014.

[45] A. Sumioka, D. Yan, and S. Tomita, "TARP Phosphorylation Regulates Synaptic AMPA Receptors through Lipid Bilayers," *Neuron,* vol. 66, no. 5, pp. 755-767, 2010, doi: 10.1016/j.neuron.2010.04.035.

[46] S. Tomita, V. Stein, T. J. Stocker, R. A. Nicoll, and D. S. Bredt, "Bidirectional Synaptic Plasticity Regulated by Phosphorylation of Stargazin-like TARPs," *Neuron,* vol. 45, no. 2, pp. 269-277, 2005, doi: 10.1016/j.neuron.2005.01.009.

[47] J. Park *et al.*, "CaMKII Phosphorylation of TARPγ-8 Is a Mediator of LTP and Learning and Memory," *Neuron,* vol. 92, no. 1, pp. 75-83, 2016, doi: 10.1016/j.neuron.2016.09.002.

[48] R. Gavin, J. P. Adams, H. K. Jee, and L. H. Richard, "SynGAP Regulates Synaptic Strength and Mitogen-Activated Protein Kinases in Cultured Neurons," *Proc Natl Acad Sci U S A*, vol. 103, no. 12, pp. 4344-4351, 2006, doi: 10.1073/pnas.0600084103.

[49] I. Ninan and O. Arancio, "Presynaptic CaMKII Is Necessary for Synaptic Plasticity in Cultured Hippocampal Neurons," *Neuron*, vol. 42, no. 1, pp. 129-141, 2004, doi: 10.1016/S0896-6273(04)00143-6.

[50] S. Incontro *et al.*, "The CaMKII/NMDA receptor complex controls hippocampal synaptic transmission by kinase-dependent and independent mechanisms," *Nat Commun*, vol. 9, no. 1, pp. 2069-21, 2018, doi: 10.1038/s41467-018-04439-7.

[51] X. Liu, P. Zhong, C. Vickstrom, Y. Li, and Q.-S. Liu, "PDE4 Inhibition Restores the Balance Between Excitation and Inhibition in VTA Dopamine Neurons Disrupted by Repeated In Vivo Cocaine Exposure," *Neuropsychopharmacology*, vol. 42, no. 10, pp. 1991-1999, 2017, doi: 10.1038/npp.2017.96.

[52] K. K. Dev, "Making protein interactions druggable: targeting PDZ domains," *Nat Rev Drug Discov*, vol. 3, no. 12, pp. 1047-1056, 2004, doi: 10.1038/nrd1578.

[53] T. Yuan-Xiang and J. Roger, "PDZ Domains at Excitatory Synapses: Potential Molecular Targets for Persistent Pain Treatment," *CN*, vol. 4, no. 3, pp. 217-223, 2006, doi: 10.2174/157015906778019473.

[54] E.-H. Alaa El-Din, S. Eric, M. C. Dane, A. N. Roger, and S. B. David, "PSD-95 Involvement in Maturation of Excitatory Synapses," *Science*, vol. 290, no. 5495, pp. 1364-1368, 2000.

[55] M. Migaud *et al.*, "Enhanced long-term potentiation and impaired learning in mice with mutant postsynaptic density-95 protein," *Nature*, vol. 396, no. 6710, pp. 433-439, 1998, doi: 10.1038/24790.

[56] S. Pepke, T. Kinzer-Ursem, S. Mihalas, and M. B. Kennedy, "A dynamic model of interactions of Ca2+, calmodulin, and catalytic subunits of Ca2+/calmodulin-dependent protein kinase II," *PLoS Comput Biol*, vol. 6, no. 2, pp. e1000675-e1000675, 2010, doi: 10.1371/journal.pcbi.1000675.

[57] N. Masada, S. Schaks, S. E. Jackson, A. Sinz, and D. M. F. Cooper, "Distinct Mechanisms of Calmodulin Binding and Regulation of Adenylyl Cyclases 1 and 8," *Biochemistry*, vol. 51, no. 40, pp. 7917-7929, 2012, doi: 10.1021/bi300646y.

[58] M. C. Potier, E. Chelot, Y. Pekarsky, K. Gardiner, J. Rossier, and W. G. Turnell, "The Human Myosin Light Chain Kinase (MLCK) from Hippocampus: Cloning, Sequencing, Expression, and Localization to 3qcen–q21," *Genomics,* vol. 29, no. 3, pp. 562-570, 1995, doi: 10.1006/geno.1995.9965.

[59] J. D. Johnson, C. Snyder, M. Walsh, and M. Flynn, "Effects of myosin light chain kinase and peptides on Ca2+ exchange with the N- and C-terminal Ca2+ binding sites of calmodulin," *J Biol Chem,* vol. 271, no. 2, pp. 761-767, 1996, doi: 10.1074/jbc.271.2.761.

[60] Y. Kubota, J. A. Putkey, and M. N. Waxham, "Neurogranin controls the spatiotemporal pattern of postsynaptic Ca2+/CaM signaling," *Biophys J,* vol. 93, no. 11, pp. 3848-3859, 2007, doi: 10.1529/biophysj.107.106849.

[61] A. Persechini, H. D. White, and K. J. Gansz, "Different mechanisms for Ca2+ dissociation from complexes of calmodulin with nitric oxide synthase or myosin light chain kinase," *J Biol Chem,* vol. 271, no. 1, pp. 62-67, 1996.

[62] M. Kim *et al.,* "Colocalization of protein kinase A with adenylyl cyclase enhances protein kinase A activity during induction of long-lasting long-term-potentiation," *PLoS Comput Biol,* vol. 7, no. 6, pp. e1002084-e1002084, 2011, doi: 10.1371/journal.pcbi.1002084.

[63] R. S. Can Özden, Nicholas Santos, Emily Agnello, Christl Gaubitz, Emily, J. F. Lapinskas, Edward A. Esposito, Brian A. Kelch, Scott C. Garman, Yasunori, and M. M. S. Hayashi, "CaMKII binds both substrates and effectors at the active site," *News of Science,* p. 283, 2021.

[64] R. S. Walikonis, A. Oguni, E. M. Khorosheva, C.-J. Jeng, F. J. Asuncion, and M. B. Kennedy, "Densin-180 Forms a Ternary Complex with the α-Subunit of Ca2+/Calmodulin-Dependent Protein Kinase II and α-Actinin," *The Journal of neuroscience,* vol. 21, no. 2, pp. 423-433, 2001, doi: 10.1523/JNEUROSCI.21-02-00423.2001.

[65] R. Raveendran *et al.,* "Phosphorylation status of the NR2B subunit of NMDA receptor regulates its interaction with calcium/calmodulin-dependent protein kinase II," *J Neurochem,* vol. 110, no. 1, pp. 92-105, 2009, doi: 10.1111/j.1471-4159.2009.06108.x.

[66] E. L. A. Stein and D. M. Chetkovich, "Regulation of stargazin synaptic trafficking by C-terminal PDZ ligand phosphorylation in bidirectional synaptic plasticity," *J Neurochem,* vol. 113, no. 1, pp. 42-53, 2010, doi: 10.1111/j.1471-4159.2009.06529.x.

[67] M. Irie *et al.*, "Binding of Neuroligins to PSD-95," *Science*, vol. 277, no. 5331, pp. 1511-1515, 1997, doi: 10.1126/science.277.5331.1511.

3. MECHANISTIC COMPUTATIONAL MODELING FOR DRUG RELEASE OF IMPLANTABLE, BIORESORBABLE DRUG DELIVERY DEVICES

3.1 Abstract

Implantable, bioresorbable drug delivery systems offer a unique alternative to current drug administration techniques, and allow for patient tailored drug dosage, while also increasing patient compliance. This study investigates drug release as a function of water-mediated polymer phase inversion into a solid depot within the first hours to days, as well as hydrolysis-mediated degradation and erosion of the implant over the next few weeks. Tuning this process allows for the drug release rate of the encapsulated drug to be controlled for a wide range of patient needs. Mechanistic mathematical modeling not only allows for the acceleration of the implant design process but also for the prediction of physical anomalies that are not intuitive and might otherwise elude discovery. Finite difference methods were used to solve for the solidification of polymer as well as the degradation and erosion of the polymer due to the hydrolysis of ester bonds, which produce carboxylic acid terminate oligomers and monomers. Acid dissociation from these accumulating byproducts and acidic drugs are also simulated by the model to account for local pH change. A sensitivity analysis showed that the impact of the degradation rates was highly time dependent, however, the non-catalytic end and auto-catalytic random chain scission rates had the most significant impact on the drug release profile. Compared to experimental data, the computational model accurately predicted the drug release profile from implantable microspheres and *in situ* forming implants with an average error of 7.200 % and 7.519 % respectively. Moreover, the model predicted the drug release during the solidification of the implant with an average error of 10.906% for microspheres and 3.539% for the in situ forming implants. This model accurately predicts the drug release profiles from a range of implant size and molecular weight, offering a tool to accelerate the design process for an implant to meet a patient specific clinical need.

3.2 Introduction

Approximately 50% of the US population takes at least one prescription drug, and the number of patients is anticipated to increase as the population ages. Furthermore, as many as 50% of patients

do not self-administer their medication as prescribed, which ultimately costs billions of dollars per year in avoidable health care costs [1, 2]. Reliance on repetitive doses of one-size-fits all pills not only results in low patient compliance, but even when taken as prescribed, results in fluctuations of drug concentration around a target zone, resulting in poor clinical outcomes for the patients [3-5]. Controlled release systems provide a platform to maintain blood plasma levels of drugs without the need for repeating dosing [6].

Polymer-based controlled release systems have already entered the market and are being used to treat a wide range of diseases from cancers to infections with a controlled systemic or local drug dosage [7-15]. One such category of implants referred to as *in situ* forming implants (ISFIs) have been used to treat prostate cancer by increasing the body's systemic concentration of leuprolide acetate, which reduces the production of testosterone to treat the cancer [7, 8]. Other ISFIs have been designed to release doxycycline only into the local, afflicted tissue to treat gum disease (periodontitis) [8, 9]. Microspheres have been developed to be injected and embolized into the vasculature around cancerous tissue to cut off the blood supply and release doxorubicin locally into the tumor [10]. Current research in the field shows promise of improving the quality of life for millions with the development of a long term ISFI that releases a mixture of antiretroviral drugs for the treatment or prophylaxis of HIV [11]. The drugs maintained their potency allowing for the release system to be effective on a time scale of week to up to one year [11].

These two controlled release platforms (ISFI, and microspheres) can be designed to encapsulate a wide range of drugs and can be placed nearly anywhere in the body via a single minimally invasive injection. Typically, these phase sensitive implants consist of a biodegradable, biocompatible polymer dissolved in a biocompatible and water immiscible solvent. ISFIs are injected directly into the body where counter exchange of water from the tissue and solvent from the implant solution drives a phase inversion of the polymer, resulting in the formation of a solid drug-eluting depot [13]. Implantable microspheres are first formed via phase inversion in a collection tank before the solid depot is implanted into the body [16, 17]. As the polymer precipitates out of solution, the water simultaneously acts as a catalyst for the degradation of the bioresorbable polymer through hydrolysis of ester bond linkages [18]. These release systems give a characteristic burst of drug followed by a period of diffusion limited release, then as the polymer degrades, a period of degradation enhanced release. The release profile dictates the drug concentration in a patient's blood plasma over the course of the drug therapy [19].

To better meet patient needs, drug release profiles could be tuned by varying factors such as the polymer composition, hydrophobicity of the solvent, and polymer chain length [19]. Developing these technologies into personalized healthcare requires that the rate of drug release is predictable and tunable. However, experimentally optimizing the parameters that influence the drug release is time consuming and expensive [15]. Development of a mathematical model in which experimentally controllable parameters can be varied to accurately predict drug release profiles would allow for efficient testing of parameter regimes that produce reliable control of desired drug release profiles, and would facilitate the rational design of implant formulations.

Building upon decades of research on the modeling of degrading/swelling polymer implants, the current study progresses previous models in four aspects: (a) consideration of the impact of phase inversion on the drug release of both microspheres and ISFIs; (b) investigation of observable phenomena such as complex implant geometries, nonuniform drug distribution, and swelling of larger implants; (c) explicit modeling of the production and transport of H^+ ions, which catalyze the degradation and diffusion of acid as separate processes; (d) inclusion of a full probability model for the distribution of oligomers produced from random chain scission as proposed by Flory [20]. The ultimate goal of this work is to create a mechanistic model of these implants with as few estimated parameters as possible such that the model is able to predict a wide range of drug release profiles from multiple systems while also providing insight into the processes that most impact drug release profiles in different time regimes.

3.3 Materials and methods

3.3.1 Materials

Poly(DL-lactide-co-glycolide) (PLGA 50:50, acid endcap, 4A, MW 53 kDa, inherent viscosity 0.38 dl/g) was obtained from Evonik Birmingham Laboratories (Birmingham, AL). Poly(DL-lactide-co-glycolide) (PLGA 50:50, acid endcap, MW 15 kDa) was obtained from PolySciTech (West Lafayette, IN).,) . N-methyl-2-pyrrolidone (NMP) was obtained from Fisher Scientific and sodium fluorescein (MW 376.28) was obtained from Acros Organics. All supplies were used as received.

3.3.2 Preparation of polymer solutions

Polymer solutions were prepared by combining poly(lactic-co-glycolic) acid (PLGA), N-methyl-2-pyrrolidone (NMP), and fluorescein in a 39:60:1 mass ratio. First, fluorescein was dissolved in NMP and then PLGA was added. The solution was stirred overnight to ensure complete dissolution. Polymer was stored at room temperature for less than a week before use.

3.3.3 Drug release studies

Implants were formed by injecting 60 µL of polymer solution into 10 mL of phosphate buffered saline (PBS). Implants were kept at 37°C on a shaker at 100 rpm for the duration of the study. Samples were taken from the bath side solution at 0.25, 0.5, 1, 2, 4, 6, 24, 48, 72, 96, 120, 144, 168, 240, 336, 408, 504 hours *post-exposure to aqueous conditions (post-exposure)*. The bath solution was completely replaced at these time points to maintain sink conditions. Residual drug mass after 21 d was determined by degrading the implants in 2 M NaOH. The fluorescence of all samples was quantified using a SpectraMax M5 microplate reader using an excitation of 485 nm and emission of 525 nm, and results were compared to a standard curve to obtain the cumulative mass of fluorescein released.

3.3.4 Scanning Electron Microscope (SEM) imaging

To prepare implants for SEM imaging, implants at selected time points were first freeze-fractured on dry ice and then lyophilized for 4 days. After lyophilization, implants were mounted on aluminum stubs and sputter-coated with platinum for 60 s using a Cressington 208 HR sputter coater. Imaging was done using a NovaNanoSEM with a spot size of 3 and a voltage of 5.00 kV.

3.3.5 Diffusion-Weighted Magnetic Resonance Imaging (DWI)

To perform DWI, implants were formed as described above. At each time point (0.25, 1, 2, 4, 6, 24, 48, 72, 96, 120, 144, 168, 240, 336, 408, 504 h post-exposure), implants were removed from solution and placed into a 3D-printed insert centered in a water-filled phantom bottle. DWI was conducted using a Bruker BioSpec 70/30 USR 7T Preclinical MRI system and Bruker rat head/mouse body RF RES 300 ^{1}H 075/040 QSN TR volume coil. A standard diffusion-weighted spin echo protocol was utilized (TE=17.5 ms, TR=2500 ms, FOV=35x35 mm^2, slice

thickness=0.80 mm, b=0,1000 s/mm^2). The raw diffusion data was used to create apparent diffusion coefficient (ADC) maps of the implant as previously described [21].

3.3.6 Fluorescence Recovery After Photobleaching (FRAP)

Three different types of samples were prepared for FRAP analysis. The first sample was a solution of 2000 ng/mL fluorescein in phosphate buffered saline (PBS) placed under a coverslip on a microscope slide. The second was approximately 60 µL of polymer solution, prepared as described in section 2.2 above, placed under a coverslip on a microscope slide. The third sample was the same polymer solution placed under a coverslip on a microscope slide with the slide then placed in a PBS bath for 24 h to allow for polymer solidification via phase inversion.

FRAP was performed on an upright Zeiss LSM T-PMT confocal microscope (Carl Zeiss, Thornwood, NY) with a 40x water immersion objective lens. Experiments were performed at room temperature. Photobleaching was achieved by focusing the 405 nm laser line at 90% power (27mW) on circular sample areas 37.4 µm in radius. Fluorescence recovery was then recorded at 2% laser power (0.6mW). Measurements were taken in mid-plane of the cover and bottom glass slides (as verified by reflectance imaging).

3.3.7 Mathematical Modeling and Numerical Analysis

The numerical solution of the system of PDEs was evaluated using a finite difference method solver in Python 3.7 with the development environment Spyder 3.3.6. To ensure numerical accuracy while maintaining unconditional stability of the solution, the system of PDEs modeling the reaction-diffusion equations was solved with a conserved 2nd order central (CN-2) and backwards differential formula (BDF-2) schemes with adaptive time stepping. The nonlinear equations were linearized through decoupling and solving for intermediate steps. The system of ODEs modeling the acid dissociation was solved with the 4th order Runge Kutta on a much finer time scale. Large simulation sweeps utilized the Brown Community Cluster on the Purdue campus.

3.3.8 Modeling Parameterization/Verification

Model development produced a set of parameters whose values were unknown, or that varied over a large range. These included diffusion coefficients for drug, oligomers, monomers, and solvent

through precipitated polymer as well as four degradation rates for end or random, and noncatalytic or auto-catalytic chain scission. Diffusivity values were derived from experimental data and degradation rates were approximated by fitting a series of degradation profiles, see section 3.5.2. Simulations were used to predict a host of outputs that were compared to independent empirical measurements. Given that there was uncertainty in some of the unknown model parameter values, global sensitivity analysis was utilized to access the sensitivity of model output (drug release profile) over a range of unknown parameter values. Latin Hypercube Sampling (LHS) was used to efficiently sample input parameter space and partial rank correlation coefficient analysis was used to assess model output sensitivity [22-25]. LHS/PRCC studies were conducted to evaluate model sensitivity to parameters involved in diffusion separately from parameters involved in degradation rates.

3.4 Results

3.4.1 Model Development

In this work, our modeling efforts center around the presence of water in the implants (Fig 1). As water diffuses into the controlled release systems, the polymer precipitates into a solid state thereby decreasing the diffusivity of drug out of the depot. In the case ISFIs, the solidification of the implant occurs over a time scale of days resulting in an initial burst of drug out of the implant. The introduction of water also catalyzes the hydrolysis of the ester bonds of immobile long polymer chains to produce short diffusible polymer chains [18]. As the small polymer chains are transported out of the implant, the porosity of the polymer increases over time resulting in increased diffusion of drug out of the ISFI. To capture the various aspects of these water-dependent processes we take a comprehensive approach to modeling time and space varying polymer solidification (Section 3.2) and water-dependent hydrolysis of the ISFI polymer (Section 3.3). These processes are then combined and solved through a sophisticated numerical analysis scheme (Section 3.4) that allows for 3D simulation of temporal and spatially dependent drug release profiles.

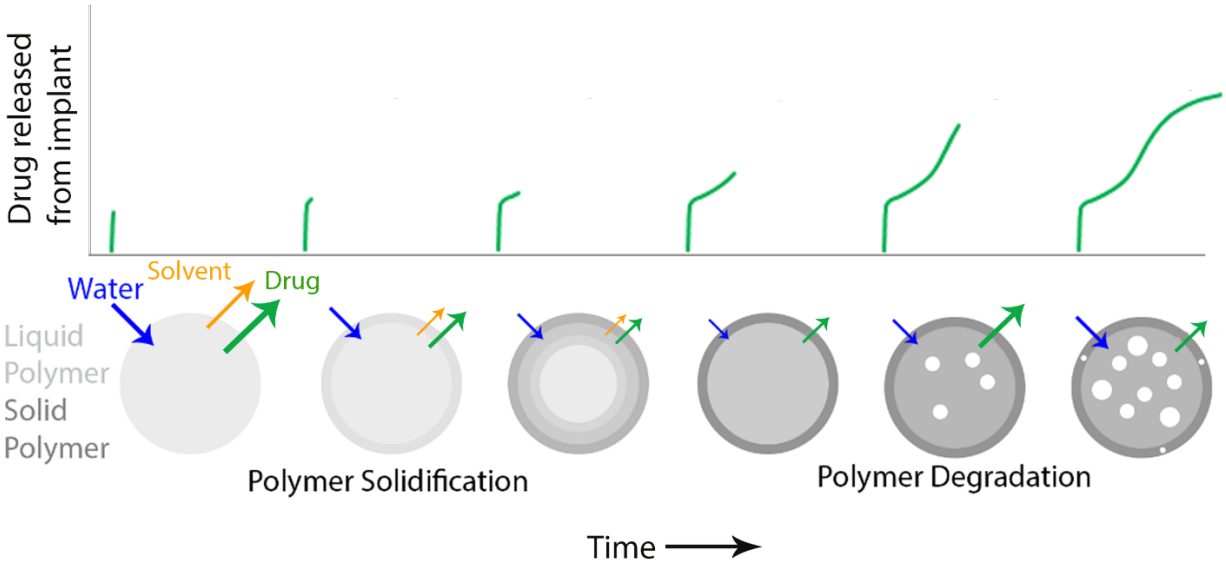

Figure 3.1. Scheme of solidification and degradation. (Bottom) The drug release from the implant is controlled by the solidification of the ISFI, and at later time points by degradation and erosion of the solid polymer matrix (white circles indicate pore formation). (Top) The influence of these two mechanisms on the drug release profile.

3.4.2 Modeling Polymer Solidification

The impact of varying the size of the phase-sensitive controlled release vehicles was considered by evaluating experimental data taken from 10 µm and 50 µm microspheres and 5 mm ISFIs [16, 26]. Each of these systems developed a unique geometry resulting from the phase inversion process. Rather than relying on the full geometries derived from imaging, simplified model geometries were designed to capture the most salient features of the release vehicles (i.e. shell thickness, pore size/distribution, interior matrix thickness, and implant size). One major benefit of reducing the complexity of the geometry with regard to space is that the geometric parameters can be easily modified to sweep parameter regimes for optimal conditions to produce desired drug release profiles.

Confocal images from literature were used to establish the geometric parameters of microspheres. The confocal images taken by Pack and colleagues depict completely solid 10 µm microspheres, however, the 50 µm microspheres had pores distributed throughout the volume of the release vehicle [16, 27]. To account for these random pores, the average distance of each pore from the center and the size of the pore was evaluated (17.99, 3.80 µm), along with standard

deviations (6.08, 1.48 μm), and skew (-0.65, 1.48), respectively. A skewed gaussian function was then used to randomly select the position and size of the pores throughout the implant.

To design the geometry for the 5 mm ISFI a SEM image (Fig 2a) from a 2 day old implant, well into the solidification phase, was converted to binary in Python (Fig 2b) and reduced to a simplified geometry (Fig 2c). Previous data on the swelling of each 15, 29, and 53 kDa implants was used to update the size of the implant on discrete time points [6]. The implants swelled at different rates but reached a maximum increase in cross sectional area of 2.40, 2.20, and 1.73 for 15, 29, and 53 kDa, respectively [26].

Each of the geometries for the ISFIs and microspheres were built as an array of 1s and 0s representing polymer rich and lean regions, respectively. Fig 2d shows one such array, which we refer to as a *mask*, that is then applied to the mathematical model to distinguish the spatial state of the precipitated polymer. This reduced geometry was verified to introduce negligible error, see section 3.4.

However, *mask* is only useful for a completely precipitated implant and does not take into consideration the time-varying nature of the solidification process, especially at early time points when water is still diffusing into the system.

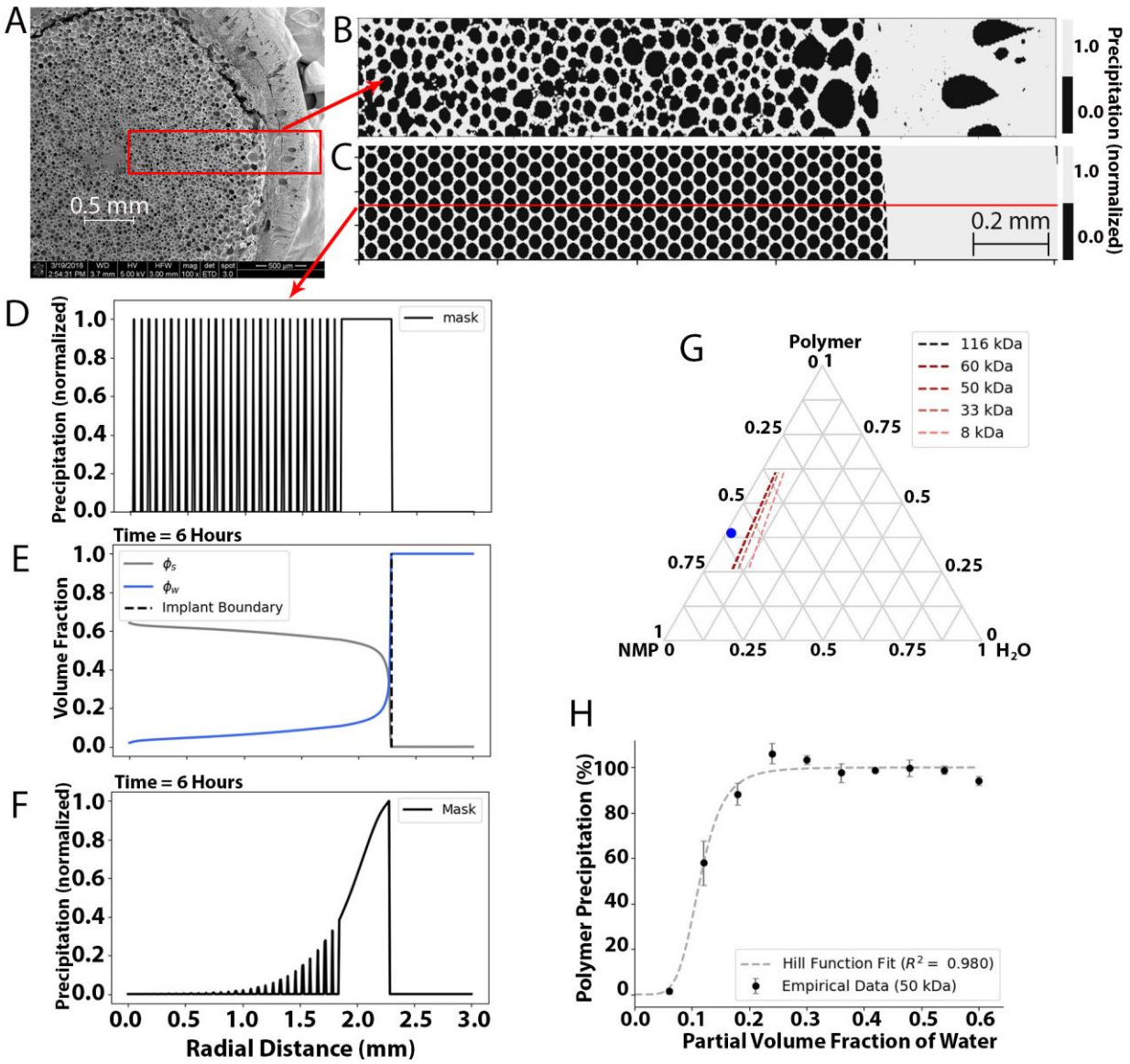

Figure 3.2. Model development of polymer solidification. (A) SEM image of a cryosectioned implant after 2 days post-exposure. (B) Binary geometry built from section of SEM image (red box in A). (C) Simplified geometry of the implant built in Python. (D) Plot of *mask* as a function of radial distance at a cross section of the simplified geometry (red line in B). (E) Volume fractions of water (φ_w) and solvent (φ_s) after 2 days in the coagulation bath as a function of radial distance; implant boundary is denoted by the dashed black line. (F) Final *Mask* function after the τ_{ter} is applied to *mask* based on the volume fractions and the ternary phase diagram. (G) Empirically derived ternary phase diagram for PLGA 50:50, data from Exner et. al [28]. Blue circle represents the initial volume fractions of the ISFIs. (H) Sample of the empirical data utilized to develop the ternary phase diagrams [28].

To model the time dependent nature of the polymer solidification, we solved for the diffusion of water in and solvent out of the implant utilizing theory for multicomponent diffusion developed initially by Maxwell and Stefan [29, 30]. The flux of polymer molecules is gradual, and the momentum imparted on the solvent and water molecules is negligible. The solidification rate, as well as the diffusivity of the solidified and dissolved polymer were considered, allowing the phase inversion to be modeled by the Maxwell-Stefan equation for an ideal, binary mixture:

$$\sum_{k=1}^{2} \frac{x_i x_k}{Đ_{ik}} (u_i - u_k) = -\frac{x_i}{RT} (\nabla_{T,P} \mu_i), \ \mathrm{i} = 1,2 \tag{1a}$$

where $x_i = c_i/c_t$, c_i is the molar concentration of component i, c_k is the molar concentration of component k, $c_t$is the total molar concentration, u_i is the molar velocity of component i, u_k is the molar velocity of component k, $Đ_{ik} = RT/ς_{ik}$, where $ς_{ik}$ is the frictional coefficient between components i and k, R is the ideal gas constant, T is the temperature of the system, and μ_i is the chemical potential. Introducing components molar fluxes N_i, driving force d_i, and flux J_i gave equation 1b:

$$\sum_{k=1}^{2} \frac{x_k J_i - x_i J_k}{c_t Đ_{ik}} = -d_i, \ \mathrm{i} = 1,2 \tag{1b}$$

which was modeled as

$$c_t \begin{pmatrix} d_1 \\ d_2 \end{pmatrix} = \begin{bmatrix} B_{1,1} & B_{1,2} \\ B_{2,1} & B_{2,2} \end{bmatrix} \begin{pmatrix} J_1 \\ J_2 \end{pmatrix} \tag{1c}$$

$$B_{ii} = \frac{x_i}{Đ_{in}} + \sum_{j \neq i}^{2} \frac{x_k}{Đ_{ij}}, \ B_{ij} = \frac{-x_i}{Đ_{ij}} + \frac{x_i}{Đ_{in}} \tag{1d}$$

[31-34]. The friction coefficients were found by using the following relationships

$$D_1 = \frac{RT}{\frac{\rho_1 ς_{11}}{Mw_1} + \frac{\rho_2 ς_{12}}{Mw_2}}, \ D_2 = \frac{RT}{\frac{\rho_2 ς_{22}}{Mw_2} + \frac{\rho_1 ς_{21}}{Mw_1}}, \ ς_{12} = (ς_{11} ς_{22})^{1/2}, \ ς_{12} = ς_{21} \tag{1e-h}$$

determined by Vrentas et. al and Bearman et. al [35, 36], where ρ_i is the density of component i and Mw_i is the molecular weight of component i.

Using equations 1c-h the mass transport of solvent and water was evaluated, while monitoring the volume fractions of each component, φ_i. The volume fractions are defined as

$$\varphi_i = \frac{Mw_i}{\rho_i} c_i \quad (2a)$$

$$\sum_{i=1}^{3} \varphi_i = 1, i = 1,2,3 \quad (2b)$$

where φ_i is the volume fraction of component i.

The solidification of the polymer was determined by overlaying the volume fractions with a ternary phase diagram, Fig 2g. The ternary phase diagrams for vary polymer Mw (Fig 2g) were developed by fitting empirical data [28] with a Hill equation (Fig 2h). The solidification was represented by the variable τ_{ter} and applied to spatially dependent variable *mask* to give a spatially and temporally dependent variable *Mask*. The function *Mask* is defined as

$$Mask = \tau_{ter} * mask \quad (2c)$$

where τ_{ter} is derived from a ternary phase diagram for PLGA, (NMP or DCM), and water, Fig 2g. Ternary diagrams produced in Fig 2g agrees with ternary phase diagrams previously published [19, 37-39].

The rate of solidification has the impact of controlling the encapsulation efficiency of microspheres [40-45], and the initial burst of drug from ISFIs [46-48], as well as the final polymer geometry formed [46].

3.4.3 Mathematical Model of Polymer Degradation

Polymer degradation occurs through the hydrolysis of linking ester bonds, which was modeled by a system of reaction-diffusion equations tracking the change in concentration of chain scission, R_s. Depending on where the chain scission occurs along the polymer chain either an oligomer, C_{ol}, or monomer, C_m, is produced. These small polymer chains are able to diffuse out of the implant,

which increases the porosity and consequently the diffusivity of the polymer. Another important characteristic of C_{ol} and C_m are that these small polymer chains terminate in a carboxylic acid end group, which further catalyzes the cleavage of ester bonds [49-51]. This produces two feedback loops: the production of C_{ol} and C_m further catalyzes the polymer degradation and increases R_s; and the diffusion of C_{ol} and C_m out of the implant increases the diffusivity of the polymer, see Fig 3.

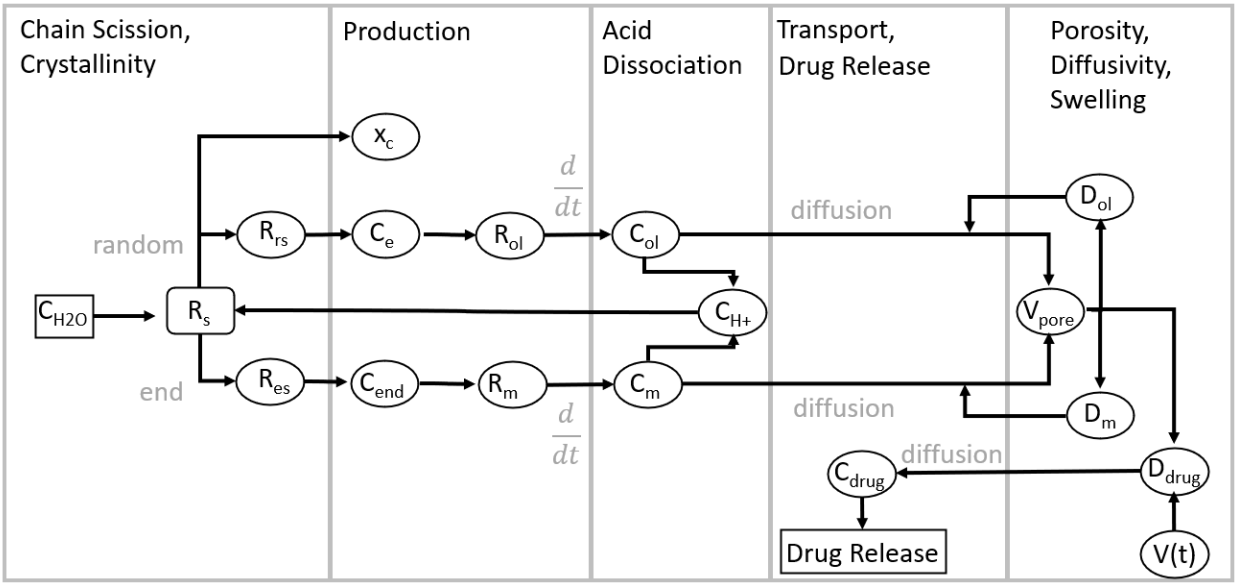

Figure 3.3. Scheme of degradation/erosion mathematical model. Water (C_{H2O}) diffuses into the implant initiating chain scission (R_s). End chain scission (R_{es}) occurs when the terminal ester bonds (C_{end}) are hydrolyzed producing monomers (C_m), while random chain scission (R_{rs}) occurs when the interior ester bonds (C_e) are hydrolyzed producing oligomers (C_{ol}). The total production of oligomers (R_{ol}) and monomers (R_m) are monitored to evaluated the porosity (V_{pore}) of the polymer which directly impacts the diffusivity of the polymer for oligomers (D_{ol}), monomers (D_m), and the loaded drug (D_{drug}). The dissociation of H^+ ions (C_{H+}) from the carboxylic acid terminals of the polymer are evaluated due to their catalytic impact on the degradation of the polymer. The swelling of the polymer (V(t)) also impacts the diffusivity of the polymer. The increase in diffusivity increases the diffusion rate of oligomers, monomers, and drug out of the implant.

Rate of Chain Scission

In developing the mathematical model for polymer degradation, we began in a similar fashion as the work of Wang et al. [49-51] with an equation to describe the rate of chain scissions per unit volume. The equation for chain scission is a function of non-catalytic and autocatalytic rate of degradation, given by:

$$\frac{dR_s}{dt} = k_1 C_{ester} C_{H_2O} + k_2 C_{ester} C_{H+} C_{H_2O} \quad (3)$$

where R_s is the concentration of chain scissions, C_{ester} is the concentration of ester bonds available for degradation, C_{H+} is the concentration of acid produced, C_{H_2O} is the concentration of water, k_1 is the non-catalytic degradation rate constant, and k_2 is the auto-catalytic degradation rate constant. Previous work assumed that water saturation of the polymer is on a much shorter time scale than degradation and erosion, and therefore not considered [49, 51-56]. However, we accounted for the time and spatial saturation of water by applying the weighting function *Mask* (section 3.2), Eq 4.

$$\frac{dR_s}{dt} = [k_1 C_{ester} + k_2 C_{ester} C_{H+}] Mask \quad (4)$$

Flory observed that polymer scission occurs through both random and end chain scission at different rates that have a varied impact on the polymer [20]. Random chain scission has the effect of dramatically reducing the average molecular weight of the polymer, while end chain scission more efficiently produces acidic byproducts. Experimental data has shown that both are necessary in modeling the degradation of polymer [52, 57-61], therefore we included both end and random chain scission, which are defined by the equations:

$$\frac{dR_{es}}{dt} = [k_{e1} C_{end} + k_{e2} C_{end} C_{H+}] Mask \quad (5a)$$

$$\frac{dR_{rs}}{dt} = [k_{r1} C_e + k_{r2} C_e C_{H+}] Mask \quad (5b)$$

where R_{es} is end chain scission, k_{e1} is the non-catalytic end scission rate constant, C_{end} is the concentration of terminal ester bonds available for end chain scission, k_{e2} is the auto-catalytic end scission rate constant, R_{rs} is random chain scission, k_{r1} is the non-catalytic random scission rate constant, C_e is the concentration of interior ester bonds available for random chain scission, and k_{r2} is the auto-catalytic random scission rate constant.

Crystallinity

To account for the observed change in crystallinity that occurs during polymer degradation, we followed the work by Han et. al, which considered the formation of crystallites, χ_c, due to the raveling of polymer chains into parallel lattice structures [53]. During the solidification of the release vehicle, the dissolved polymer has a greater degree of freedom resulting in initial crystallinity, χ_{c0}. During a chain scission, the end of the polymer has an increased flexibility and has a probability, p_c, of forming a crystallite. Work by Tsuji et. al has shown that once formed the crystallites take months to degrade, which is outside of the simulations timescale and therefore degradation of crystallites was not considered [54, 62]. The equation for unrestrained growth of crystallites, χ_{ext}, is given by

$$\chi_{ext} = p_c \eta_A R_s V_c \tag{6}$$

where η_A is Avogadro's constant and V_c is the volume of an average crystallite. To account for growth restrictions χ_{cmax} is introduced as a limiting term for the maximum crystallinity and λ is an empirically derived constant set to 1 [54].

$$\frac{d\chi_{ext}}{d\chi_c} = [\chi_{cmax} - \chi_c]^{\lambda} \tag{7}$$

$$\chi_c = \chi_{c0} - \frac{(\chi_{cmax} - \chi_c)^{\lambda}}{\lambda + 1} \tag{8}$$

Integrating Eq 7 results in Eq 8 and allows for modeling the production of crystallites during chain scission with a volume restraint [54].

Production of Acidic Byproducts

Work by Flory *et al*. used probability distributions to evaluate the average size of the polymer chains resulting from linear condensation and hinted that a similar approach would be useful in modeling random chain scissions [20]. The probability of a polymer chain of x units being produced by a chain scission is governed by the binomial probability distribution:

$$N_x = Np(1-p)^{x-1} = N_0 p^2 (1-p)^{x-1} \quad (9a)$$

where N_x is the probability of having a polymer chain of x units, N is the total number of polymer chains, p is the probability of an event, and N_0 is the total number of units. Eq 9a is then converted to a weight fraction:

$$w_x = \frac{xN_x}{N_0} \quad (9b)$$

$$w_x = xp^2(1-p)^{x-1} \quad (9c)$$

where w_x is the weight fraction of polymer chain of x units. Eq 9c is then generalized for a distribution of oligomers:

$$w_{ol} = \sum_{x=2}^{L} x(p)^2(1-p)^{x-1} \quad (9d)$$

where w_{ol} is the weight fraction of all oligomers, and L is the maximum length of mobile oligomers. Therefore, the probability function used for predicting the weight fraction of oligomers produced during random chain scission is given by:

$$\frac{R_{ol}}{C_{ester0}} = \sum_{l=2}^{L} l \left(\frac{R_s}{C_{ester0}}\right)^2 \left(1 - \frac{R_s}{C_{ester0}}\right)^{l-1} \quad (9e)$$

$$\frac{R_{ol}}{C_{e0}} = \sum_{l=1}^{L} l \left(\frac{R_s}{C_{e0}}\right)^2 \left(1 - \frac{R_s}{C_{e0}}\right)^{l-1} \quad (9f)$$

where R_{ol} is the total concentration of short polymer chains produced over reaction time, C_{e0} is the initial concentration of interior ester bonds and l is the length in ester bonds of the oligomer chain [61, 63]. In this work we continue by applying equation 9f to evaluate the production of oligomers, while Pan et. al continues by generalizing eq 9f to allow for empirical tuning [64].

The distinguishing characteristic between C_{ol} and R_{ol} is that C_{ol} is reduced when the oligomers diffuse out of the polymer matrix, while R_{ol} accounts for all the ester bonds of oligomers that have been produced. Unlike random chain scission, end scission produces exactly one

monomer during each scission event. Therefore $R_m = R_{es}$, where R_m is the total concentration of monomers produced over reaction time.

The concentration of ester bonds available for degradation is a function of both degradation and formation of crystallites. C_e is equivalent to the initial ester bond concentration reduced by the concentration of ester bonds of all oligomers and monomers formed, and the concentration of crystalline esters bonds, Eq 10a. Eq 9 was substituted into Eq 10a to producing, Eq 10b, the functional equation for the concentration of ester bonds available for random chain scission:

$$C_e = C_{e0} - (R_{ol} + R_m) - \omega\chi_c \tag{10a}$$

$$C_e = C_{e0}\left[1 - \sum_{l=2}^{L} l\left(\frac{R_s}{C_{e0}}\right)^2\left(1 - \frac{R_s}{C_{e0}}\right)^{l-1} - R_{es}\right] - \omega\chi_c \tag{10b}$$

where ω is the molar concentration of ester bonds in the crystalline phase. The concentration of terminal ester bonds available for end chain scission is determined by:

$$C_{end} = 2N_{chain0} + 2\left(R_{rs} - \left(\frac{R_{ol}}{m}\right)\right) = 2N_{chain0} + 2\left(R_{rs} - \left(\frac{1}{m}\sum_{l=2}^{L} l\left(\frac{R_s}{C_{e0}}\right)^2\left(1 - \frac{R_s}{C_{e0}}\right)^{l-1}\right)\right) \tag{11}$$

where N_{chain0} is the initial number of chains, and m is the average chain length of oligomers formed during degradation.

Acid Dissociation

Water hydrolyzes the ester bonds of the polymer to produce two new terminal groups, a hydroxyl and a carboxylic acid group. The carboxylic acid functional group has a high degree of reversible acid dissociation, thereby promoting further degradation of the polymer. The total concentration of H^+ ions distributed throughout the implant is regulated by both the acidity of the drug and the production of carboxylic acid end groups through the chain cleavage. Therefore, the concentration of H^+ ions was modeled by:

$$C_{H+} = C_{H+,polymer} + C_{H+,drug} \tag{12}$$

where the contribution of H^+ ions by the polymer, including long polymer chains, oligomers, and monomers, are defined as $C_{H^+,polymer}$, and the contribution H^+ ions by the drug are defined by $C_{H^+,drug}$.

Due to the rapid fluctuations of diffusivity of these acidic products during solidification and degradation, it is probable that diffusion can be rate controlling. It then becomes necessary to solve for acid dissociation as a time dependent event, rather than rely on an equilibrium expression. It has also been previously noted that when the diffusivity of polymer is too low, the equilibrium concentration of reactants is not maintained, and the reaction may not reach equilibrium [20]. Therefore, acid dissociation from the carboxylic acid was modeled using mass action kinetics:

$$C_{COOH} \underset{k_{off}}{\overset{k_{on}}{\rightleftharpoons}} C_{H+} + C_{COO-} \tag{13a}$$

where C_{COOH} is the concentration of acid, $C_{H+}$is the concentration of dissociated ions, C_{COO-} is the concentration of conjugate base formed, k_{on} is the rate of acid association, and k_{off} is the rate of acid dissociation. Eq. 13a was then rewritten in the form of the ordinary differential equation:

$$\frac{dC_{COOH}}{dt} = k_{on}C_{H^+}C_{COO^-} - k_{off}C_{COOH} \tag{13b}$$

which was then expanded to account for long polymer chains (C_{pol}), oligomers (C_{ol}), monomers (C_m), acidic drug (C_{Drug}), and water/buffer (C_{H2O}). The protonation of the solution from these five proton donors is represented by:

$$\sum_{k=1}^{5} C_{H+,k} \tag{14}$$

where C_{pol}, C_{ol}, C_m, C_{drug}, and C_{H_2O} are represented by k = 1,2,3,4, and 5 respectively.

Substituting Eqns 10b, 11, 12, and 14 into 5a and 5b generated the final expression for the degradation rates:

$$\frac{dR_{rs}}{dt} = C_{e0}\left[1 - \sum_{l=2}^{L} l\left(\frac{R_s}{C_{e0}}\right)^2\left(1 - \frac{R_s}{C_{e0}}\right)^{l-1} - R_{es} - \omega\chi_c\right]\left\{k_{r1} + k_{r2}\left[\sum_{k=1}^{5} C_{H+,k}\right]\right\}Mask \tag{16a}$$

$$\frac{dR_{es}}{dt} = \left[2N_{chain0} + 2(R_{rs} - \left(\frac{1}{m}\sum_{l=2}^{L} l\left(\frac{R_s}{C_{e0}}\right)^2\left(1-\frac{R_s}{C_{e0}}\right)^{l-1}\right))\right]\{k_{e1} + k_{e2}[\sum_{k=1}^{5} C_{H+,k}]\}Mask \tag{16b}$$

The analytical solution for the rate of production of the short chain polymers, $\frac{dR_{ol}}{dt}$ was determined as:

$$\frac{dR_{ol}}{dt} = \frac{d}{dt}\left(\sum_{l=2}^{L} l\left(\frac{R_s}{C_{e0}}\right)^2\left(1-\frac{R_s}{C_{e0}}\right)^{l-1}\right) = \sum_{l=1}^{L}\frac{-C_{e0}\left(\frac{R_{rs}}{C_{e0}}\right)\left(1-\frac{R_{rs}}{C_{e0}}\right)^{l-2}\left(l\left(\frac{R_{rs}}{C_{e0}}\right)+\frac{R_{rs}}{C_{e0}}-2\right)\left(\frac{dR_{rs}}{dt}\right)}{\left(\left(\frac{R_{rs}}{C_{e0}}\right)-1\right)^2} \tag{17a}$$

Every end chain scission produces a monomer so the concentration of monomers produced, R_m, is modeled by equation 17b.

$$\frac{dR_m}{dt} = \frac{dR_{es}}{dt} \tag{17b}$$

3.3.3.5 Polymer and Drug Transport

Assuming the polymer degradation products are well-mixed and soluble, the erosion of C_m and C_{ol} was modeled by the conserved form of Fick's second law of diffusion to account for the non-homogeneous material. The diffusion-reaction equations for C_{ol} and C_m become:

$$\frac{dC_{ol}}{dt} = \frac{dR_{ol}}{dt} + \sum_{i=1}^{3}\frac{\partial}{\partial x_i}\left(D_{Col}(x_i,t)\frac{\partial C_{ol}}{\partial x_i}\right) \tag{18a}$$

$$\frac{dC_m}{dt} = \frac{dR_{es}}{dt} + \sum_{i=1}^{3}\frac{\partial}{\partial x_i}\left(D_{Cm}(x_i,t)\frac{\partial C_m}{\partial x_i}\right) \tag{18b}$$

Diffusion of drug, H^+ (which is transported as hydronium), and the conjugate bases out of the system were modeled in a similar manner with a conserved form of Fick's second law of diffusion, represented by ψ. The diffusion terms are then rewritten for a spherical coordinate system:

$$\sum_{i=1}^{3}\frac{\partial}{\partial x_i}\left(D\frac{\partial C}{\partial x_i}\right) = \frac{1}{r^2}\frac{\partial}{\partial r}\left[Dr^2\frac{\partial \psi}{\partial r}\right] + \frac{1}{r^2 sin\theta}\frac{\partial}{\partial \theta}\left[Dsin\theta\frac{\partial \psi}{\partial \theta}\right] + \frac{1}{r^2\sin\theta^2}\frac{\partial}{\partial \phi}\left[\frac{\partial \psi}{\partial \phi}\right] \tag{19}$$

and reduced to a one dimensional equation, which was applied to all of the simulation present in this study, with the exception of the geometric reduction studies in section 3.4:

$$\sum_{i=1}^{1} \frac{\partial}{\partial x_i}\left(D\,\frac{\partial C}{\partial x_i}\right) = \frac{1}{r^2}\frac{\partial}{\partial r}\left[Dr^2\,\frac{\partial \psi}{\partial r}\right] \tag{20}$$

3.3.3.6 Porosity/Diffusivity of Polymer

Following the work by Pan *et. al [55]*, the porosity of the polymer matrix was defined by the loss of drug and short polymer chains from the release vehicle, evaluated by the equations:

$$V_{pore,ol,m} = \frac{R_{ol}+R_m}{C_{e0}} - \frac{C_m+C_{ol}-C_{ol0}-C_{m0}}{C_{e0}} \tag{21a}$$

$$V_{pore,drug} = 1 - \frac{C_{drug}}{C_{drug,0}} \tag{21b}$$

The contribution of each is proportional to f_{Drug}, which is the volume ratio of drug to polymer. Therefore, the final equation for porosity was given by Eq. 22 [55].

$$V_{pore} = V_{pore,ol}\left(1 - f_{drug}\right) + V_{pore,drug} f_{drug} \tag{22}$$

The diffusivity of the polymer was modeled as:

$$D = D_{polymer} + \left(1.3V_{pore}^2 - 0.3V_{pore}^3\right)\left(D_{pore} - D_{polymer}\right) \tag{23}$$

where $D_{polymer}$ is the diffusivity of a component (ie. drug, water, polymer degradation products, etc.) through pure polymer, and D_{pore} is the diffusivity of a component (ie. drug, water, polymer degradation products etc.) through dissolved polymer [62].

For the ISFI, significant swelling was observed, and to account for the increased diffusivity of the polymer during the swelling of the implant we modified equation 23 to account for free-volume theory. The relationship between polymer diffusivity and the implant volume expansion is based on the generalized free-volume theory proposed by Fujita et al. [65-67] based on work by Turnbull and Cohen [24], and further developed by Peppas et al. [68-74]. The function for the polymer diffusivity was

$$D(t) = D_0 * e^{-\beta_{sw}\left(1-\frac{V(t)}{V_0}\right)} \tag{24a}$$

where D(t) is the polymer diffusivity as a function of time, D_0 is the equilibrium polymer diffusivity, V(t) is the polymer volume as a function of time, V_0 is the initial polymer volume, and an empirical term (β_{sw}) [69-72].

$$D_{polymer} = D_{polymer,0} * e^{-\beta_{sw}\left(1-\frac{V(t)}{V_0}\right)} \tag{24b}$$

$$D = (1 - Mask) * D_{pore} + Mask * \left[D_{polymer,0} * e^{-\beta_{sw}\left(1-\frac{V(t)}{V_0}\right)} + \left(1.3V_{pore}^2 - 0.3V_{pore}^3\right)\left(D_{pore} - D_{polymer,0} * e^{-\beta_{sw}\left(1-\frac{V(t)}{V_0}\right)}\right)\right] \tag{24c}$$

The final equations 2a, 16a-b, 18a-b, 22, 23, and 23/24c are solved as a system of PDEs to evaluate the drug release rate from the release vehicles.

It becomes important to recognize that the diffusivity of the polymer is a function of φ_i, C_{ol}, C_m, and C_{drug} (acting as a feedback loop) and thereby is a spatially and temporally dependent function. This also means that the PDE governing mass transport is nonlinear and must be treated with great care to reach a stable and accurate numerical solution.

3.4.4 Verification of Geometry Reduction

In creating the simplified time-dependent geometry of the model it was necessary to verify that each of the following assumptions or simplifications did not introduce significant error: (1) reduction of the dimensionality of the model to one spatial dimension, (2) use of a simplified spatial geometry without the random shell pores, and (3) use of a stochastic model for the internal pores in the 50 μm implant.

Reduction of spatial dimensions

COMSOL was used to simulate the diffusion drug out of a solid three dimensional spherical implant, Fig 4a, which was directly compared to a Python simulation of the radial drug diffusion out of the implant, Fig 4b. The initial drug concentration was set to high order polynomial depicted by the darkest navy line in Fig 4b. This was necessary in the COMSOL simulation to prevent the software's treatment of a discontinuous variable, which dramatically impacts the model results. The drug release rates from these two simulations were compared in Fig 4c. The use of a model with a single spatial dimension of radial diffusion introduced a maximum of 0.949% error.

ISFI Geometry Simplification

SEM images of the fully solidified implant were imported into Python where the images were converted into binary, with 1 representing polymer matrix and 0 the pores. The drug released from the simplified geometry (Fig 4d) and the SEM geometry (Fig 4e) where compared to verify that no significant source of error was being introduced, Fig 4f. The reduction of the geometry derived from SEM images to the simplified geometry introduced a maximum error of 0.864% with the inclusion of shell pores, and 8.048% when the shell pores are excluded, Fig 4d-f.

Microsphere Geometry Simplification

Experimental data collected by Pack et. al determined that not only do 50 μm microspheres contained randomly distribution of interior pores, but that the loaded drug was heterogeneously distributed in these pores [16]. The experimental data was used to build a COMSOL simulation for the diffusion of drug out of 2D slice geometry, Fig 4g. To reduce the complexity of the model the distribution of the pores was analyzed and applied to a Python model for a single spatial dimension, Fig 4h. The drug released from the 2D COMSOL simulation (solid grey line) and the stochastic 1D Python simulation (solid blue line), in the absence of polymer degradation, are compared to experimental data, Fig 4i [16]. These two simulation results are also compared to the drug released from a 1D Python simulation with a homogeneous initial drug distribution (dashed blue line), Fig 4i. With a single spatial dimension, stochastic model for the random distribution of pores in the 50 μm implant introduced a maximum error of 3.230%, while modeling a homogeneous initial drug distribution produced a maximum error of 20.440%, Fig 4g-i.

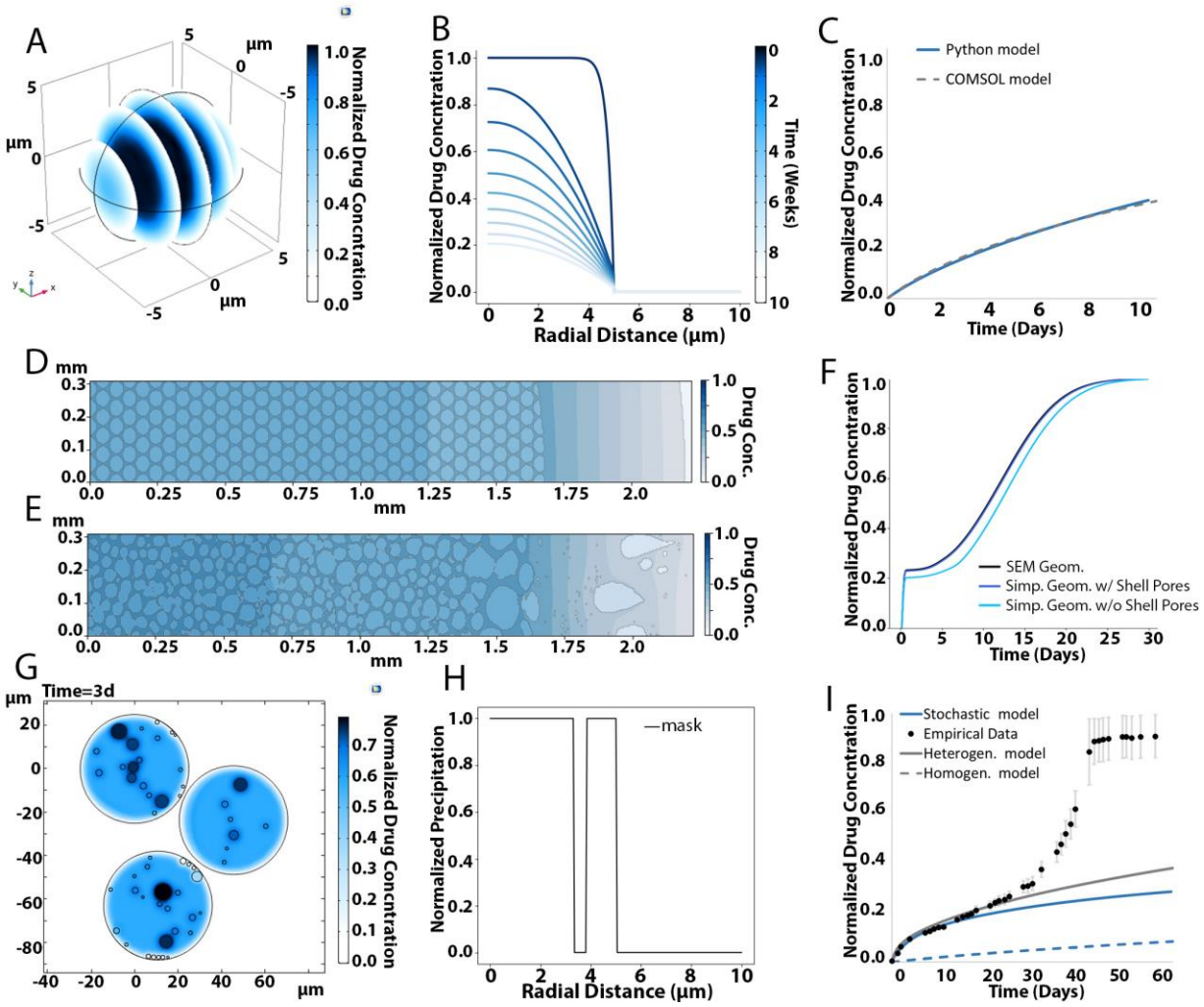

Figure 3.4. Numerical Verification. (A) COMSOL simulation out of a sphere in three spatial dimensions. (B) Python simulation out of a sphere in a single spatial dimension. (C) Overlaying drug release predictions from A and B. (D) Python simulation for drug diffusion out of simple 2D slice geometry of an ISFI, 2 days post-exposure.(E) Python simulation for drug diffusion out of a complex 2D slice geometry derived from SEM images of an ISFI, 2 days after formation. (F) Overlaying the entire 30 day time course of drug released from the 2D geometries shown in D and E. (G) COMSOL simulation for drug diffusion out of 50 μm microsphere with a 2D slice geometry derived from confocal images, 6 hours after formation [16]. (H) A single geometry from the Python stochastic simulation for radial diffusion out of the 50 μm microsphere. (I) Comparison of the drug released from 2D COMSOL simulation (solid grey line), 1D stochastic heterogeneous Python simulation (solid blue line), 1D homogeneous Python simulation (dashed blue line), and experimental data for 67 kDa 50 μm microsphere [16]. FIX COLORS BLUE AND GREY

3.4.5 Model parameterization

In developing this model two sets of unknown parameters are introduced: the diffusivity of oligomer, monomers, water, solvent, and the loaded drug through the polymer; and the four degradation rates of the polymer.

Model parameterization: diffusivity

Reviewing literature data of drug release profiles from vehicles of varying combinations of drugs and PLGA50:50 Mw allowed us to develop an empirical equation for the diffusivity as a function of drug and polymer Mw [21, 28, 56, 75-87], Fig 5a. The data was found to be best fit by an exponential function, Fig 5b. This function was then used to approximate individual diffusion coefficients for the diffusion of NMP and dichloromethane (DCM); the degradation products oligomers and monomers; and drugs Fluorescein and Piroxicam through solid polymer, $D_{polymer.}$

Fluorescent recovery after photobleaching (FRAP) was performed to measure the diffusivity of fluorescein in 53 kDa dissolved polymer (1.387e-6 m^2/day) and water (5.356e-6 m^2/day), Table S1. The arithmetic mean was taken for the diffusion of the loaded drug through polymer pores, see table S1. Diffusion weighted imaging (DWI) was used to measure the diffusivity of water in the solidifying polymer. The diffusivity ranged from 3e-10 m^2/s (solid polymer matrix) to 2e-9 m^2/s (degraded polymer solution). These values were used to parameterize the diffusivity of water, hydroxide, and H+ (which exists as hydronium) through the solidified polymer and soluble polymer pores (Dpore and Dpolymer, respectively for each component). The Stokes-Einstein equation was then used to approximate the values of D_{pore} for the solvent, monomers, and oligomers.

Model parameterization: degradation rate constants

The degradation rates (k_{e1}, k_{e2}, k_{r1}, k_{r2}) for the polymer were approximated by fitting the degradation profiles for the 50 μm implants with empirical data, Fig 5c-f [16]. The values for these rates were determined to be: $k_{e1} = 3.75e-3\ m^3/(mol*day)$, $k_{e2} = 3e-6\ m^6/(mol^2*day)$, $k_{r1} = 7e-6\ m^3/(mol*day)$, and $k_{r2} = 1e-2\ m^6/(mol^2*day)$. Allowing initial

crystallinity of each Mw implant to vary with the final Mn allowed for accurate fits (Fig 5c-f), parameter values can be found in table S5.

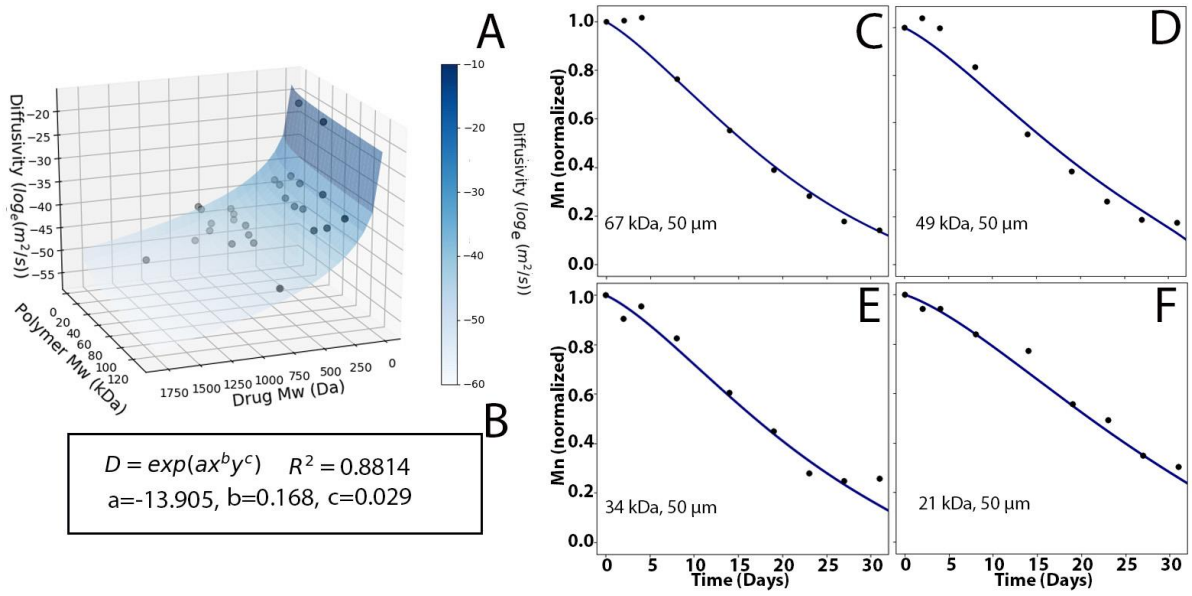

Figure 3.5. Model Parameterization. (A) Experimental data collected from a literature review of PLGA 50:50 nanoparticles and small microspheres were used as a training set for the polymer diffusivity as a function of the Mw of the polymer and the analyte. [21, 28, 56, 75-87]. (B) The equation used in the regression analysis along with the parameters fits and the R^2 value. (C-F) The degradation profile of 67, 49, 34, and 21 kDa, PLGA 50:50 polymer 50 µm microspheres, respectively was used to parameterize the degradation rate constants (k_{e1}, k_{e2}, k_{r1}, k_{r2}) [16].

3.3.6 Model Verification

With the diffusivities through polymer matrix and pores, and the degradation rates parameterized, the predictive capability of the model was evaluated. Simulations were compared against a host of experimental data including: drug release profiles and encapsulation efficiencies of 10 µm microspheres; drug release, degradation, and mass loss profiles of 5 mm ISFIs; and the pH distributions and encapsulation efficiencies of 50 µm microspheres of varying Mw [16, 21, 26, 88].

Solidification Model Verification

To verify the accuracy and predictive capabilities of the solidification model, simulation results were compared to four sets of empirical data: DWI data for the 5 mm implants, early drug release

from the 5 mm implants, and the encapsulation efficiencies of both the 10 and 50 μm implants, Fig 6.

DWI data of 15 and 53 kDa PLGA 5 mm implants was sampled at 0.25, 1, 2, 3, 7, and 10 days post-exposure. Early time points (0.25-3 days) are shown in Fig 6a and 6b. The DWI images show the formation of a solid polymer shell for both Mw polymers within a day, which is maintained over weeks, while the core of the implant solidifies over days but decays within a week. For the 53 kDa polymer, the solvent, which is evident by the dark blue regions of the MR images (Fig 4a), takes much longer to leave the implant thereby delaying the formation of the core over three days and its subsequent degradation. By contrast, the solvent leaves the low Mw polymer implant within a day allowing the core of the implant to form within the first day, and the core degrades within the first three days.

During solidification, the model predicts the time scales of polymer solidification of both the 15 and 53 kDa polymers shown by the rapid transition from liquid to solid polymer in the ternary phase diagram, Fig 6c-e. The grey boxes around the time points in the ternary phase diagrams correspond to the respective DWI images in Fig 6a,b. To verify that the model was able to predict the drug release rates, simulations of 15, 29, 53 kDa 5mm ISFIs was compared to experimental data, Fig6f-h. Absolute error between experimental measurements and model predictions averaged over the first 3 days was found to be 3.514, 3.167, and 2.057%, respectively, giving an average absolute error for the 5 mm implants of 2.913%, Fig 6f-h [26].

The respective manufacturing processes for producing microspheres was also considered. To produce the microspheres a stream of codissolved PLGA and drug were broken up by acoustic excitation into uniform spheres, which were collected in a bath for 3 hours to solidify. These implants were then lyophilized for 2 additional days to ensure the removal of solvent and water [16, 17]. This process was simulated by the model to increase the accuracy of the overall simulation and to verify the solidification model by predicting the encapsulation efficiency that was measured experimentally by Pack et. al [16]. The solidification rates used for the ISFIs (Fig 2g) were also used for modeling the microsphere solidification, except for the solidification rate for the 15 kDa, which would result in the complete loss of drug. The model predicted the encapsulation efficiencies of 6.5, 21, 34, 49, and 67 kDa 10 μm implants, as well as 21, 34, 49, and 67 kDa 50 μm implants, see Fig 6i-j, with an average absolute error of 10.767% and 11.044% for the 10 and 50 μm implants, respectively.

Figure 3.6. Solidification Model Verification. (A) DWI data for a 15 kDa, 5 mm implant collected over the first 3 days (B) DWI data for a 53 kDa, 5 mm implant collected over the first 3 days. Regions of dark blue indicate the retention of solvent and a slower solidification process. (C) Ternary phase diagrams overlaid with experimentally derived binodal line (dashed blue) and the predicted volume fractions of a 15 kDa, 5 mm implant as 0, 1, 6, 24, 48, and 72 hours post-exposure. Gray boxes correspond to 6, 24, 48, and 72 hours post-exposure in increasing lightness. (D) Ternary phase diagrams overlaid with experimentally derived binodal line and the predicted volume fractions of a 29 kDa, 5 mm implant as 0, 1, 6, 24, 48, and 72 hours post-exposure.(E) Ternary phase diagrams overlaid with experimentally derived binodal line and the predicted volume fractions of a 53 kDa, 5 mm implant as 0, 1, 6, 24, 48, and 72 hours post-exposure [28]. Gray boxes correlate to 6, 24, 48, and 72 hours in increasing lightness. (F) Empirical data for the drug released from a 15 kDa, 5mm implant (dots) is compared to model prediction (solid line) over the first 5 days [26]. (G) Empirical data for the drug released from a 29 kDa, 5mm implant (dots) is compared to model prediction (solid line) over the first 5 days [26]. (H) Empirical data for the drug released from a 53 kDa, 5mm implant (dots) is compared to model prediction (solid line) over the first 5 days [26]. (I) Empirical data for the encapsulation efficiencies for varying polymer Mw (6.5, 21, 34, 49, and 67 kDa) for 10 μm implants (grey bars) compared to model prediction (blue bars) [16]. (J) Empirical data for the encapsulation efficiencies for varying polymer Mw (21, 34, 49, and 67 kDa) for 50 μm implants (grey bars) compared to model prediction (blue bars) [16].

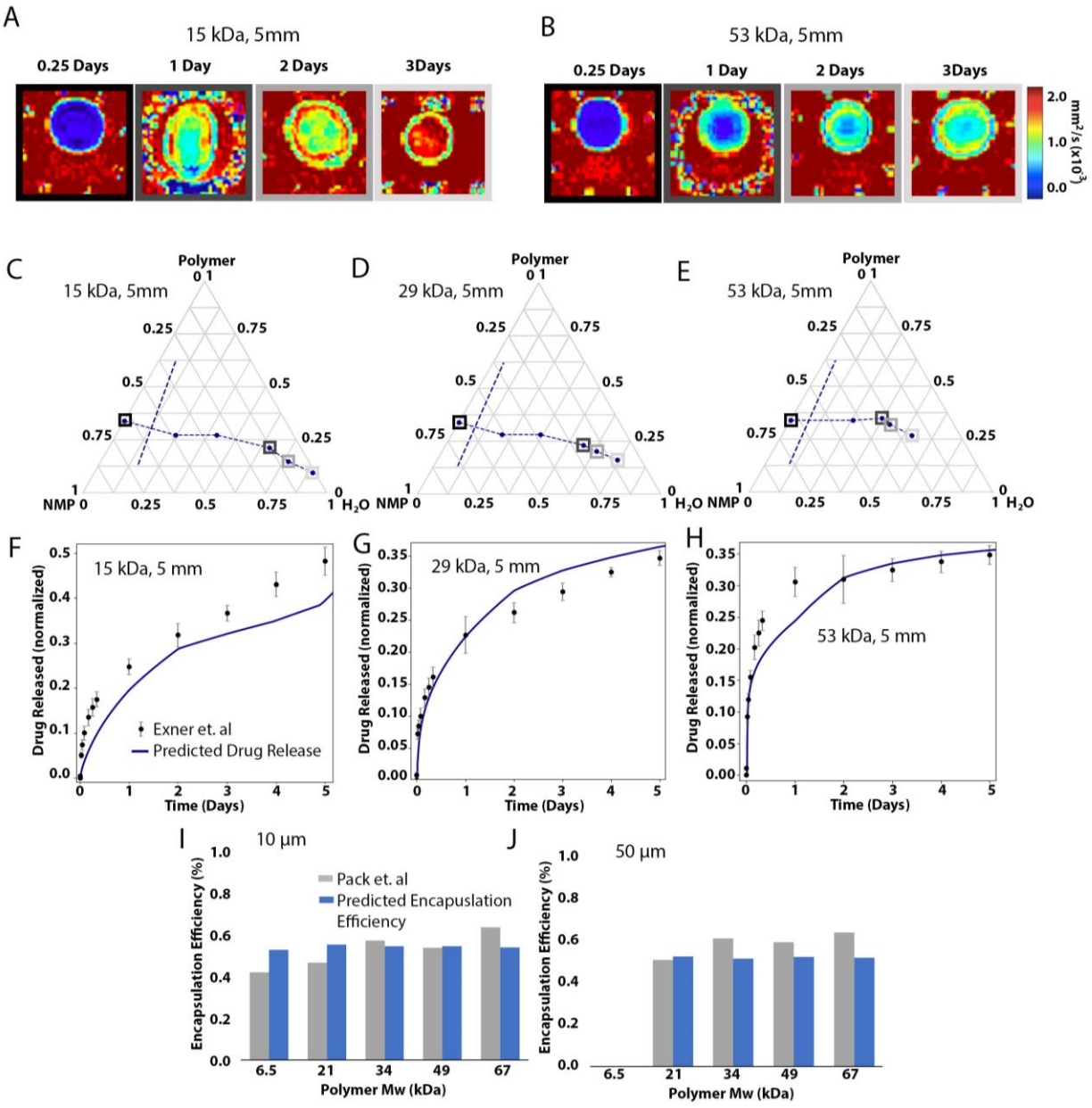
A
15 kDa, 5mm
0.25 Days
1 Day
2 Days
3Days
B
53 kDa, 5mm
0.25 Days
1 Day
2 Days
3Days
2.0
1.0
0.0
mm²/s (x10⁻³)
C
15 kDa, 5mm
D
29 kDa, 5mm
E
53 kDa, 5mm
Polymer
NMP
H₂O
F
15 kDa, 5 mm
G
29 kDa, 5 mm
H
53 kDa, 5 mm
Drug Released (normalized)
Time (Days)
Exner et. al
Predicted Drug Release
I
10 µm
J
50 µm
Pack et. al
Predicted Encapsulation Efficiency
Encapsulation Efficiency (%)
Polymer Mw (kDa)

Degradation Model Verification

To verify the accuracy and predictive capabilities of the polymer degradation model, the simulation results were compared to five sets of empirical data: drug release from 10 μm implants, drug release and pH distribution within 50 μm implants, drug release and mass loss from 5 mm implants.

Drug release rates from 6.5, 21, 34, 49, and 67 kDa 10 μm microspheres were simulated and compared to previous data [16], Fig 7g-k. The absolute error between predicted and measured values were 14.349, 8.000, 7.136, 4.9090, and 3.453%, respectively (Fig 7g-k solid navy lines). Giving an average absolute error of 7.590%. The polymer diffusivity was then allowed to vary slightly to match early time points of the experimental data, see Fig 7g-k, without degradation (dashed grey lines). These values were then used to quantify error in the model prediction of polymer diffusion coefficients (Fig 5b). All values for parameters can be found in table S5. The predicted values for polymer diffusivities for the 10 μm implants were predicted with an average relative error of 41.351%.

The model predicted the drug release rate from the 21, 34, 49, and 67 kDa 50 μm microspheres with an absolute error of 8.950, 7.583, 6.353, and 3.949% respectively, see Fig7a-d (solid navy lines) [16]. With an average absolute error of 6.709%, however, with the corrected drug diffusion coefficients, found in Fig 7g-k (dashed grey lines), the average error for the 50 μm implants decreases to 4.333% (Fig 7a-d dashed blue lines). The average position of pores for the 21, 34, and 49 kDa implants were also allowed to vary within 10% to match the experimental data, see Fig 7a-d (dashed grey lines). By explicitly modeling the polymer degradation process and acid dissociation, we were able monitor the pH change of the implant, which influences the conformation and the potency of the drug [89-91]. Experimental data from Liu et al was compared to the pH gradient predicted by the model, Fig 7e-f [88]. Predicted pH values were spatially averaged and compared to measured pH values; resulting in a relative error of 3.688%.

Figure 3.7. Degradation Model Verification. (A-D) Empirical data for the drug release of 21, 34, 49, and 67 kDa, 50 μm implants is compared to model predictions using the determined degradation parameters and diffusivity function (solid navy). For the 21 and 34 kDa, 50 μm implants the average position of the pores was shifted from 17.99 to 19.50 μm (dashed blue) [16]. (E-F) Comparison of the spatial average pH in the 50 μm implants from data collected by Liu et al. for 7, 14, 21, and 28 days [88] compared to model predictions. (G-K) Empirical data for the drug release of 6.5, 21, 34, 49, and 67 kDa, 10 μm implants is compared to model predictions using the determined degradation parameters and the diffusivity function (solid navy). Polymer diffusivity values are also allowed to vary to determine error in the diffusivity function, with degradation (dashed blue) and without degradation (dashed grey) [16].

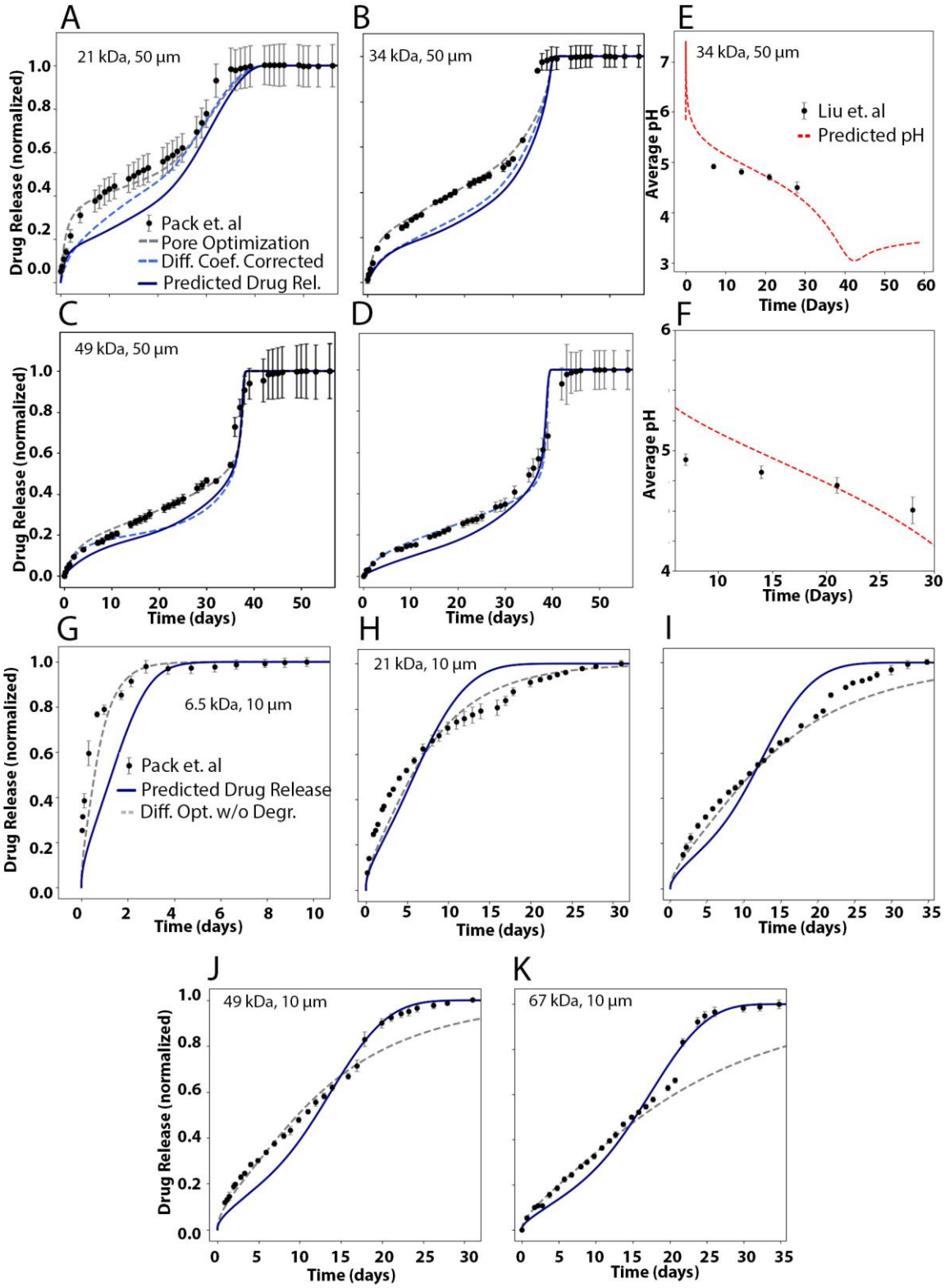
A
21 kDa, 50 µm
Drug Release (normalized)
Pack et. al
Pore Optimization
Diff. Coef. Corrected
Predicted Drug Rel.
B
34 kDa, 50 µm
E
34 kDa, 50 µm
Liu et. al
Predicted pH
Average pH
Time (Days)
C
49 kDa, 50 µm
Drug Release (normalized)
Time (days)
D
Time (days)
F
Average pH
Time (Days)
G
6.5 kDa, 10 µm
Pack et. al
Predicted Drug Release
Diff. Opt. w/o Degr.
Drug Release (normalized)
Time (days)
H
21 kDa, 10 µm
Time (days)
I
Time (days)
J
49 kDa, 10 µm
Drug Release (normalized)
Time (days)
K
67 kDa, 10 µm
Time (days)

To verify that the model can account for implants of larger size (5mm) the model predictions were compared to experimental data for the drug release, see Fig 8d-f, and mass loss profiles, see Fig 8g-i. Phase diagrams, Fig 8a-c, allow us to not only understand the impact of the solidification process in terms of volume fractions, but also the impact of polymer degradation and swelling on the partial volume fractions. Each individual phenomenon has a different impact on the phase transition which can clearly be seen by the 53 kDa ISFI (Fig 8c black arrows). Phase inversion causes the volume fraction of water to increase, while the volume fraction of polymer remains constant. Swelling increases this exchange, while also decreasing the polymer volume fraction. Degradation causes the volume fraction of water to increase, while the volume fraction of solvent remains constant.

The drug release profile for the 15, 29, and 53 kDa implants were predicted with a time average absolute error of 7.300,9.295, and 5.961% respectively, see Fig 8d-f (solid navy lines). With an average absolute error of 7.519 %. The impact of the swelling parameter for the diffusion of hydronium was evaluated by setting $ß_{CH} = 0$, see Fig 8d-f (dashed blue lines). The value of the swelling parameter was allowed to very, see Fig 8d-f (solid grey lines), values are reported in table S5. Mass loss of the 15, 29, and 53 kDa were predicted with an absolute error of 4.778, 5.224, and 6.080%. Giving an average absolute error of 5.36%.

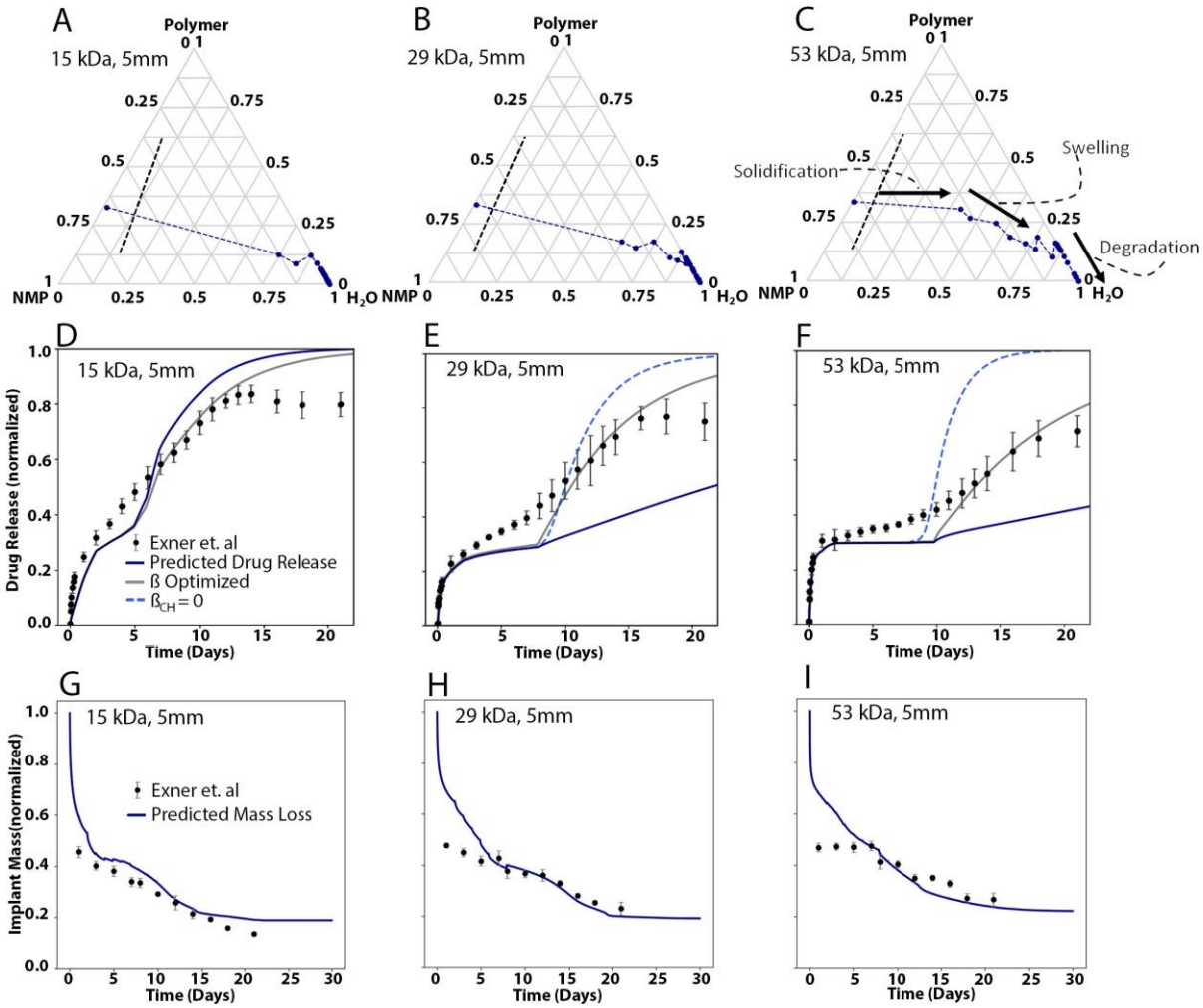

Figure 3.8. Degradation Model Verification. (A-C) Ternary phase diagrams overlaid with experimentally derived binodal line (dashed black) and the predicted volume fractions of a 15, 29 and 53 kDa, 5 mm implant sampled every day for 4 weeks (dots) [28]. Black arrows indicate the impact of solidification, swelling, and degradation on the volume fractions. (D-F) Empirical data for the drug release of 15, 29, 53 kDa, 5 mm implants compared to model predictions (solid navy). Swelling parameter values are also allowed to vary to determine error in the estimation of β (solid grey). The impact of the accelerated release of C_{H+} due to swelling was evaluated by setting $ß_{CH}$ = 0 (dashed blue). (G-I) Mass loss of the ISFIs are also predicted by the model (solid navy) [26].

3.4.6 Parameter Variation and Model Sensitivity Analysis

To quantify the impact of the variation of each model parameter on the drug release profiles, we performed global parameter sensitivity analysis using Latin Hypercube Sampling with quantification using partial correlation coefficient (PRCC) analysis [92, 93]. Two global sensitivity analyses were run for both the microspheres and ISFIs for the entire time course of drug release to evaluate the impact of variation in diffusivity of each mobile molecule in the system and polymer

degradation rates (see section 3.5) on drug release, respectively (Fig S3, S4). PRCC results in correlation coefficients that relate the variation in parameter input with the variation in model output, with 1 being perfect positive correlation, and -1 being perfect negative correlation. The PRCC data showed that for the microspheres (10 μm), the non-catalytic end and auto-catalytic random scission rates (ke1, kr2) had the greatest impact on model results (Fig S3), while in the ISFIs (5mm) the auto-catalytic degradation rates have a larger impact on the drug release profile (Fig S4). The microspheres were profoundly impacted by the diffusion coefficient for the diffusion of drug through the solid polymer, while the ISFIs were only affected by variations in this parameter for the first day post-exposure. The ISFIs were more greatly affected by the diffusion coefficient for oligomers and monomers than the microspheres, Fig S3 and S4.

3.5 Discussion

Using the mechanistic model, we were able to investigate the impact of specific aspects of the controlled release vehicle's geometry, mobile molecule diffusivity, and polymer degradation on drug release profiles. These investigations were able to produce significant insight into the aspects of these polymeric systems that can be manipulated to produce desired dynamics of drug release.

3.5.1 Model Geometry

To accurately predict the drug release from controlled release vehicles, prior knowledge of the solidified geometry was required. For the 10 μm microspheres, the implants were completely solid and had a uniform drug distribution. The 50 μm implants were not solid but had randomly positioned as well as randomly sized pores which followed a skew-normal distribution.

Accounting for the localization of drug in the pores and through the polymer matrix of the 50 μm implant allowed for the accurate modeling of the microspheres. Without this non-uniform drug distribution it would be impossible to unify the 10 and 50 μm microspheres, Fig 4i. Therefore, there is a need for a model to simulate phase inversion and accurately predict the geometry of the solidified implant and the drug distribution throughout the implant.

Our DWI data shows that unlike the microspheres, which solidified within 3 hours, the ISFIs require 3 days to solidify (Fig 6a,b), resulting in the formation of a complex structure. The

most salient features of the 5 mm ISFIs, Fig 2a, were the shell thickness and the radius of the implant. The interior pores had an insignificant impact on the degradation and drug release profiles, Fig 4d-f. However, the impact of the shell pores was not negligible introducing an average error of 8% (Fig 4f). Furthering the need for a simulation to predict the formation of these pores.

We found that the swelling of these implants, which was quantified by the Exner lab [26], had a significant impact on the diffusivity of the polymer, see Eq 24b and Fig 7. Without including swelling, the simulation was unable to predict the sustained release of the 15 kDa implant. The sustained drug release profile was not able to be predicted by, an increased degradation rate due to the positive feedback of auto-catalytic degradation. Including swelling in the model not only provided a more prolonged release of drug (Fig 8d-f) as compared to a pure degradation model (Fig 7a-d,g-k), but also reduces degradation by releasing acidic byproducts out of the polymer matrix (Fig 8d-f dashed line). Therefore, not only will further development into the impact of swelling on polymer diffusivity will be critical in reducing model error, but understanding the relationship will be key in designing implants with specific drug release profiles.

3.5.2 Model Parameterization Diffusivity/Degradation

Functionalizing the relationship between the PLGA Mw and the polymer diffusivity has not only been critical in predicting the drug release from the variety of implants but allows for future work to approximated diffusion coefficients for a variety of diffusion controlled release applications.

Previous work by Pack et. al. estimated this relationship for the 10 and 50 μm separately. While the values were close and even identical for the higher MW polymers, the diffusivity of low Mw polymers was inconsistent between the different implant sizes. The goal of our project was to develop a unified model for any size and MW implant. Accounting for the localization of drug concentration in the randomly distributed pores was crucial in unifying the microsphere models, Fig 4g-i.

The function for diffusivity, Fig 5b, was found to predict the diffusivity coefficient of piroxicam in 6.5, 21, 34, 49, and 67 kDa PLGA 50:50 with an average error of 45.950 %.This error while seemingly large is reasonably small when considering that the value of diffusivity varies over 11 orders of magnitude from the diffusion of water to the diffusion of a large drug such as clarithromycin. The PRCC analysis determined that although including the varying polymer

diffusivity was critical to the model, the diffusivity of the drug through the polymer was negligible compared to that of the solvent and oligomers. Therefore there is a need to carefully quantify the transport of polymer byproducts as well as the effect of varying organic solvents on the release of drug from the implants.

Although, allowing each of the degradation rates to vary based on polymer Mw would have led to a better fit in Fig 4a-d and a better prediction in Fig 7g-k (dashed blue lines), it was viewed as unmechanistic and an overparameterization of the model. The relationship between the end and random chain scission rate were consistent with predictions made by Flory [20] who believed that end scission occurred an order of magnitude faster than random scission. The model suggests that between a pH of 5 and 4, Fig 7f-g, end scission occurred 68x to 11x more often than random scission.

3.5.3 Auto-catalytic degradation

Degradation of PLGA through the cleavage of esters bonds has the important consequence of producing acidic byproducts, which then further enhances chain scission. The impact of auto-catalytic degradation can be seen, in the 5 mm ISFI, when comparing the degradation of the polymer shell to that of the core (Fig S5), and when observing the degradation in the walls of the interior pores of the implant (Fig S6a). Experimental DWI and SEM data, show extensive degradation and erosion of the interior of implant, while the shell retains structurally integrity for the first 10 days (Fig S5). After 10 days, the shell rapidly degrades until its rupture at day 17.

While the core of the implant sustains the most rapid degradation as a whole, the wall between the interior pores sustains the greatest rate of degradation, which is seen in Fig 14a. Rather than the pores exclusively breaching where it was the thinnest, they broke open where the most bulk polymer was, for example at the intersection of four pores in a hexagonal close-packed structure (Fig S6). This increased degradation is due to the auto-catalytic nature of the PLGA copolymer degradation and the increased concentration of H^+ ions in the nucleation site (Fig S6a, S6b). The computational model predicts the highest concentration of polymer chain scission to take place in these nucleation sites (Fig 6c) due to the inclusion of the auto-catalytic degradation term in Eq. 1. The importance of the autocatalytic degradation for the large ISFIs is quantitatively reaffirmed by the results of the PRCC analysis where k_{e2} has the greatest correlation with drug released from the implant, Fig S4. The microspheres show a more uniform distribution of acid, Fig

S3, and are more impacted by the non-catalytic degradation rate k_{e1}. The PRCC data reaffirmed the need for considering all four unique degradation rates.

Evaluating the production and diffusion of H^+ ions rather than estimating them as a lumped constituent with the oligomer, and drug [52, 57-60]allowed the model to predict the pH change within the implant (Fig 7e-f) and evaluate the impact on polymer degradation and drug release. pH change within the implant can be also particularly important parameter to consider when designing patient-specific or treatment-specific controlled release vehicles, as some tissues do not have significant rates of clearance to tolerate highly acidic systems.

Previous literature has modeled polymer degradation with a single first/second order decay term [16, 51, 55, 56, 75]. However, the experimental data and model predictions developed in this work, demonstrate that to fully understand, and therefore control, the degradation of the implant it becomes necessary to not only consider end and random scission, but also noncatalytic and autocatalytic degradation [52, 58].

3.5.4 Modeling error

Numerical solutions of the governing PDEs in Python proved to be a reliable computational model for predicting the drug release rate of the implant for varying PLGA molecular weights, and size. Model error, on the drug release profile, introduced by reducing the geometry to the simplified model was determined to be an average of 0.864% with shell pores and 8.048% without. A mesh convergence study quantified the numerical error introduced by the algorithm at 0.111%, and 0.787% error was introduced in the stochastic model for the 50 μm microspheres, see Fig S7.

The solidification model was shown to be accurate within a 3.341% average error in predicting the drug release from ISFIs in the first 3 days, however there was 10.767 and 11.044% error in predicting the encapsulation efficiency of the 10 and 50 μm microspheres, respectively. Also the solidification rate for the lowest molecular weight microspheres utilized the data for the solidification of the 29 kDa ISFIs rather than the 15 kDa ISFIs. There is also significant error in predicting the early mass loss from ISFIs, see Fig 8g-I, which is due to a higher retention of solvent than the empirical data suggests. These differences in model prediction versus experimental data on solvent diffusion indicate that the solidification model used in this project was much too simple to completely explain this phenomenally complicated process, emphasizing the need for a future work on a mechanistic model of polymer solidification.

The degradation model was also quite accurate with an average of 7.842% error in predicting the drug release profile of the 5 mm ISFIs (excluding the first 3 days), and an average of 8.003% error in predicting the drug release from the 10 μm microspheres. There was, however, notable error in the late stage release profiles of the 5 mm ISFIs. The divergence from predicted values after 15 days for the 5 mm ISFIs is likely due to the difficulties in collecting experimental data for the later time points. The computational model is developed having a perfect sink 1 mm away from the surface of the implant, however, the empirical data shows that this particular ideal sink condition was not satisfied [26]. This would account for the steepness of the simulated release profile as compared to the experimental data.

3.6 Conclusion

Given the high potential for controlled release vehicles to be tailored to individual patient need and to increase patient compliance, there is a high potential for their increased and broad use as a replacement for conventional forms of therapeutic administration. Development and validation of mechanistic computational models, as we have done here, lends significant insight into the underlying physical and chemical processes that determine drug release dynamics. Furthermore, by incorporating mechanistic detail, these models are able to be applied to a variety of release vehicle formats, from 10 μm microspheres formed *in vitro*, to 5mm *in situ* forming implants with a variety of molecular weights. This will allow researcher and developers to rapidly screen for conditions (i.e. implant size, polymer molecular weight, polymer ester bond content, drug pH) that produce desired drug release profiles. Thus, we expect this newly developed tool to assist in an acceleration of the iterative design process for producing controlled release vehicles. Immediate future work will be aimed at reducing the model error by collecting experimental data for the diffusion of a variety of drugs in polymers of various molecular weight to further characterize this complex relationship. Another future goal will be to increase the complexity of the solidification model to accurately simulate the phase inversion stage so that prior knowledge of the implant geometry and initial drug distribution are not required by the model.

3.7 Acknowledgments

This work was supported in part by the National Institutes of Health (NIH) National Cancer Institute (NCI) R00CA198929 and National Institute of Drug Abuse (NIDA) R21DA048074 to LS, the National Institute of Biomedical Imaging and Bioengineering (NIBIB) R03EB026231 to JVR, the National Science Foundation (NSF) CAREER award 1752366 to TKU, and the Purdue Discovery Park Undergraduate Internship Program (DURI) to PAG. The content is solely the responsibility of the authors and does not necessarily represent the official views of the NIH or NSF.

3.8 References

[1] A. Luga and M. McGuire, "Adherence and health care costs," *Risk Management and Healthcare Policy*, vol. 7, pp. 35-44, 2014, doi: https://dx.doi.org/10.2147%2FRMHP.S19801.

[2] A. B. Neiman *et al.*, "CDC Grand Rounds: Improving Medication Adherence for Chronic Disease Management - Innovations and Opportunities," *MMWR Morb Mortal Wkly Rep*, vol. 66, no. 45, pp. 1248-1251, 2017, doi: 10.15585/mmwr.mm6645a2.

[3] L. R. Martin, S. L. Williams, K. B. Haskard, and M. R. Dimatteo, "The challenge of patient adherence," (in English), *Therapeutics and clinical risk management*, vol. 1, no. 3, pp. 189-99, 2005 2005.

[4] T. Junaid, X. Wu, H. Thanukrishnan, and Venkataramanan, *Chapter 30 - Therapeutic Drug Monitoring*, D. Thomas, ed., 2019, pp. 425-436.

[5] D. M. Roberts, J. Sevastos, J. E. Carland, S. L. Stocker, and T. N. Lea-Henry, "Clinical Pharmacokinetics in Kidney Disease: Application to Rational Design of Dosing Regimens," (in English), *Clinical journal of the American Society of Nephrology : CJASN*, ; Research Support, Non-U.S. Gov't; Review vol. 13, no. 8, pp. 1254-1263, 2018 08 07 (Epub 2018 Jul 2018, doi: 10.2215/cjn.05150418.

[6] D. N. Kapoor, O. P. Katare, and S. Dhawan, "In situ forming implant for controlled delivery of an anti-HIV fusion inhibitor," (in English), *International journal of pharmaceutics*, ; Research Support, Non-U.S. Gov't vol. 426, no. 1-2, pp. 132-143, 2012 Apr 15 (Epub 2012 Jan 2012, doi: 10.1016/j.ijpharm.2012.01.005.

[7] H. B. Ravivarapu, K. L. Moyer, and R. L. Dunn, "Sustained suppression of pituitary-gonadal axis with an injectable, in situ forming implant of leuprolide acetate," (in English), *Journal of pharmaceutical sciences,* vol. 89, no. 6, pp. 732-41, 2000 2000, doi: 10.1002/(sici)1520-6017(200006)89:6<732::aid-jps4>3.0.co;2-d.

[8] H. B. Ravivarapu, K. L. Moyer, and R. L. Dunn, "Sustained activity and release of leuprolide acetate from an in situ forming polymeric implant," (in English), *AAPS PharmSciTech,* vol. 1, no. 1, p. E1, 2000 Feb 2000, doi: 10.1208/pt010101.

[9] G. L. Southard, R. L. Dunn, and S. Garrett, "The drug delivery and biomaterial attributes of the ATRIGEL technology in the treatment of periodontal disease," (in English), *Expert opinion on investigational drugs,* vol. 7, no. 9, pp. 1483-91, 1998 1998, doi: 10.1517/13543784.7.9.1483.

[10] A. L. Lewis *et al.,* "DC bead: in vitro characterization of a drug-delivery device for transarterial chemoembolization," (in English), *Journal of vascular and interventional radiology : JVIR,* ; Research Support, Non-U.S. Gov't vol. 17, no. 2 Pt 1, pp. 335-42, 2006 2006.

[11] S. R. Benhabbour *et al.,* "Ultra-long-acting tunable biodegradable and removable controlled release implants for drug delivery," (in English), *Nature communications,* ; Research Support, N.I.H., Extramural vol. 10, no. 1, p. 4324, 2019 09 2019, doi: 10.1038/s41467-019-12141-5.

[12] X. S. Wu and N. Wang, "Synthesis, characterization, biodegradation, and drug delivery application of biodegradable lactic/glycolic acid polymers. Part II: biodegradation," (in English), *Journal of biomaterials science. Polymer edition,* vol. 12, no. 1, pp. 21-34, 2001 2001, doi: 10.1163/156856201744425.

[13] S. Hariharan, V. Bhardwaj, I. Bala, J. Sitterberg, U. Bakowsky, and M. N. V. Ravi Kumar, "Design of estradiol loaded PLGA nanoparticulate formulations: a potential oral delivery system for hormone therapy," (in English), *Pharmaceutical research,* ; Research Support, Non-U.S. Gov't vol. 23, no. 1, pp. 184-95, 2006 Jan (Epub 2006 Nov 2006, doi: 10.1007/s11095-005-8418-y.

[14] Y. Yamaguchi, M. Takenaga, A. Kitagawa, Y. Ogawa, Y. Mizushima, and R. Igarashi, "Insulin-loaded biodegradable PLGA microcapsules: initial burst release controlled by hydrophilic additives," (in English), *Journal of controlled release : official journal of the Controlled Release Society,* vol. 81, no. 3, pp. 235-49, 2002 Jun 2002, doi: 10.1016/s0168-3659(02)00060-3.

[15] C.-C. Huang *et al.*, "An Implantable Depot That Can Generate Oxygen in Situ for Overcoming Hypoxia-Induced Resistance to Anticancer Drugs in Chemotherapy," (in English), *Journal of the American Chemical Society,* ; Research Support, Non-U.S. Gov't vol. 138, no. 16, pp. 5222-5, 2016 04 27 (Epub 2016 Apr 2016, doi: 10.1021/jacs.6b01784.

[16] C. Raman, C. Berkland, K. Kim, and D. W. Pack, "Modeling small-molecule release from PLG microspheres: effects of polymer degradation and nonuniform drug distribution," (in English), *Journal of controlled release : official journal of the Controlled Release Society,* ; Research Support, N.I.H., Extramural; Research Support, U.S. Gov't, Non-P.H.S.; Research Support, U.S. Gov't, P.H.S. vol. 103, no. 1, pp. 149-58, 2005 Mar 2005, doi: 10.1016/j.jconrel.2004.11.012.

[17] C. Berkland, K. Kim, and D. W. Pack, "Fabrication of PLG microspheres with precisely controlled and monodisperse size distributions," (in English), *Journal of controlled release : official journal of the Controlled Release Society,* ; Research Support, Non-U.S. Gov't vol. 73, no. 1, pp. 59-74, 2001 May 2001, doi: 10.1016/s0168-3659(01)00289-9.

[18] H. K. Makadia and S. J. Siegel, "Poly Lactic-co-Glycolic Acid (PLGA) as Biodegradable Controlled Drug Delivery Carrier," (in English), *Polymers,* vol. 3, no. 3, pp. 1377-1397, 2011 Sep 01 (Epub 2011 Aug 2011.

[19] M. Parent, C. Nouvel, M. Koerber, A. Sapin, P. Maincent, and A. Boudier, "PLGA in situ implants formed by phase inversion: critical physicochemical parameters to modulate drug release," (in English), *Journal of controlled release : official journal of the Controlled Release Society,* ; Research Support, Non-U.S. Gov't; Review vol. 172, no. 1, pp. 292-304, 2013 Nov 28 (Epub 2013 Sep 2013, doi: 10.1016/j.jconrel.2013.08.024.

[20] P. J. Flory, *Principles of polymer chemistry*. Ithaca: Cornell University Press, 1953.

[21] K. A. Hopkins *et al.*, "Noninvasive characterization of in situ forming implant diffusivity using diffusion-weighted MRI," (in English), *Journal of controlled release : official journal of the Controlled Release Society,* ; Research Support, N.I.H., Extramural vol. 309, pp. 289-301, 2019 09 10 (Epub 2019 Jul 2019, doi: 10.1016/j.jconrel.2019.07.019.

[22] J. C. Helton and F. J. Davis, "Illustration of Sampling-Based Methods for Uncertainty and Sensitivity Analysis," *Risk Anal,* vol. 22, no. 3, pp. 591-622, 2002, doi: 10.1111/0272-4332.00041.

[23] R. L. Iman and J. C. Helton, "An Investigation of Uncertainty and Sensitivity Analysis Techniques for Computer Models," *Risk analysis,* vol. 8, no. 1, pp. 71-90, 1988, doi: 10.1111/j.1539-6924.1988.tb01155.x.

[24] T. L. Kinzer-Ursem and J. J. Linderman, "Both ligand- and cell-specific parameters control ligand agonism in a kinetic model of g protein-coupled receptor signaling," *PLoS Comput Biol,* vol. 3, no. 1, pp. e6-e6, 2007, doi: 10.1371/journal.pcbi.0030006.

[25] D. R. Romano, M. C. Pharris, N. M. Patel, and T. L. Kinzer-Ursem, "Competitive tuning: Competition's role in setting the frequency-dependence of Ca2+-dependent proteins," *PLoS Comput Biol,* vol. 13, no. 11, pp. e1005820-e1005820, 2017, doi: 10.1371/journal.pcbi.1005820.

[26] L. Solorio *et al.*, "Noninvasive characterization of the effect of varying PLGA molecular weight blends on in situ forming implant behavior using ultrasound imaging," (in English), *Theranostics,* ; Research Support, N.I.H., Extramural vol. 2, no. 11, pp. 1064-77, 2012 (Epub 2012 Nov 2012, doi: 10.7150/thno.4181.

[27] J. Kang and S. P. Schwendeman, "Pore closing and opening in biodegradable polymers and their effect on the controlled release of proteins," (in English), *Molecular pharmaceutics,* ; Research Support, N.I.H., Extramural vol. 4, no. 1, pp. 104-18, 2007 2007.

[28] R. B. Patel, A. N. Carlson, L. Solorio, and A. A. Exner, "Characterization of formulation parameters affecting low molecular weight drug release from in situ forming drug delivery systems," (in English), *Journal of biomedical materials research. Part A,* ; Research Support, N.I.H., Extramural vol. 94, no. 2, pp. 476-84, 2010 2010, doi: 10.1002/jbm.a.32724.

[29] J. Stefan, "Über das Gleichgewicht und die Bewegung, insbesondere die Diffusion von Gasgemengen," *Universitätsbibliothek Johann Christian Senckenberg*, pp. 63-124, 1871, doi: http://nbn-resolving.de/urn/resolver.pl?urn:nbn:de:hebis:30-1038910.

[30] M. J, "On the dynamic theory of gases," *Philosophical Transactions of the Royal Society of London* vol. 157, pp. 49-88, 1867, doi: https://doi.org/10.1142/9781848161337_0014.

[31] L. Boudin, B. Grec, and F. Salvarani, "A mathematical and numerical analysis of the Maxwell-Stefan diffusion equations," *Discrete and continuous dynamical systems. Series B*, vol. 17, no. 5, pp. 1427-1440, 2012, doi: 10.3934/dcdsb.2012.17.1427.

[32] F. Fornasiero, J. M. Prausnitz, and C. J. Radke, "Multicomponent Diffusion in Highly Asymmetric Systems. An Extended Maxwell−Stefan Model for Starkly Different-Sized, Segment-Accessible Chain Molecules," *Macromolecules*, vol. 38, no. 4, pp. 1364-1370, 2005, doi: 10.1021/ma040133v.

[33] K. Lu, "The Application of Generalised Maxwell-Stefan Equations to Protein Gels," ed: University of Canterbury. Chemical and Process Engineering, 2007.

[34] R. Krishna and J. A. Wesselingh, "The Maxwell-Stefan approach to mass transfer," *Chemical engineering science*, vol. 52, no. 6, pp. 861-911, 1997, doi: 10.1016/s0009-2509(96)00458-7.

[35] J. S. Vrentas and C. M. Vrentas, "Restrictions on Friction Coefficients for Binary and Ternary Diffusion," *Ind. Eng. Chem. Res*, vol. 46, no. 10, pp. 3422-3428, 2007, doi: 10.1021/ie061593a.

[36] R. J. Bearman, "ON THE MOLECULAR BASIS OF SOME CURRENT THEORIES OF DIFFUSION1," *J. Phys. Chem*, vol. 65, no. 11, pp. 1961-1968, 1961, doi: 10.1021/j100828a012.

[37] K. J. Brodbeck, J. R. DesNoyer, and A. J. McHugh, "Phase inversion dynamics of PLGA solutions related to drug delivery: Part II. The role of solution thermodynamics and bath-side mass transfer," *J Control Release*, vol. 62, no. 3, pp. 333-344, 1999, doi: 10.1016/S0168-3659(99)00159-5.

[38] R. M. Boom, I. M. Wienk, T. van den Boomgaard, and C. A. Smolders, "Microstructures in phase inversion membranes. Part 2. The role of a polymeric additive," *Journal of membrane science,* vol. 73, no. 2-3, pp. 277-292, 1992, doi: 10.1016/0376-7388(92)80135-7.

[39] C. A. Smolders, A. J. Reuvers, R. M. Boom, and I. M. Wienk, "Microstructures in phase-inversion membranes. Part 1. Formation of macrovoids," *Journal of membrane science,* vol. 73, no. 2-3, pp. 259-275, 1992, doi: 10.1016/0376-7388(92)80134-6.

[40] H. Kranz and R. Bodmeier, "A novel in situ forming drug delivery system for controlled parenteral drug delivery," *Int J Pharm,* vol. 332, no. 1, pp. 107-114, 2007, doi: 10.1016/j.ijpharm.2006.09.033.

[41] G. Jiang, B. C. Thanoo, and P. P. DeLuca, "Effect of Osmotic Pressure in the Solvent Extraction Phase on BSA Release Profile from PLGA Microspheres," *Pharm Dev Technol,* vol. 7, no. 4, pp. 391-399, 2002, doi: 10.1081/PDT-120015040.

[42] R. Bodmeier and J. McGinity, "Solvent selection in the preparation of poly(d,l-lactide) microspheres prepared by the solvent evaporation method," *International Journal of Pharmaceutics,* vol. 43, pp. 179-186, 1988, doi: https://doi.org/10.1016/0378-5173(88)90073-7.

[43] S. Ravi, K. K. Peh, Y. Darwis, B. K. Murthy, T. R. R. Singh, and C. Mallikarjun, "Development and characterization of polymeric microspheres for controlled release protein loaded drug delivery system," *Indian J Pharm Sci,* vol. 70, no. 3, pp. 303-309, 2008, doi: 10.4103/0250-474X.42978.

[44] T. A. Ahmed *et al.*, "Development of biodegradable in situ implant and microparticle injectable formulations for sustained delivery of haloperidol," *J Pharm Sci,* vol. 101, no. 10, pp. 3753-3762, 2012, doi: 10.1002/jps.23250.

[45] J. Wang, B. M. Wang, and S. P. Schwendeman, "Characterization of the initial burst release of a model peptide from poly(d,l-lactide-co-glycolide) microspheres," *J Control Release,* vol. 82, no. 2-3, pp. 289-307, 2002, doi: 10.1016/s0168-3659(02)00137-2.

[46] L. solorio, D. Sundarapandiyan, A. Olear, and A. A. Exner, "The Effect of Additives on the Behavior of Phase Sensitive In Situ Forming Implants," *J Pharm Sci,* vol. 104, no. 10, pp. 3471-3480, 2015, doi: 10.1002/jps.24558.

[47] P. D. Graham, K. J. Brodbeck, and A. J. McHugh, "Phase inversion dynamics of PLGA solutions related to drug delivery," *J Control Release,* vol. 58, no. 2, pp. 233-245, 1999, doi: 10.1016/S0168-3659(98)00158-8.

[48] S. Chen and J. Singh, "Controlled delivery of testosterone from smart polymer solution based systems: In vitro evaluation," *Int J Pharm,* vol. 295, no. 1, pp. 183-190, 2005, doi: 10.1016/j.ijpharm.2005.02.023.

[49] G. L. Siparsky, K. J. Voorhees, and F. Miao, "Hydrolysis of Polylactic Acid (PLA) and Polycaprolactone (PCL) in Aqueous Acetonitrile Solutions: Autocatalysis," *Journal of environmental polymer degradation,* vol. 6, no. 1, pp. 31-41, 1998, doi: 10.1023/A:1022826528673.

[50] J. S. Wiggins, M. K. Hassan, K. A. Mauritz, and R. F. Storey, "Hydrolytic degradation of poly(d, l-lactide) as a function of end group: Carboxylic acid vs. hydroxyl," *Polymer (Guilford),* vol. 47, no. 6, pp. 1960-1969, 2006, doi: 10.1016/j.polymer.2006.01.021.

[51] Y. Wang, J. Pan, X. Han, C. Sinka, and L. Ding, "A phenomenological model for the degradation of biodegradable polymers," *Biomaterials,* vol. 29, no. 23, pp. 3393-3401, 2008, doi: 10.1016/j.biomaterials.2008.04.042.

[52] A. Gleadall, J. Pan, M.-A. Kruft, and M. Kellomäki, "Degradation mechanisms of bioresorbable polyesters. Part 1. Effects of random scission, end scission and autocatalysis," *Acta Biomater,* vol. 10, no. 5, pp. 2223-2232, 2014, doi: 10.1016/j.actbio.2013.12.039.

[53] X. Han and J. Pan, "A model for simultaneous crystallisation and biodegradation of biodegradable polymers," *Biomaterials,* vol. 30, no. 3, pp. 423-430, 2008, doi: 10.1016/j.biomaterials.2008.10.001.

[54] X. Han, "Degradation models for polyesters and their composites," ed: University of Leicester, 2011.

[55] K. Sevim and J. Pan, "A Mechanistic Model for Acidic Drug Release Using Microspheres Made of PLGA 50:50," *Mol. Pharmaceutics,* vol. 13, no. 8, pp. 2729-2735, 2016, doi: 10.1021/acs.molpharmaceut.6b00313.

[56] N. Faisant, J. Siepmann, and J. P. Benoit, "PLGA-based microparticles: elucidation of mechanisms and a new, simple mathematical model quantifying drug release," (in English), *European journal of pharmaceutical sciences : official journal of the European Federation for Pharmaceutical Sciences,* ; Research Support, Non-U.S. Gov't vol. 15, no. 4, pp. 355-66, 2002 2002, doi: 10.1016/s0928-0987(02)00023-4.

[57] C. Shih, "A graphical method for the determination of the mode of hydrolysis of biodegradable polymers," *Pharm Res,* vol. 12, no. 12, pp. 2036-2060, 1995.

[58] A. Belbella, C. Vauthier, H. Fessi, J.-P. Devissaguet, and F. Puisieux, "In vitro degradation of nanospheres from poly(D,L-lactides) of different molecular weights and polydispersities," *International journal of pharmaceutics,* vol. 129, no. 1, pp. 95-102, 1996, doi: 10.1016/0378-5173(95)04258-X.

[59] C. Shih, N. Waldron, and G. M. Zentner, "Quantitative analysis of ester linkages in poly(dl-lactide) and poly(dl-lactide-co-glycolide)," *Journal of controlled release,* vol. 38, no. 1, pp. 69-73, 1996, doi: 10.1016/0168-3659(95)00104-2.

[60] S. H. Hyon, K. Jamshidi, and Y. Ikada, "Effects of residual monomer on the degradation of DL-lactide polymer," *Polymer international,* vol. 46, no. 3, pp. 196-202, 1998, doi: 10.1002/(SICI)1097-0126(199807)46:3<196::AID-PI914>3.0.CO;2-Y.

[61] C. Shih, "Calculation of hydrolytic rate constants of poly(ortho ester)s from molecular weights determined by gel permeation chromatography," *Pharm Res,* vol. 12, no. 12, pp. 2041-2048, 1995.

[62] H. Tsuji and K. Ikarashi, "In vitro hydrolysis of poly(l-lactide) crystalline residues as extended-chain crystallites. Part I: long-term hydrolysis in phosphate-buffered solution at 37°C," *Biomaterials,* vol. 25, no. 24, pp. 5449-5455, 2004, doi: 10.1016/j.biomaterials.2003.12.053.

[63] M. Inokuti, "Weight-Average and z-Average Degree of Polymerization for Polymers Undergoing Random Scission," *The Journal of chemical physics,* vol. 38, no. 5, pp. 1174-1178, 1963, doi: 10.1063/1.1733820.

[64] X. Han, J. Pan, F. Buchanan, N. Weir, and D. Farrar, "Analysis of degradation data of poly(l-lactide–co- l, d-lactide) and poly(l-lactide) obtained at elevated and physiological temperatures using mathematical models," *Acta Biomater,* vol. 6, no. 10, pp. 3882-3889, 2010, doi: 10.1016/j.actbio.2010.05.015.

[65] H. Fujita, "Diffusion in polymer-diluent systems," *In: Fortschritte Der Hochpolymeren-Forschung. Advances in Polymer Science,* vol. 3, 1961, doi: https://link.springer.com/chapter/10.1007/BFb0050514.

[66] H. Fujita, "Notes on free volume theories," *Polymer Journal,* vol. 23, no. 12, pp. 1499-1506, 1991, doi: https://doi.org/10.1295/polymj.23.1499.

[67] S. JU, H. Liu, J. Duda, and J. Vrentas, "Solvent diffusion in amorphous polymers," *Journal of Applied Polymer Sciences,* vol. 26, pp. 3735-3744, 1981, doi: https://doi.org/10.1002/app.1981.070261120.

[68] K. Zieminshi and N. Peppas, "Diluent diffusion in polymer-diluent systems near Tg: Migration of phthalic esters from PVC to water," *Journal of Applied Polymer Science,* vol. 28, pp. 1751-1765, 1983, doi: https://doi.org/10.1002/app.1983.070280518.

[69] R. Korsmeyer, R. Gurny, E. Doelker, P. Buri, and N. Peppas, "Mechanisms of solute release from porous hydrophilic polymers," *International Journal of Pharmaceutics,* vol. 15, pp. 25-35, 1983, doi: https://doi.org/10.1016/0378-5173(83)90064-9.

[70] L. Peppas and N. Peppas, "Solute and penetrant diffusion in swellable polymers. IX. The mechanisms of drug release from pH-sensitive swelling-controlled systems," *Journal of Controlled Release,* vol. 8, pp. 267-274, 1989, doi: https://doi.org/10.1016/0168-3659(89)90048-5.

[71] B. Narasimhan and N. A. Peppas, "Molecular analysis of drug delivery systems controlled by dissolution of the polymer carrier," (in English), *Journal of pharmaceutical sciences,* ; Research Support, U.S. Gov't, Non-P.H.S. vol. 86, no. 3, pp. 297-304, 1997 1997, doi: 10.1021/js960372z.

[72] J. Siepmann, K. Podual, M. Sriwongjanya, N. A. Peppas, and R. Bodmeier, "A new model describing the swelling and drug release kinetics from hydroxypropyl methylcellulose tablets," (in English), *Journal of pharmaceutical sciences,* ; Research Support, Non-U.S. Gov't; Research Support, U.S. Gov't, P.H.S. vol. 88, no. 1, pp. 65-72, 1999 1999, doi: 10.1021/js9802291.

[73] R. W. Korsmeyer, S. R. Lustig, and N. A. Peppas, "Solute and penetrant diffusion in swellable polymers. I. Mathematical modeling," *Journal of polymer science. Part B, Polymer physics,* vol. 24, no. 2, pp. 395-408, 1986, doi: 10.1002/polb.1986.090240214.

[74] R. W. Korsmeyer, E. Von Meerwall, and N. A. Peppas, "Solute and penetrant diffusion in swellable polymers. II. Verification of theoretical models," *Journal of polymer science. Part B, Polymer physics,* vol. 24, no. 2, pp. 409-434, 1986, doi: 10.1002/polb.1986.090240215.

[75] M. Zhang, Z. Yang, L.-L. Chow, and C.-H. Wang, "Simulation of drug release from biodegradable polymeric microspheres with bulk and surface erosions," (in English), *Journal of pharmaceutical sciences,* ; Research Support, Non-U.S. Gov't vol. 92, no. 10, pp. 2040-56, 2003 2003, doi: 10.1002/jps.10463.

[76] M. Hill, R. N. Cunningham, R. M. Hathout, C. Johnston, J. G. Hardy, and M. E. Migaud, "Formulation of Antimicrobial Tobramycin Loaded PLGA Nanoparticles via Complexation with AOT," (in English), *Journal of functional biomaterials,* vol. 10, no. 2, 2019 Jun 2019, doi: 10.3390/jfb10020026.

[77] M. C. Operti, Y. Dolen, J. Keulen, E. A. W. van Dinther, C. G. Figdor, and O. Tagit, "Microfluidics-Assisted Size Tuning and Biological Evaluation of PLGA Particles," (in English), *Pharmaceutics,* vol. 11, no. 11, 2019 Nov 2019, doi: 10.3390/pharmaceutics11110590.

[78] C. Jiang *et al.*, "Biodegradable Polymeric Microsphere-Based Drug Delivery for Inductive Browning of Fat," (in English), *Frontiers in endocrinology,* vol. 6, p. 169, 2015 2015, doi: 10.3389/fendo.2015.00169.

[79] A. C. Doty *et al.*, "Mechanisms of in vivo release of triamcinolone acetonide from PLGA microspheres," (in English), *Journal of controlled release : official journal of the Controlled Release Society,* ; Research Support, Non-U.S. Gov't vol. 256, pp. 19-25, 2017 06 28 (Epub 2017 Mar 2017, doi: 10.1016/j.jconrel.2017.03.031.

[80] J. Kang and S. P. Schwendeman, "Determination of Diffusion Coefficient of a Small Hydrophobic Probe in Poly(lactide-c o-glycolide) Microparticles by Laser Scanning Confocal Microscopy," *Macromolecules,* vol. 36, no. 4, pp. 1324-1330, 2003, doi: 10.1021/ma021036+.

[81] M. Alkholief *et al.*, "Employing a PLGA-TPGS based nanoparticle to improve the ocular delivery of Acyclovir," (in English), *Saudi pharmaceutical journal : SPJ : the official publication of the Saudi Pharmaceutical Society,* vol. 27, no. 2, pp. 293-302, 2019 Feb (Epub 2018 Nov 2019, doi: 10.1016/j.jsps.2018.11.011.

[82] G. Arora, J. Shukla, S. Ghosh, S. K. Maulik, A. Malhotra, and G. Bandopadhyaya, "PLGA nanoparticles for peptide receptor radionuclide therapy of neuroendocrine tumors: a novel approach towards reduction of renal radiation dose," (in English), *PloS one,* ; Research Support, Non-U.S. Gov't vol. 7, no. 3, p. e34019, 2012 (Epub 2012 Mar 2012, doi: 10.1371/journal.pone.0034019.

[83] H. Pool *et al.*, "Antioxidant Effects of Quercetin and Catechin Encapsulated into PLGA Nanoparticles," *Journal of nanomaterials,* vol. 2012, pp. 1-12, 2012, doi: 10.1155/2012/145380.

[84] A. A. Öztürk, E. Yenilmez, and M. G. Özarda, "Clarithromycin-Loaded Poly (Lactic-co-glycolic Acid) (PLGA) Nanoparticles for Oral Administration: Effect of Polymer Molecular Weight and Surface Modification with Chitosan on Formulation, Nanoparticle Characterization and Antibacterial Effects," *Polymers,* vol. 11, no. 10, p. 1632, 2019, doi: 10.3390/polym11101632.

[85] A. Gaignaux *et al.*, "Development and evaluation of sustained-release clonidine-loaded PLGA microparticles," *Int J Pharm,* vol. 437, no. 1-2, pp. 20-28, 2012, doi: 10.1016/j.ijpharm.2012.08.006.

[86] S.-B. Sun, P. Liu, F.-M. Shao, and Q.-L. Miao, "Formulation and evaluation of PLGA nanoparticles loaded capecitabine for prostate cancer," (in English), *International journal of clinical and experimental medicine,* vol. 8, no. 10, pp. 19670-81, 2015 2015.

[87] I. Mylonaki, E. Allemann, F. Delie, and O. Jordan, "Imaging the porous structure in the core of degrading PLGA microparticles: The effect of molecular weight," (in English), *Journal of controlled release : official journal of the Controlled Release Society,* vol. 286, pp. 231-239, 2018 09 28 (Epub 2018 Jul 2018, doi: 10.1016/j.jconrel.2018.07.044.

[88] Y. Liu, "Mapping microclimate pH in biodegradable polymeric microspheres," ed.

[89] M. D. Milne, "Influence of Acid-Base Balance on Efficacy and Toxicity of Drugs," *Journal of the Royal Society of Medicine,* vol. 58, no. 11P2, pp. 961-963, 1965, doi: 10.1177/003591576505811P204.

[90] J. W. Wojtkowiak, D. Verduzco, K. J. Schramm, and R. J. Gillies, "Drug Resistance and Cellular Adaptation to Tumor Acidic pH Microenvironment," *Mol. Pharmaceutics,* vol. 8, no. 6, pp. 2032-2038, 2011, doi: 10.1021/mp200292c.

[91] W. Men *et al.*, "Layer-by-layer pH-sensitive nanoparticles for drug delivery and controlled release with improved therapeutic efficacy in vivo," *Drug Deliv,* vol. 27, no. 1, pp. 180-190, 2020, doi: 10.1080/10717544.2019.1709922.

[92] S. Marino, I. B. Hogue, C. J. Ray, and D. E. Kirschner, "A methodology for performing global uncertainty and sensitivity analysis in systems biology," *J Theor Biol,* vol. 254, no. 1, pp. 178-196, 2008, doi: 10.1016/j.jtbi.2008.04.011.

[93] A. Saltelli, P. Annoni, I. Azzini, F. Campolongo, M. Ratto, and S. Tarantola, "Variance based sensitivity analysis of model output. Design and estimator for the total sensitivity index," *Computer physics communications,* vol. 181, no. 2, pp. 259-270, 2010, doi: 10.1016/j.cpc.2009.09.018.

3.9 Appendix

Appendix A. FRAP Data

Table S1. FRAP Data. FRAP data collected for two samples: sample 1 was the diffusion of fluorescein in water, and sample 2 is the diffusion of fluorescein in dissolved polymer (53 kDa).

	Sample 1t-half [s]	**Diffusion [μm^2/s]**	**Sample 2 t-half [s]**	**Diffusion [μm^2/s]**
Run 1			4.5576	17.22358294
Run 2	1.665	47.14606703	4.8886	16.05739917
Run 3	2.0206	38.84895655	5.1843	15.14152375
Run 4	1.3447	58.37599584	4.9417	15.88485776
Run 5	1.6417	47.81519254	4.9130	15.97765146
Average		48.04655299		16.05700302

Appendix B. DWI Data

To properly model the degradation of the polymer, we chose to model the diffusion of the polymer oligomers and hydronium produced from the dissociation of hydrogen ions from the carboxylic acid end groups, separately. The MR data gave us both spatial and temporal resolution of the diffusivity of the implant to water as the polymer solidifies. Great care was taken to ensure that the organic solvent did not influence the data, Figure 1. We used these values for the diffusivity of the implant to water and hydronium.

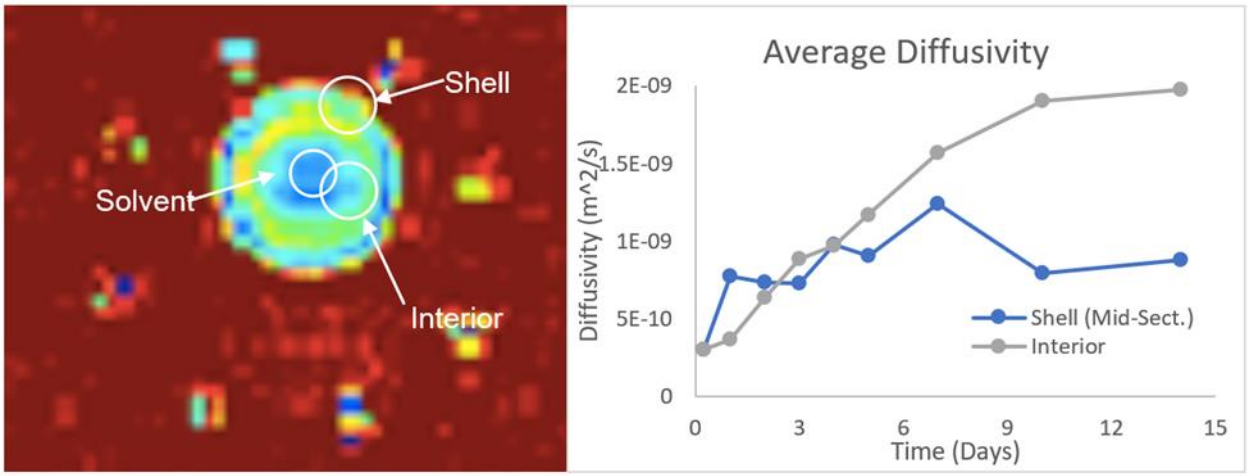

Fig S1. Analyzing DWI Data. (Left) DWI data for the 53 kDa ISFI, 2 days post-exposure. The diffusivity of water is not only influenced by the precipitation of the polymer, but also by the presence of organic solvent. (Right) The average diffusivity of the implant's shell and interior over 14 days.

To ensure that the added computational cost was necessary the model was run twice with all the same parameters except the diffusion of the hydronium was solved for using the diffusivity of the oligomers. The result was a huge increase in the degradation phase of the drug release profile, Figure 2.

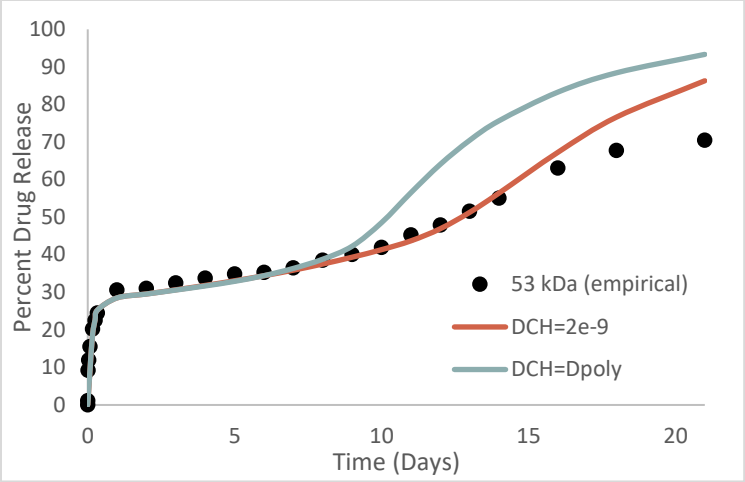

Fig S2. Impact of modeling diffusion of acid. Drug release profile when using the MR data (blue) or the oligomer (grey) diffusivity for the diffusivity of the hydrogen ions as compared to the empirical data for the 53 kDa implant.

To properly determine the degradation rates it is necessary to model the ions and oligomers as having separate diffusivities.

Appendix C. LHS/PRCC Results

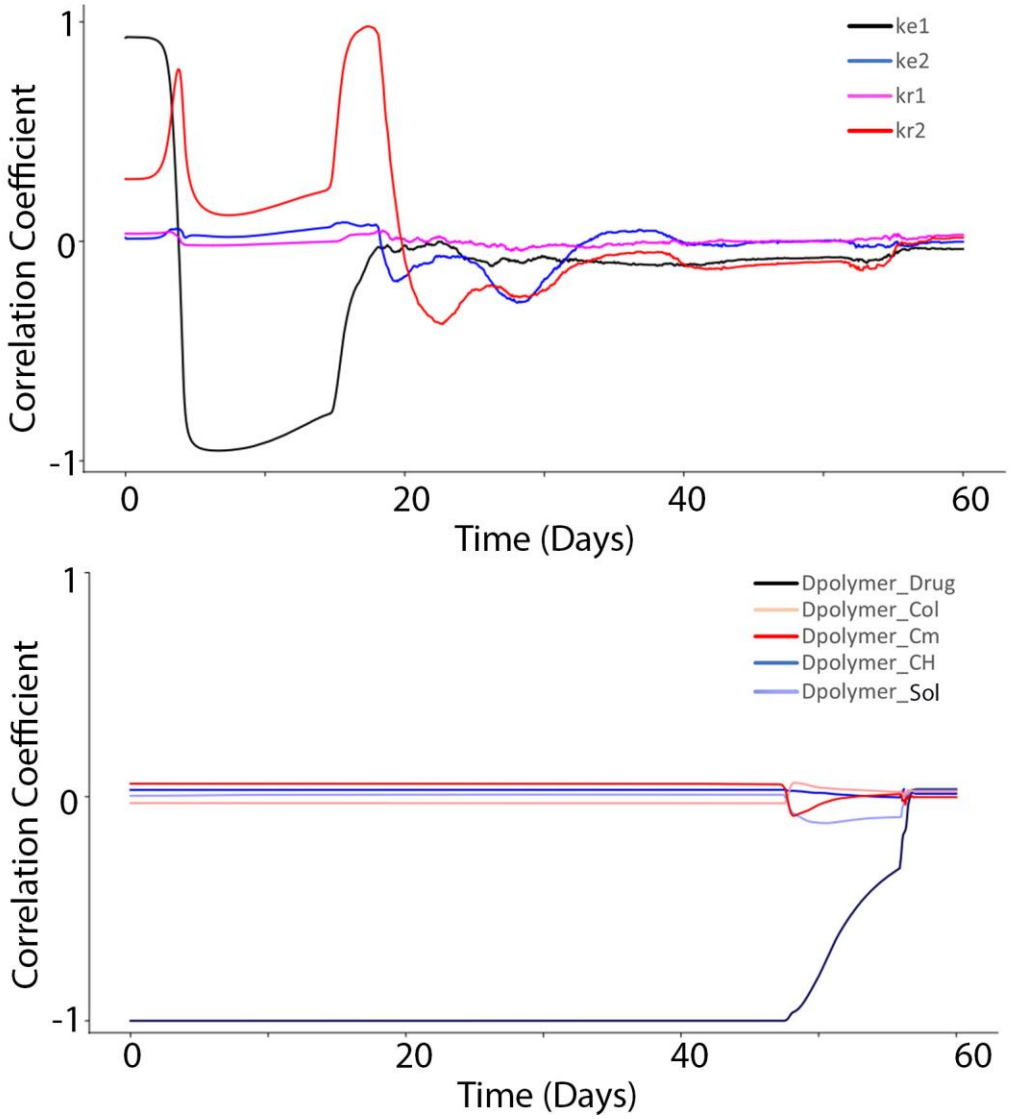

Fig S3. LHS/PRCC for degradation rates. (Top) Global sensitivity analysis for the 10 µm microspheres, investigating the impact of degradation rates on the drug release profile. (Bottom) Global sensitivity analysis for the 10 µm microspheres, investigating the impact of diffusion coefficients on the drug release profile.

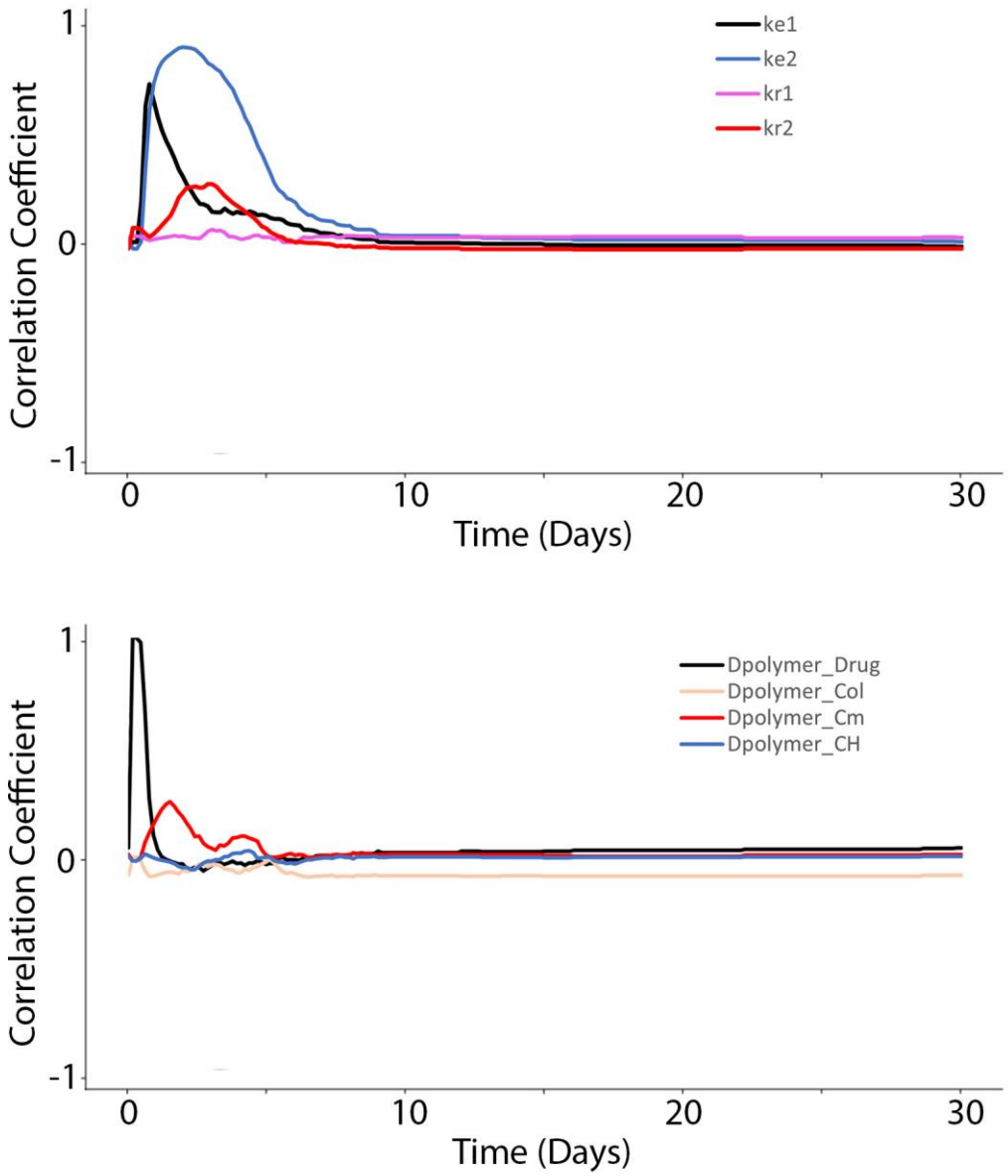

Fig S4. LHS/PRCC for degradation rates. (Top) Global sensitivity analysis for the 53 kDa ISFI, investigating the impact of degradation rates on the drug release profile. (Bottom) Global sensitivity analysis for the 53 kDa ISFI, investigating the impact of diffusion coefficients on the drug release profile.

Appendix D. Impact of Autocatalytic Degradation

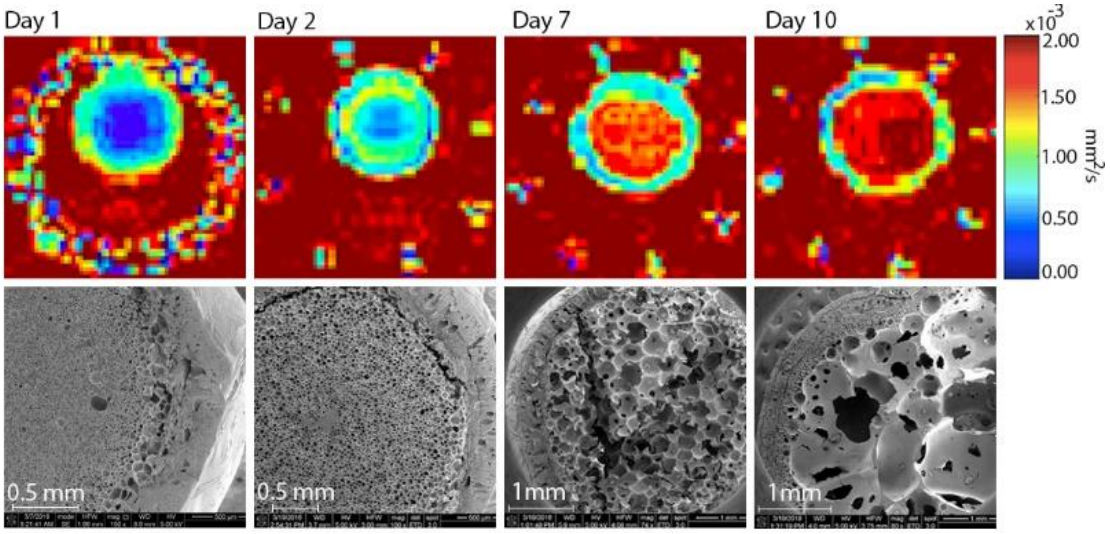

Fig S5. Interior degradation. DWI (top) and SEM (bottom) data for a 53 kDa 5mm ISFI corroborating extensive interior degradation and enlargement of the interior pore size, while the shell of the implant remains intact up to 10 days.

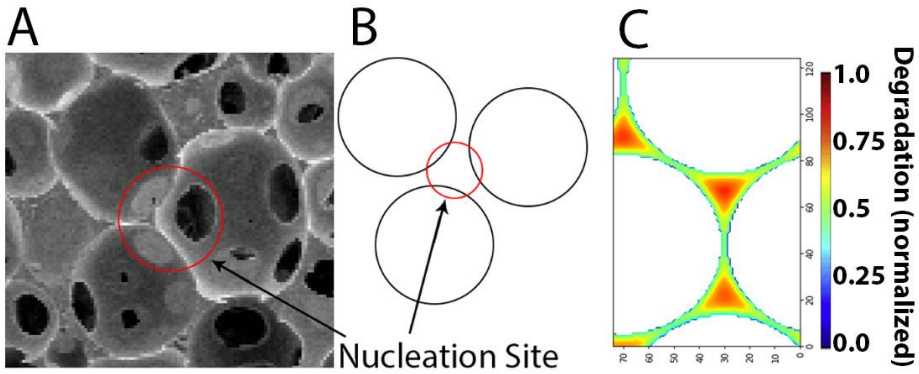

Fig S6. Interior pore degradation. A) SEM images taken from 5 days after formation show accelerated degradation between pores. B) Depiction of the nucleation site. C) Magnified 2D model show quicker degradation where the polymer is the thickest.

Appendix E. Model Error

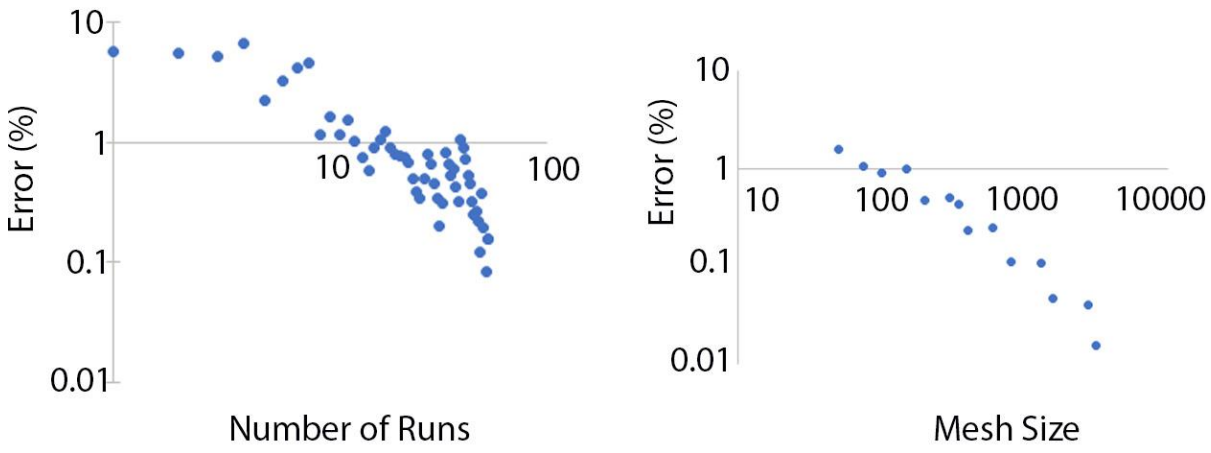

Fig S7. Numerical Error. (left) Error introduced by stochastic variations of the pores in the 50 µm implants. (right) Error introduced by reducing mesh size.

Table S2. Error in Encapsulation Efficiency. Error in predicting encapsulation efficiencies for 10 and 50 µm microspheres.

10 µm	**Experimental**	**Model**	**Error**	**50 µm**	**Experimental**	**Model**	**Error**
6.5 KDA	0.436	0.47	3.4	**6.5 kDa**	na	na	
21 KDA	0.484	0.585	10.1	**21 kDa**	0.507	0.449	5.8
34 KDA	0.595	0.853	25.8	**34 kDa**	0.609	0.449	16
49 KDA	0.558	0.82	26.2	**49 kDa**	0.592	0.795	20.3
67 KDA	0.66	0.898	23.8	**67 kDa**	0.638	0.959	32.1
AVERAGE			17.86	**Average**			18.55

Table S3. Error in Predicting Burst of Drug from ISFIs. Error in predicting the burst of drug in the first three days from the 15, 29, and 53 kDa ISFIs.

Time (Days)	**15 kDa**	**29 kDa**	**53 kDa**
0	0	0	0
0.000694	0.618605	0.615609	0.125576
0.020833	1.002027	6.301118	0.210152
0.041667	2.162772	2.712277	1.898253
0.083333	2.997528	2.941846	3.760481

0.166667	4.123892	2.745987	5.329084
0.25	4.867726	3.394127	3.737764
0.333333	5.055775	4.275742	1.902631
1	2.294014	6.690966	4.022396
2	3.572021	4.63953	3.86442
3	6.421459	3.280951	4.653251
Average	3.311582	3.759815	2.950401

Table S4. Error in pH Prediction. Error in predicting the time dependent pH change for a 50 μm microsphere.

pH Error	Experimental	Model	Error
7 Days	4.942	5.308	7.420
14 Days	4.825	4.983	3.282
21 Days	4.717	4.700	0.353
28 Days	4.508	4.342	3.697
Average			3.688

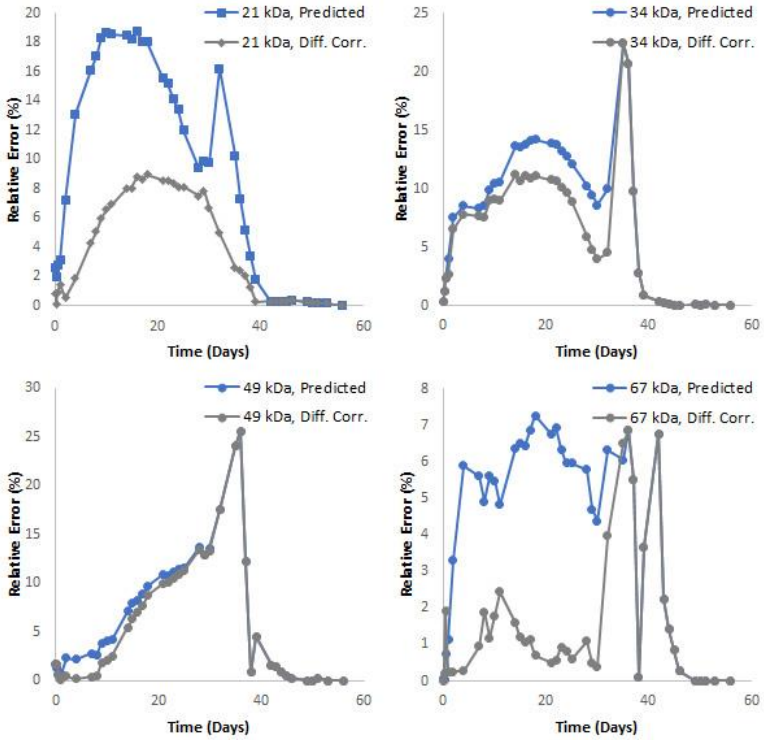

Fig S8. Drug Release Error 50 µm microspheres. Time dependent, absolute error in predicting the drug released from the 50 µm microspheres. Average error for the 21,34,49, and 67 kDa implants is 6.075, 6.239, 0.499, and 2.851%.

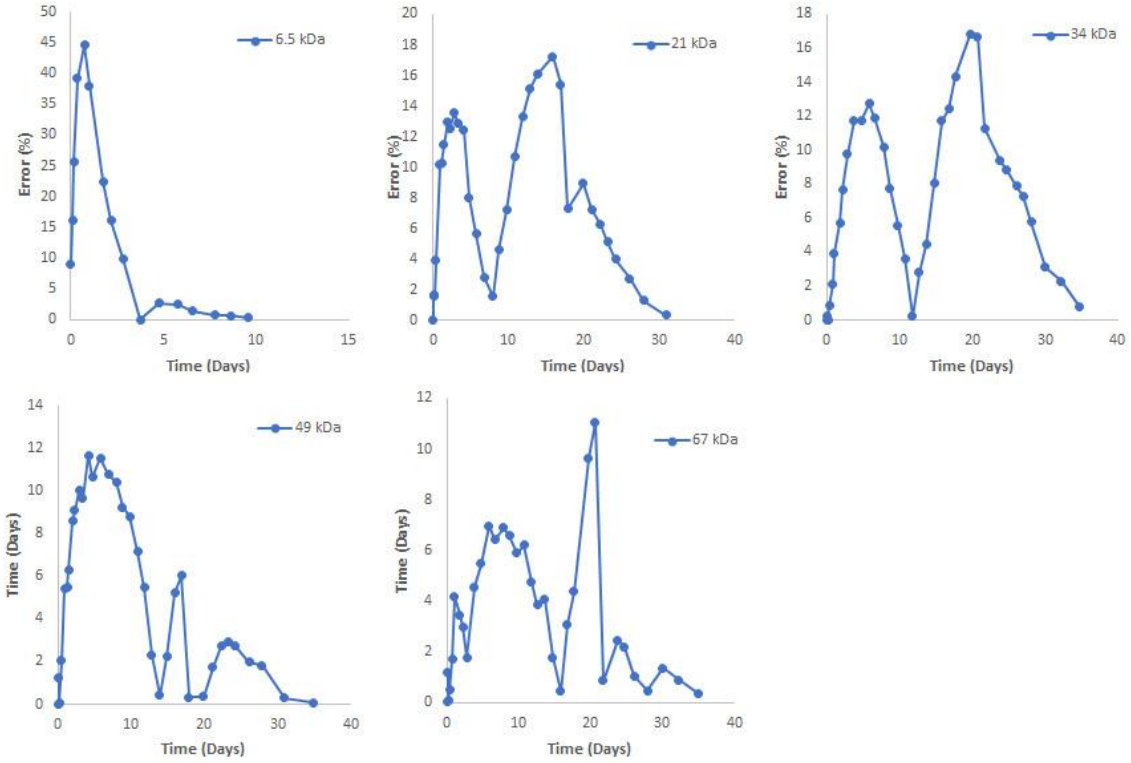

Fig S9. Drug Release Error 10 µm microspheres. Time dependent, absolute error in predicting the drug released from the 10 µm microspheres. Average error for the 6.5, 21,34,49, and 67 kDa implants is 13.902, 5.040, 6.273, 8.734, and 6.064%.

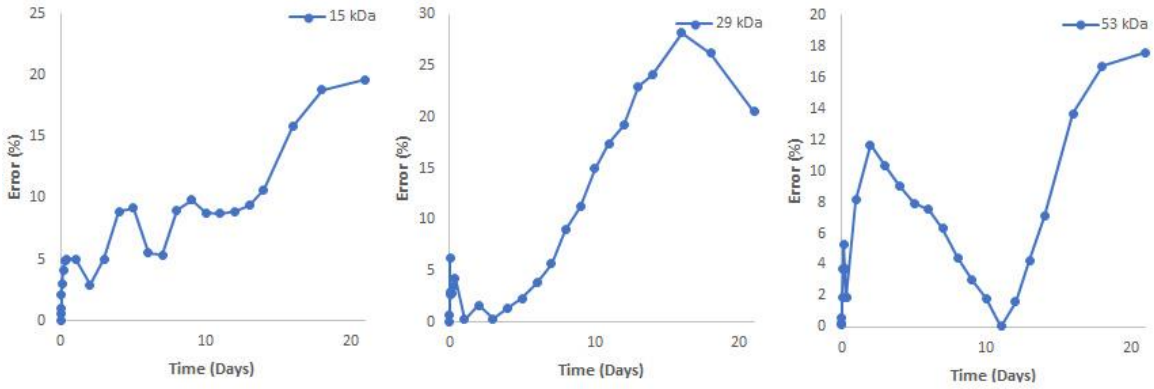

Fig S10 Drug Release Error, 5mm ISFIs. Time dependent, absolute error in predicting the drug released from the 5 mm ISFIs. Average error for the 15, 29, and 53 kDa implants is 7.300, 9.295, and 5.961%, respectively.

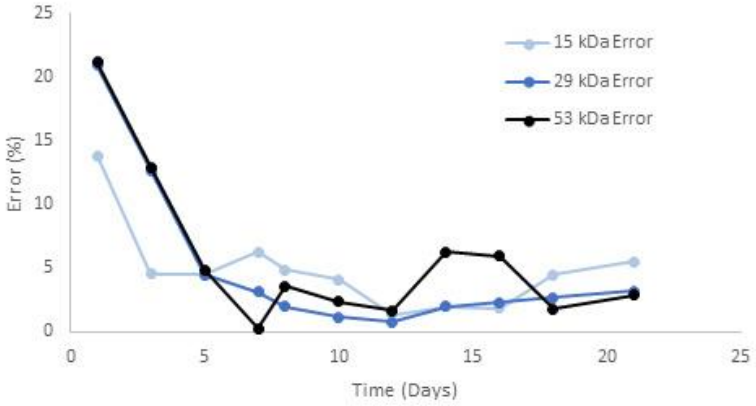

Fig S11 Time Dependent Mass Loss Error for 5mm ISFI. Absolute error in predicting the loss of mass from the 5mm ISFIs over 21 days. Average error for the 15, 29, and 53 kDa implants is 4.778, 5.224, and 6.080%, respectively. Average error after 3 days for the 15, 29, and 53 kDa ISFIs is 3.679, 2.328, and 3.342%, respectively.

Appendix F. Model Parameters Values

Table S5. Model Parameters. Values for all model parameters and values of the optimized parameters shown in figures 7 and 8.

10 µm	**6.5 kDa**		**21 kDa**		**34 kDa**		**49 kDa**		**67 kDa**	
Parameters	pred.	opt.	pred.	opt.	pred.	opt.	pred.	opt.	pred.	opt.
ke1	3.75e-3	-	3.75e-3	-	3.75e-3	-	3.75e-3	-	3.75e-3	-
ke2	2.81e-6	-	2.81e-6	-	2.81e-6	-	2.81e-6	-	2.81e-6	-
kr1	7e-6	-	7e-6	-	7e-6	-	7e-6	-	7e-6	-
kr2	1.12e-2	-	1.12e-2	-	1.12e-2	-	1.12e-2	-	1.12e-2	-
Xc0	0.2511	-	0.2162	-	0.1824	-	0.1254	-	0.1	-
Dpoly_drug xe-18(m^2/s)	12.221	40	3.178	4	1.804	3	1.167	2.5	0.802	1.5
β	na	na	na	na	na	na	na	na	na	na
50 µm			21 kDa		34 kDa		49 kDa		67 kDa	
ke1	na	na	3.75e-3	-	3.75e-3	-	3.75e-3	-	3.75e-3	-
ke2	na	na	2.81e-6	-	2.81e-6	-	2.81e-6	-	2.81e-6	-
kr1	na	na	7e-6	-	7e-6	-	7e-6	-	7e-6	-
kr2	na	na	1.12e-2	-	1.12e-2	-	1.12e-2	-	1.12e-2	-
Xc0	na	na	0.2162	-	0.1824	-	0.1254	-	0.1	-
Dpoly_drug (m^2/s)	na	na	3.178	4	1.804	3	1.167	2.5	0.802	1.5
β	na	na	na	na	na	na	na	na	na	na
ISFI	**15 kDa**		**29 kDa**		**53 kDa**					
ke1	3.75e-3	-	3.75e-3	-	3.75e-3	-				
ke2	2.81e-6	-	2.81e-6	-	2.81e-6	-				
kr1	7e-6	-	7e-6	-	7e-6	-				
kr2	1.12e-2	-	1.12e-2	-	1.12e-2	-				
Xc0	0.1288	-	0.1920	-	0.1288	-				
Dpoly_drug xe-18(m^2/s)	4.575	-	2.212	-	1.034	-				
β	8.4	8.2	8.4	10	8.4	10				

4. UTILIZATION OF DIRECT FORCING IMMERSED BOUNDARY METHODS FOR THE OPTIMIZATION OF INERTIAL FOCUSING MICROFLUIDICS

4.1 Introduction

Inertial focusing microfluidics have gained significant momentum in the last decade for their ability to separate and filter mixtures of particles and cells based on size [1-3]. However, the most important feature is that the separation is passive, without the need for external forces. At the heart of inertial focusing is the balance between counteracting lift forces: shear and wall-induced lift. Shear-induced lift is a product of the curvature of the fluid flow and the rotation of the particle in the flow, while wall-induced lift is generated by the disturbance of the fluid by the particle near a wall. This phenomenon was first observed by Segre and Silberberg for the focusing of particles in a pipe, and was later extended to the focusing of cells and particle in rectangular channels [4]. Taking advantage of inertial focusing we explore particle capture utilizing an expanded channel microfluidics chip design. By expanding a small region of the straight channel microvortices form in the well, which allows for size selective trapping of particles [1, 2].

Modeling the two-way coupled with traditional finite volume method (FVM) or finite element method (FEM) can prove costly as with each time step the body-fitted grid would have to be re-meshed [5, 6]. Immersed boundary methods (IBM) offer a cost effective solution, rather than solving the fluid equations on a body fitted grid they are solved on a regular cartesian grid and the boundary conditions are imposed on the fluid domain by the addition of a forcing term. The Navier-Stokes equations are solved for on this Eulerian grid, while the Newton-Euler equations that govern the motion of the particle are solved for on the Lagrangian grid that defines the surface of the particle. The direct forcing IBM accounts for the force and torque acting on the particle by the requirement of the predict fluid velocity to be the local velocity of the particle on the surface of particle [7, 8]. Interpolations are required to find the velocity of the fluid on the Lagrangian nodes, and then a spreading function to return the force on the Lagrangian nodes back to the Eulerian grid [9].

4.2 Materials and Methods

4.2.1 Experimental Methods

Design and Fabrication of Microfluidics Chips

For this study, two chip designs were produced to evaluate the inertial focusing properties of particles. The first chip design is a straight channel microfluidics chip fabricated in polydimethylsiloxane (PDMS, SYLGARD184 Silicone Elastomer Kit) using a master mold developed with standard photolithography. A silicon wafer with dry resist film (PerMX 3050 series, DuPont Electronic Technologies) was used to develop the mold and cast the PDMS, which was then bound to a glass slide (Sigma Aldrich) and baked for 45 minutes at 95 ̊C. A second series of chip designs were produced with an expanded channel to produce microvortices for particle retention. These microfluidics chips were designed by cutting pressure sensitive adhesive (PSA, ARseal 90880, Adhesive Research, cyclic olefin copolymer (COC, Zeon Zeonor zf14-188) with a laser cutter (Universal Laser Systems, VSL350).

Particle Imaging

Experimental data for the motion of buoyant polystyrene microparticles of size 1 and 7.32 μm in diameter, and acrylic particles of size 20 μm in diameter (Fisher Scientific) were captured using a fluorescence microscope (Axio Observer, Zeiss). Shutter speeds were varied from 1/10 to 1/10000 s, allowing for both particle image velocimetry (PIV) data analysis and the observation of complete pathlines. The 1, 7.32, and 20 μm particles were mixed with deionized water at a concentration of $5x10^7$, $2.5x10^5$, and $6x10^4$ particles per mL, respectively. Particles were collected in a syringe (BD syringe, 1mL) and pumped through PEEK tubing (IDEX, 1569) utilizing a syringe pump (KD Scientific Inc) to vary flow conditions ($0.1 \leq Re \leq 500$).

Image Analysis

The expanded well design produced two separate fluid domains with dramatically different Reynolds numbers (Re), which required separate in-house algorithms for the quantification of particle velocities. For regions of slow fluid motion, particle motion was captured in image pairs that produced a strong cross-correlation, which is ideal for PIV analysis. However, in regions of high Reynolds flow the particles became faint streaks, and cross-correlation procedures became

nonviable. Particle streak velocimetry (PSV) was employed to find and quantify the length of the streaks to determine the particles velocity.

The first few image pairs were used to segment the images into regions of large and small Re flow to be quantified by either PIV or PSV, respectively. The first image pair from the stack was split into interrogation window and evaluated with a FFT cross-correlation algorithm to evaluate the strength of cross-correlation for each window, Fig 1a. Windows that produced cross-correlation resembling a Dirac function were quantified with PIV for the entire image stack. Regions with a cross-correlation domains of lowered and wider peaks in the cross-correlation domain were segmented with a morphological operator to look for streaks, Fig 1b. If streaks were identified of significant size PSV was used to quantify the particle motion in the window for the entire stack. If there were no significant streaks in the window, then the particle velocity of that window was set to zero to avoid extraneous velocity vectors, Fig 1c. This allowed for rapid and accurate quantification of the particle motion in the entire fluid domain within the microfluidics chip, Fig 1d.

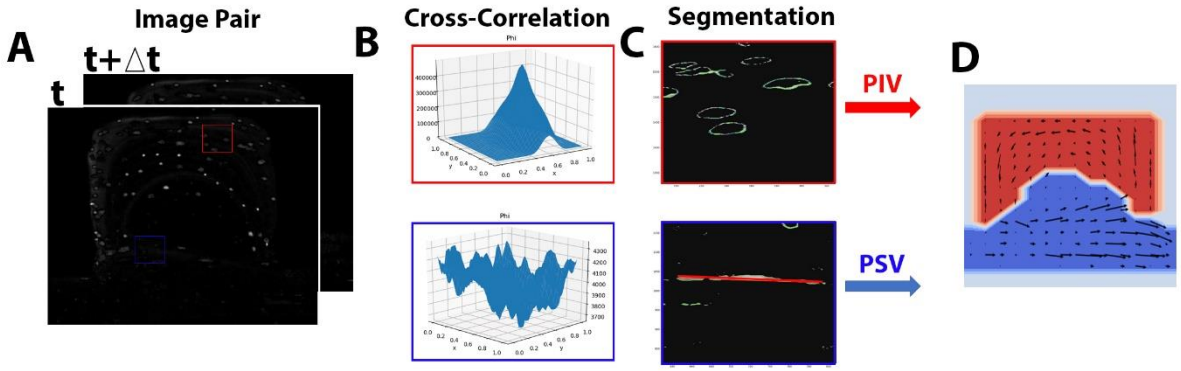

Figure 4.1. PIV/PSV Algorithm. (A) Image pair used to produce mask to separate windows for PIV or PSV analysis. (B) Cross-correlation of a window in the image pair. (C) Segmentation of images to identify streaks. (D) Final quantification of particle velocities in the entire system. Regions quantified with PIV/PSV are red/blue, respectively.

4.2.2 Numerical Methods

Governing Equations

Particle motion was governed by Newton-Euler equations, while the fluid motion was governed by the Navier-Stokes equations.

The incompressible, Newtonian Navier-Stokes equations:

$$\frac{\partial u_i}{\partial t} + \frac{\partial}{\partial x_j} u_i u_j = -\frac{\partial p_i}{\partial x_i} + \frac{1}{Re} \frac{\partial}{\partial x_j} \frac{\partial u_i}{\partial x_j} \quad (1)$$

$$\frac{\partial u_i}{\partial x_i} = 0 \quad (2)$$

where u_i is the i[th] component of the fluid velocity, x_j is the j[th] dimension, and p_i is the i[th] component of pressure. Notable this system was 2D flow and gravity was negligible in this system for small buoyant particles. Re is defined as

$$Re = \frac{\rho_f UL}{\mu} \quad (3)$$

where ρ_f is the density, μ is the dynamic viscosity, U is the characteristic velocity, and L is the characteristic length of the fluid.

The particle was modeled by a string of interconnected nodes, the motion of which includes both translational and rotational velocity:

$$u_{pn} = u_p + \omega_p \, x \, r \quad (4)$$

where u_{pn} is the velocity of the particle node, u_p is the velocity of the particle, ω_p is the angular velocity of the particle, and r is the radial arm from the position of the node to the center of mass of the particle. Assuming buoyancy the Newton-Euler equations became:

$$\rho_p V_p \frac{\partial u_p}{\partial t} = \oint_{\partial V} \tau * n da + F_c \quad (5)$$

$$I_p \frac{\partial \omega_c}{\partial t} = \oint_{\partial V} r \, x \, (\tau * n) da + T_c \quad (6)$$

where ρ_p is the density of the particle V_p is the volume of the particle, F_c is the force introduced by a collision, I_p is the moment of inertia of the particle, T_c is the torque introduced by a collision, and τ is the total stress tensor acting on the particle. Finally, eq 1 is modified to include the forcing term:

$$\frac{\partial u_i}{\partial t} + \frac{\partial}{\partial x_j} u_i u_j = -\frac{\partial p_i}{\partial x_i} + \frac{1}{Re} \frac{\partial}{\partial x_j} \frac{\partial u_i}{\partial x_j} + f_i \quad (7)$$

where the forcing term f is zero everywhere except in the vicinity of the particle.

First Order Accurate Immersed Boundary Method

The Navier-Stokes equations are handled with pressure-correction scheme, which is highly compatible with the direct forcing IBM [5, 10]. The numerical method is semi-implicit second order difference method, where operator splitting was used to handle the linear terms with the 2[nd]

order backward difference formula (BDF-2) and the nonlinear terms with the 2nd order Adams-Bashforth (AB-2) explicit method. Spatially the viscous terms were approximated with the 2nd order central difference (CD-2) method, an adaptive upwind-downwind scheme is used to approximate the convective terms, and the Laplacian in the Poisson problem is approximated with a 9-point scheme ($\propto = 1/3$) [11]. The velocity and pressure components are solved for on a fully staggered grid, also known as a Marker And Cell (MAC) scheme, Fig 2 bc.

The first step of Chorin's projection method is to solve for the intermediate fluid velocity without the added forcing term:

$$\frac{u_i^* - u_i^n}{\Delta t} = \frac{1}{Re}\frac{\partial^2 u_i^n}{\partial x_j \partial x_j} - \frac{\partial (u_i u_j)^n}{\partial x_j} \quad (8)$$

where u_i^* is the intermediate fluid velocity, and is notably not divergence free. As mentioned previously this is solved in two steps: linear and nonlinear terms. The second step is to solve for the forcing term, which done by first interpolating the intermediate fluid velocity onto the Lagrangian nodes:

$$U_l^* = \sum_{ij} u_{ij}^* \delta_d (x_{ij} - X_l^n) \Delta x \Delta y \quad (9)$$

where capital letters represent values on the Lagrangian grid, and δ_d is the Dirac delta function, Fig 2a,b.

The forcing term on the Lagrangian nodes is then computed:

$$F_l^{n+1/2} = \frac{U_p(X_l^n) - U_l^*}{\Delta t} \quad (10)$$

where $U_p(X_l^n)$ is the velocity of the particle node, which includes both translational and rotational velocity. Equ 10 handles both the no slip and no penetration boundary conditions. Finally, the forcing term is interpolated back onto the cartesian grid:

$$f_{ij}^{n+1/2} = \sum_l F_l^{n+1/2} \delta_d (x_{ij} - X_l^n) \Delta V_l \quad (11)$$

where ΔV_l is the volume of the Lagrangian grid cells, Fig 2c. The third step is to update the intermediate velocity to account for the forcing term:

$$\frac{u_i^{**} - u_i^*}{\Delta t} = f^{n+1/2} \quad (12)$$

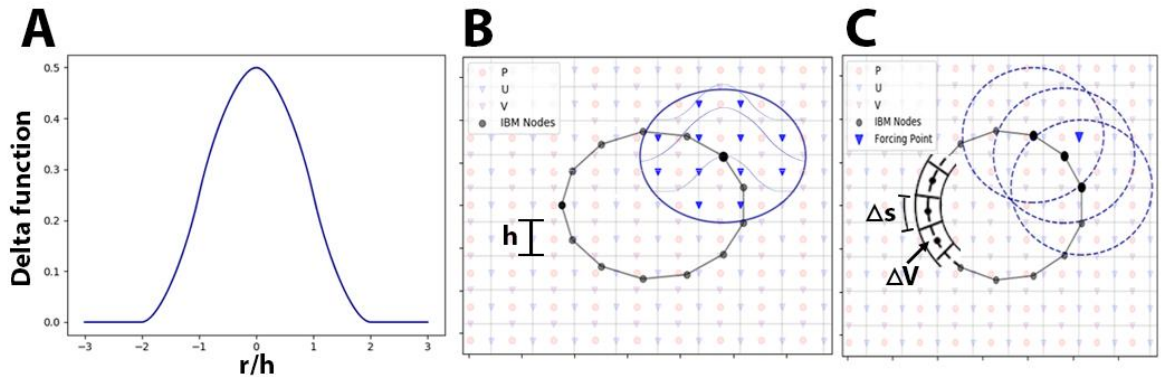

Figure 4.2. Interpolation Between Eulerian and Lagrangian Grid. The immersed boundary method utilized two independent grids to resolve the fluid-surface interface. A method for interpolating between the fully staggered Eulerian grid and the Lagrangian grid is achieved utilizing IBM. (A) The 4-point Dirac delta function the kernel is used to interpolate between the grids. (B) The interpolation of the intermediate fluid velocity onto the Lagrangian nodes. Dark blue triangles are the intermediate U-velocity nodes, which are known and used to find the intermediate fluid U-velocity at the Lagrangian node (large black dot), Equ 9. The Lagrangian forcing term is then found to impose the no-slip boundary conditions, Equ 10. (C) The spreading of the forcing term from the Lagrangian nodes onto the Eulerian nodes. The forcing term from each of the neighboring Lagrangian nodes (large black nodes) are interpolated onto the Eulerian node (dark blue triangle), Equ 11. Each node has a discrete volume, ΔV, associated with it such that the collection of nodes form a thin shell around the particle.

In the fourth step, the projection function is solved:

$$-\frac{\partial^2 p^{n+1}}{\partial x_j \partial x_j} = \left(\frac{\partial u_j^*}{\partial x_j}\right)\frac{1}{\Delta t} \tag{13}$$

In the final step, the approximated pressure is used to update the divergence free velocity at the n+1 step:

$$\frac{u_i^{n+1} - u_i^{**}}{\Delta t} = \; -\frac{\partial p^{n+1}}{\partial x_i} \tag{14}$$

After solving for the velocity and pressure of the fluid domain at the next time point, the position of the particle needs to be updated. Utilizing Cauchy's principle for hydrodynamic force and torque:

$$\oint_{\partial V} \tau * n da = -\int_V \; f dx + \frac{d}{dt}\int_V \; u dx \tag{15}$$

$$\oint_{\partial V} r \; x \; (\tau * n) da = -\int_V \; r \; x \; f dx + \frac{d}{dt}\int_V \; (r \; x \; u) dx \tag{16}$$

Equs 5 and 6 are finally modified in terms of the forcing term,

$$(\rho_p - \rho_f) V_p \frac{du_p}{dt} = -\rho_f \sum_{l=1}^{N_l} F_l^{n+1/2} \Delta V_l + F_c^{n+1/2} \tag{17}$$

$$I_p \frac{d\omega_c}{dt} = -\rho_f \sum_{l=1}^{N_l} r_l^n \, x \, F_l^{n+1/2} \Delta V_l + T_c^{n+1/2} \quad (18)$$

Second Order Accurate Immersed Boundary Method

The direct-forcing IBM does not directly enforce the no-slip/no-penetration boundary conditions on the IBM nodes, but through the body force term *f* introduced after the discretization of Navier-Stokes equations, Equ 7. Although, this method benefits from a diffuse distribution of the forcing term, it may not impose the accurately. By implementing the multidirect forcing scheme the boundary condition $u_i^{**} \approx U_p$, with a required accuracy [5, 12]. The multidirect forcing scheme proposed by Luo et al. [12] included the iterative algorithm:

$$U_l^{**,m} = \sum_{ij} u_{ij}^{**,m-1} \delta_d\left(x_{ij} - X_l^n\right) \Delta x \Delta y \quad (19)$$

$$F_l^{n+1/2,m} = F_l^{n+1/2,m-1} + \frac{U_p(X_l^n) - U_l^{**,m}}{\Delta t} \quad (20)$$

$$f_{ij}^{n+1/2,m} = \sum_l F_l^{n+1/2,m} \delta_d\left(x_{ij} - X_l^n\right) \Delta V_l \quad (21)$$

$$\frac{u_i^{**,m} - u_i^*}{\Delta t} = f^{n+1/2,m} \quad (22)$$

where the equations are indexed by m for a total number of iterations of Nm. Following the work of Breugem et al. the solver is upgraded with the three-step Runge-Kutta, and a higher order accurate pressure increment method [5, 13]. For a single time step:

for q = 0:3

$$u_i^* = u_i^n + \frac{\propto_q \Delta t}{\rho_f}\left[-\nabla p^{q-1/2} + \frac{1}{Re}\frac{\partial^2 u_i^n}{\partial x_j \partial x_j} - \frac{\partial (u_i u_j)^n}{\partial x_j}\right] + \frac{\beta_q \Delta t}{\rho_f}\left[-\nabla p^{q-1/2} + \frac{1}{Re}\frac{\partial^2 u_i^{n-1}}{\partial x_j \partial x_j} - \frac{\partial (u_i u_j)^{n-1}}{\partial x_j}\right] \quad (23)$$

$$U_l^* = \sum_{ij} u_{ij}^* \delta_d\left(x_{ij} - X_l^q\right) \Delta x \Delta y \quad (24)$$

$$F_l^{q+1/2,0} = \frac{U_p(X_l^q) - U_l^*}{\Delta t} \quad (25)$$

$$f_{ij}^{q+1/2,0} = \sum_l F_l^{q+1/2,0} \delta_d\left(x_{ij} - X_l^q\right) \Delta V_l \quad (26)$$

$$u_i^{**,0} = u_i^* + \Delta t f^{q+1/2,0} \quad (27)$$

for m = 0:Nm

$$U_l^{**,m} = \sum_{ij} u_{ij}^{**,m} \delta_d\left(x_{ij} - X_l^q\right) \Delta x \Delta y \quad (28)$$

$$F_l^{q+1/2,m} = F_l^{q+1/2,m-1} + \frac{U_p(X_l^q) - U_l^{**,m}}{\Delta t} \quad (29)$$

$$f_{ij}^{q+1/2,m} = \sum_l F_l^{q+1/2,m} \delta_d(x_{ij} - X_l^q) \Delta V_l \quad (30)$$

$$u_i^{**,m} = u_i^* + \Delta t f^{q+1/2,m} \quad (31)$$

end

$$-\frac{\partial^2 \phi^{q+1/2}}{\partial x_j \partial x_j} = \left(\frac{\partial u_j^{**,Nm}}{\partial x_j}\right) \frac{\rho_f}{(\propto_q + \beta_q)\Delta t} \quad (32)$$

$$\frac{u_i^{q+1} - u_i^{**,Nm}}{\Delta t} = -\frac{(\propto_q + \beta_q)}{\rho_f} \frac{\partial \phi^{n+1}}{\partial x_i} \quad (33)$$

$$p^{q+1/2} = p^{q-1/2} + \phi^{q+1/2} \quad (34)$$

end

where $\propto_q = [32/60, 25/60, 45/60]$, $\beta_q = [0, -17/60, -25/60]$, and ϕ is the pseudo incremental pressure.

Collisions were modeled using a short ranged repulsive force, based on the work of Glowinski et. al [14, 15].

$$F_{c,P1}^{n+1/2} \begin{cases} 0 \; if \; |\vec{\gamma}_{P1,2}| > 2R_P + \Delta r_c, \\ \kappa_c \left(\frac{2R + \Delta r_c - \vec{\gamma}_{P1,2}}{\Delta r_c}\right)^2 \frac{\vec{\gamma}_{P1,2}}{|\vec{\gamma}_{P1,2}|} \; if \; 2R_P < |\vec{\gamma}_{P1,2}| < 2R_P + \Delta r_c, \\ \kappa_c \left(\frac{2R + \Delta r_c - \vec{\gamma}_{P1,2}}{\Delta r_c}\right)^4 \frac{\vec{\gamma}_{P1,2}}{|\vec{\gamma}_{P1,2}|} \; if \; |\vec{\gamma}_{P1,2}| < 2R_P \end{cases} \quad (17)$$

where $\vec{\gamma}_{P1,2} = \vec{X}_{P1} - \vec{X}_{P2}$, Δr_c is the threshold distance for the repulsive force, and $\kappa_c = \rho_p V_p |g|$.

4.3 Results

4.3.1 Model Verification

To verify the accuracy of the computational model, the model was compared to experimental data of increasing complexity. The accuracy of the numerical scheme solving for the Navier-Stokes equation was first verified by comparing the model to experimental data for the lid driven flow in a square cavity for Reynolds number of 100, 400, and 1000, Fig 3a. Cross-sections of fluid velocity predicted by the model were compared to Ghia et. al [16] resulting in an average relative error of 0.802%. The accuracy of the IBM was then evaluated by comparing the model to another classical problem in fluid mechanics, flow past a stationary cylinder modeled with IBM mesh, Fig 3b. For mid-range Re, from 10 to 100, steady vortices downstream of the cylinder were formed. Experimental data for the structure of the steady vortices were compared to model predictions with

an average relative error of 4.139%. These steady vortices become unsteady at higher Re which transitioned to unsteady von Karmann vortices for higher Re. The vortex shedding creates oscillations in lift and drag forces on the cylinder, Fig 3c. Finally, the coefficient of drag for the cylinder was compared to experimental data over varying Re. The model predicted the coefficient of drag on a cylinder for Re = 0.1, 1, 10, 30, 120, and 1000 with an average relative error of 3.016%, Fig 3d (red dots).

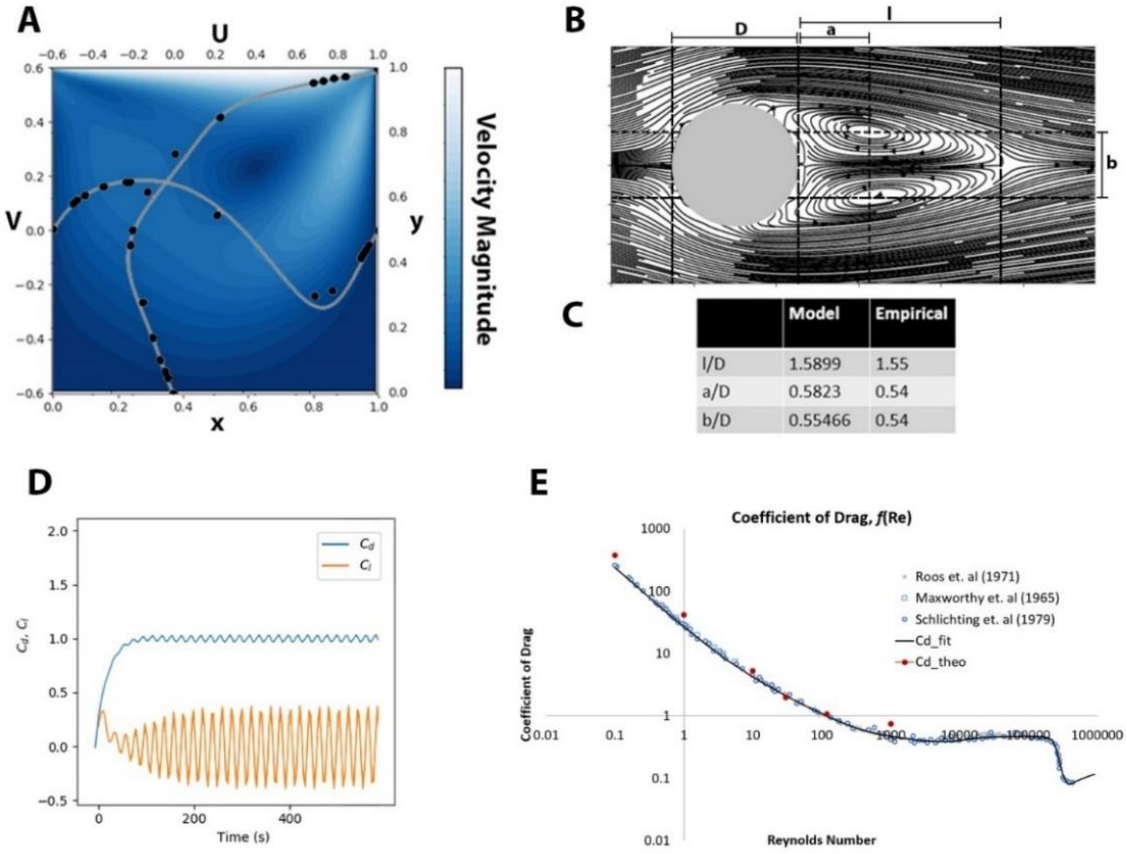

Figure 4.3. Model Verification. (A) Results from Ghia et. al [16] (black dots) are compared to the model predicted for fluid velocity across mid-sections (grey lines) for the lid driven cavity flow. Normalized velocity magnitude is plotted as a contour plot. (B) Pseudo streamlines for the flow over a cylinder with Re=30 and definitions of structural parameters of the steady vortices. (C) Comparison of experimental data [17] for the flow over a cylinder with predicted values from the model. (D) Coefficient of lift and drag for the flow over a cylinder at a Re of 100. (E) Comparison of experimental data to model predicted values for the coefficient of drag for varying Re.

The accuracy of the algorithm developed for the quantification of the velocity field within the microfluidics chips as well as the experimental error were evaluated through the comparison

to synthetic image pairs and the analytical solution for channel flow. The PIV/PSV algorithm was first used to quantify the velocity field for synthetic images for linear and vortical flow, with an average error of 0.04995 pixels/frame. The experimental error was then quantified by comparing the known analytical solution for the flow through a 50 μm channel with velocity field for 1 μm beads, quantified with the PIV/PSV algorithm. The average absolute error was found to be 25.546%, which was within the standard deviation, Fig 4.

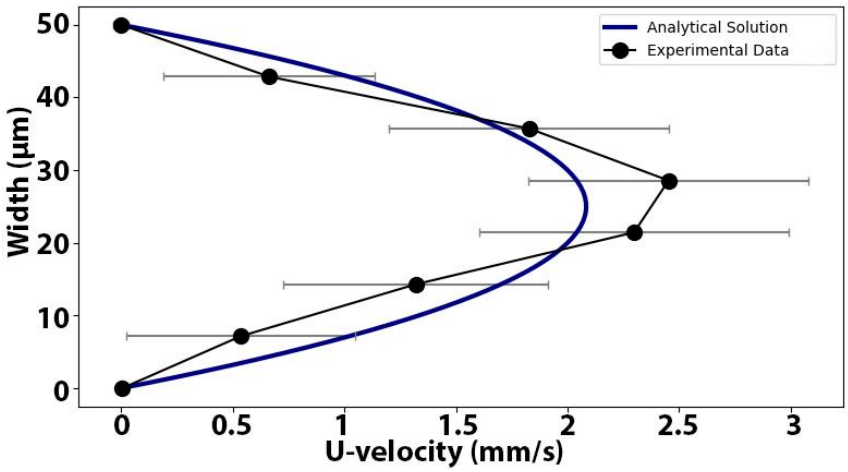

Figure 4.4. Experimental Error and PIV/PSV Verification. Comparison of analytical solution for flow through a 50 μm channel (navy line) with the velocity of 1 μm beads (black dots), quantified with the PIV/PSV algorithm.

4.3.2 Inertial Focusing

With both the accuracy of the numerical methods for solving the acceleration of the fluid and solid phases as well as the PIV/PSV algorithm verified, the model was used to predict the inertial focusing of particles. Experimental data was collected for the migration of 7.32 μm particles, in a straight 50 μm wide PDMS channel (blockage ratio of 0.146), into two beams of particles off the side of the walls. Images were collected every 500 μm downstream of the inlet with short and long exposure to monitor the distribution of particles along the width of the channel (W), as well as their velocities, Fig 5a,b.

Cross sections of the fluorescent streak images, Fig 5b, were analyzed to quantify the radial distribution of particles across the width of the channel, Fig 5c. Model predictions for the distribution of particles along the width of the channel were compared to the experimental data.

The model predicted the final equilibrium position of the particles at 0.120 y/W from the wall, Fig 5d. Experimental data found the particles migrating to a stable equilibrium position of 0.1255 y/W, which is in agreement with the previously measured equilibrium position of 0.125 y/W [18]. The relative error in the model prediction of 4%, or 0.025 µm was well within in the standard deviation of the experimental data of 2.5 µm.

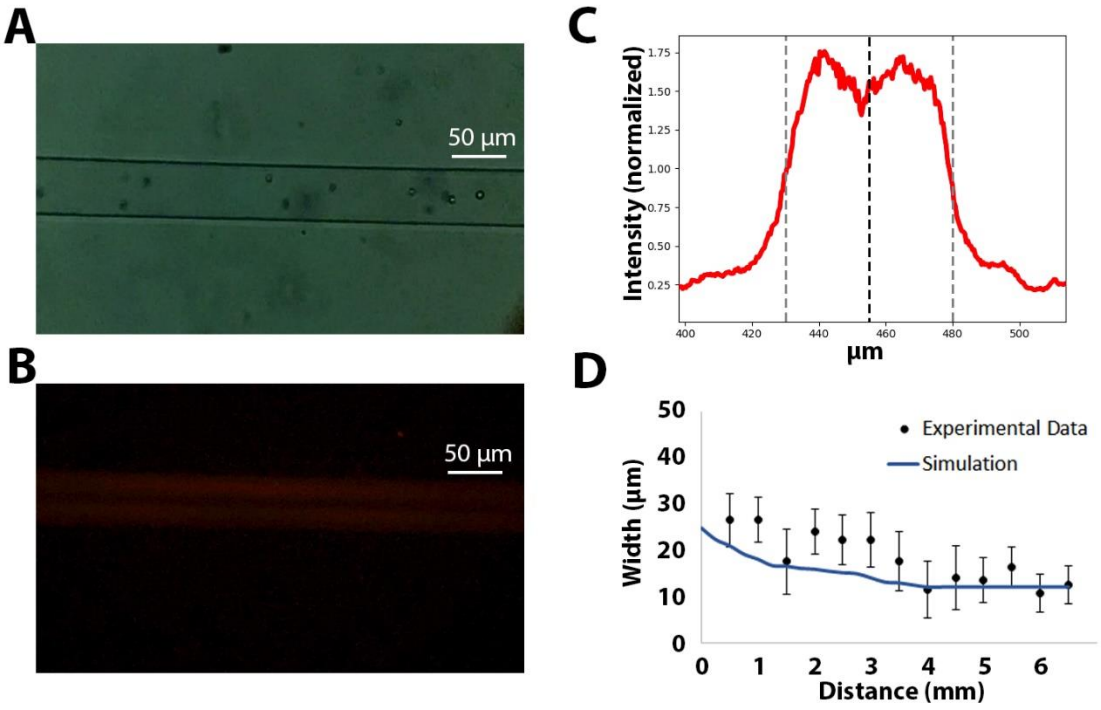

Figure 4.5. Particle Migration Across Streamlines. (A) Brightfield image of 50 µm channel with 7.32 µm beads. (B) Fluorescents of the 7.32 µm beads at a Re of 20 and an exposure of 1/10 s. (C) Example cross section of fluorescence normalized to FWHM (red line), 1 mm downstream of the inlet. Approximate wall positions and centerline are depicted by dashed grey lines and a dashed black line, respectively (D) Experimental data (black dots) for the average radial position of particles downstream of the inlet compared to predicted results from IBM simulations (navy line).

4.3.3 Particle Capture

Experimental data for motion of 7.32 and 20 µm beads were collected for varying Re to quantify the size selective capture of particles as a function of well geometry and Re. The velocity fields of the 7.32 µm beads through the expanded channel microfluidics device for a Re of 5 and 120 were quantified using the PIV/PSV algorithm, Fig 6a-d. The particle velocity across the entire

channel/well at the centerline was compared to the numerical simulation for the fluid velocity profile, Fig 6e-f. For the higher Reynolds flow the algorithm was unable to detect the streaks in the channel due to their low signal to noise ratio, Fig 6f. However, however the algorithm did quantify the velocity of the particles entering the low Reynolds vortex from the higher Reynolds channel flow, Fig 6f (red circle).

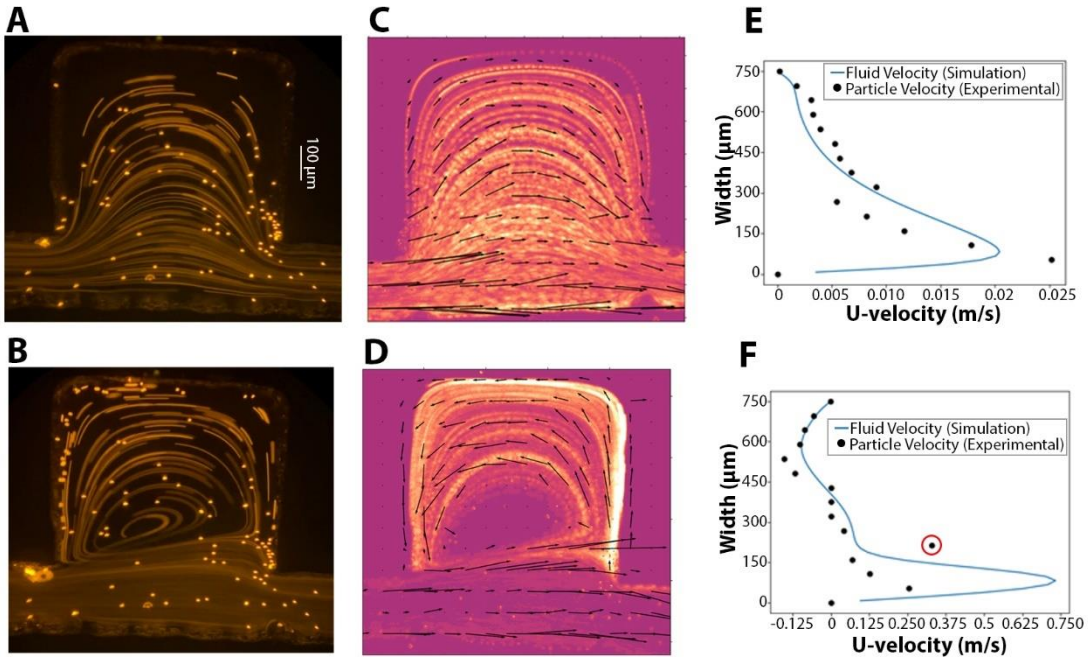

Figure 4.6. Particle Capture in Microvortices. (A) Long exposure images of 7.32 µm beads for Re = 5, and (B) Re = 120. (C) Short exposure images were then used to collect PIV/PSV Data for Re = 5 and (D) Re = 120. (E) Comparison of u-velocity of mid-slice of PIV/PSV data (black dots) and model predictions (blue line) for Re = 5 and (F) Re = 120. Notably the difference between the data point circled in red and the model predictions for the fluid velocity is the inertia of the particle that keeps the particle moving rapidly as it enters the well before it decelerates.

Numerical simulations were also compared to experimental data collected by Papautsky et al. [1], for the size selective trapping of microparticles. Simulations showed the size selective trapping of 20 µm beads for both 300x300 µm (Fig 7a), and 400x400 µm (Fig 7b) wells. The experimental data for the instantaneous position of 20 µm (blue xs) and 7.32 µm (grey xs) beads [1] were overlayed with simulation predictions for the motion of 20 µm (blue dots) and 7.32 µm (black dots), Fig 7b.

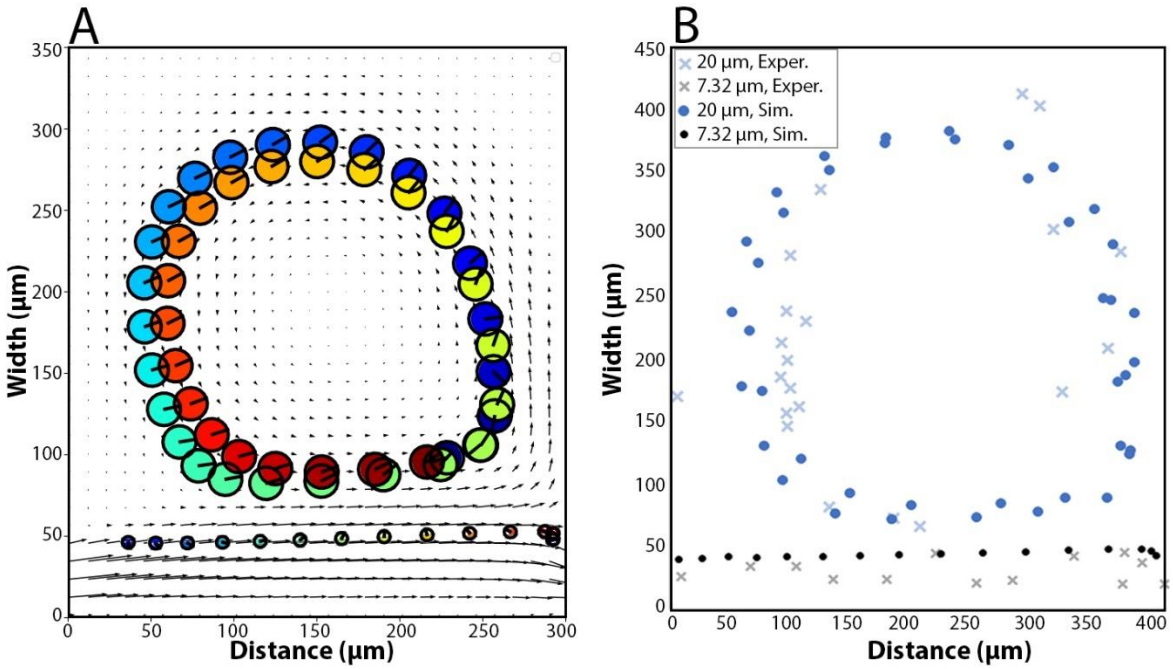

Figure 4.7. Size Selective Capture. (A) Model simulations for the size selective capture of 20 µm particles, while the 7.32 µm particles pass the 300x300 µm well without entering, Re = 135. The particle color represents normalized time from navy to maroon, which are plotted over a quiver plot of the fluid velocity field. (B) Comparison of experimental data for the instantaneous position of 7.32 µm (grey xs) and 20 µm (blue xs) particles, collected by Papautsky et. al [1], to simulation results for motion of 7.32 µm (black dots) and 20 µm (blue dots) particles.

Papautsky et al. reported that the size selective capture of particles within the microvortices was also Reynolds number dependent. To characterize the Reynolds number dependent capture of the 7.32 µm particles in a 300x300 µm experimental data was collected for Re = 5, 100, and 200 with the characteristic length of the channel width, Fig 8d-g. The experimental data was then compared to model predictions, Fig8 a-c, both of which found that at Re 200 the particles collided with the downstream wall of the well and entered the well on the outmost streamlines, Fig 8c,g. This is in agreement with the results from Papautsky et al. who observed 7.32 µm particles entering the microvortices at Re 215 [1].

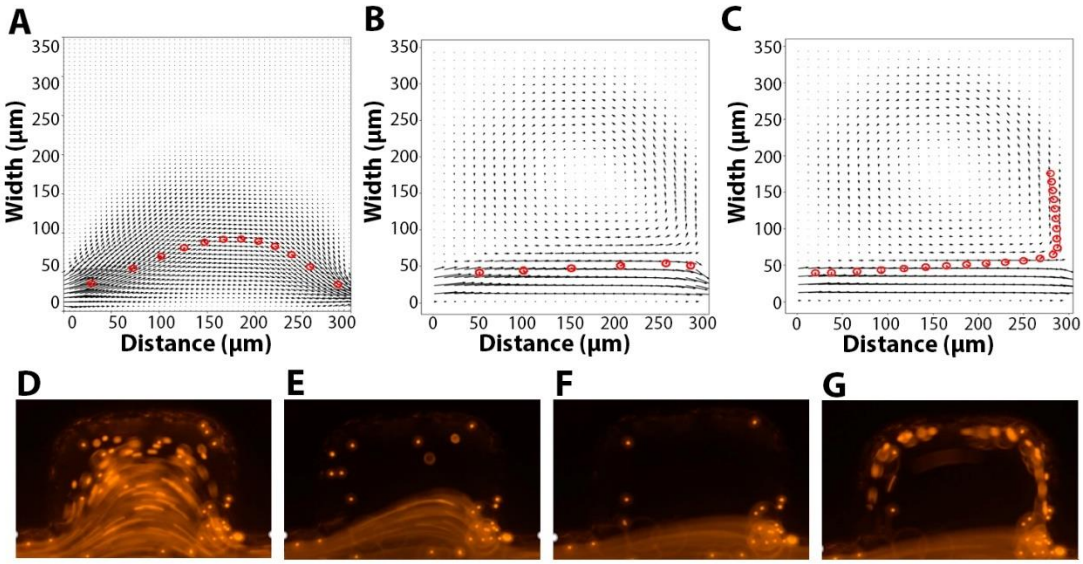

Figure 4.8. Re Dependent Particle Capture. (A-C) Model simulations for the Re dependent capture of 7.32 µm particles for (A) Re = 5, (B) Re = 100, and (C) Re = 200. The 7.32 µm particles are plotted in red over a quiver plot of the fluid velocity field. (D-F) Fluorescent streak images of the 7.32 µm particles for (D) Re = 5, (E) Re = 100, and (F-G) Re = 200. The fluorescent streak image in (G) was taken a few seconds after (F) and shows the collision of a few fluorescent particles with the side of the well and their subsequent entry into the well.

4.4 Discussion

4.4.1 Error in PIV/PSV Algorithm

The PIV/PSV algorithm was able to quantify the displacement of particles in rotational flow with subpixel accuracy, for synthetic images. However, the quantified experimental data for the flow through a rectangular channel was compared to the analytical solution with an average absolute error of 25.546%. This error is likely experimental error and will be corrected with more rigorous protocols for experimental data collection.

The algorithm performed well for quantifying the particles velocities within both the low and high Reynolds flow of the expanded channel microfluidics devices. Although the algorithm accurately quantified the motion of particles in the entire system for Re = 5, the algorithm could only accurately quantify the velocity of particles within and entering the well for Re = 120 and 360, Fig 6. Inside the channel (Re = 120 and 360) the particle velocity was too great for the particle streaks to be detected over the background noise, Fig 6f.

4.4.2 Microfluidics Device Fabrication

The current method of fabrication for the expanded chip design relies on a laser cutter to etch the design. This not only produces rough boundaries that will likely affect the inertial focusing of the particles, but also limits the channel size to >150μm which is too large to observe inertial focusing of 7.32μm. This limits the application of the chip design to either capturing 7.32μm beads with a larger well or only capturing 20μm beads. To increase the resolution of the well microfluidics chip, the design will be fabricated using standard photolithography in the same way the straight chip design was fabricated.

4.4.3 Microfluidics Device Optimization

With the model able to predict the inertial focusing of the particles, as well as the development of microvortices at varying Re, the model will be used to aid in the design and optimization of the well microfluidics devices. Utilizing IBM any type of well geometry can be modeled as well as allow for the modeling of elastic, deformable cells. These simulations can be used to evaluate the rate of particle drift, which is directly related to their size and deformability. The opening of the well can then be modified to increase or decrease the amount of time the particles spend moving past the opening, thus allowing, or preventing a size specific particle from drifting into the well and becoming captured. The shape of the well can also be modified to modulate the strength of the vortices to aid in particle retention.

4.4.4 Biomedical Engineering Applications

Size selective capturing has numerous applications for filtering biological samples. The filtration of cancerous cells out of the blood stream for analysis is a practical use of these chip designs as the larger cancerous cells will experience a larger shear force and become captured in the wells much more readily than red blood cells [2]. Inertial focusing is also greatly influenced by deformability of the particle; increased deformability shifts the focusing of the particle towards the centerline. This could be taken advantage of by filtering out malaria infected red blood cells, which become rigid during the incubation of the viral infection.

4.5 Conclusion

Utilizing continuous and direct forcing immersed boundary methods we developed a model that accurately simulates the inertial focusing of particles. The model was then expanded to model the expansion of the channel with IBM and simulate the capture of 7.32 μm particles within the wells. Future work will aim at utilizing the developed IBM model to optimize the geometry to enhance size selectivity and efficiency of the particle capture. The model will also be expanded to account for deformable and rigid cells.

4.6 References

[1] J. Zhou, S. Kasper, and I. Papautsky, "Enhanced size-dependent trapping of particles using microvortices," *Microfluid Nanofluidics,* vol. 15, no. 5, pp. 611-623, 2013, doi: 10.1007/s10404-013-1176-y.

[2] S. C. Hur, A. J. Mach, and D. Di Carlo, "High-throughput size-based rare cell enrichment using microscale vortices," *Biomicrofluidics,* vol. 5, no. 2, pp. 022206-022206-10, 2011, doi: 10.1063/1.3576780.

[3] A. J. Mach and D. Di Carlo, "Continuous scalable blood filtration device using inertial microfluidics," *Biotechnol. Bioeng,* vol. 107, no. 2, pp. 302-311, 2010, doi: 10.1002/bit.22833.

[4] G. SegrÉ and A. Silberberg, "Radial Particle Displacements in Poiseuille Flow of Suspensions," *Nature (London),* vol. 189, no. 4760, pp. 209-210, 1961, doi: 10.1038/189209a0.

[5] W.-P. Breugem, "A second-order accurate immersed boundary method for fully resolved simulations of particle-laden flows," *Journal of computational physics,* vol. 231, no. 13, pp. 4469-4498, 2012, doi: 10.1016/j.jcp.2012.02.026.

[6] J. Lee and D. You, "An implicit ghost-cell immersed boundary method for simulations of moving body problems with control of spurious force oscillations," *Journal of computational physics,* vol. 233, pp. 295-314, 2013, doi: 10.1016/j.jcp.2012.08.044.

[7] A. Gronskis and G. Artana, "A simple and efficient direct forcing immersed boundary method combined with a high order compact scheme for simulating flows with moving rigid boundaries," *Computers & fluids,* vol. 124, pp. 86-104, 2016, doi: 10.1016/j.compfluid.2015.10.016.

[8] J. Yang and F. Stern, "A simple and efficient direct forcing immersed boundary framework for fluid–structure interactions," *Journal of computational physics,* vol. 231, no. 15, pp. 5029-5061, 2012, doi: 10.1016/j.jcp.2012.04.012.

[9] A. M. Roma, C. S. Peskin, and M. J. Berger, "An Adaptive Version of the Immersed Boundary Method," *Journal of computational physics,* vol. 153, no. 2, pp. 509-534, 1999, doi: 10.1006/jcph.1999.6293.

[10] M. Uhlmann, "An immersed boundary method with direct forcing for the simulation of particulate flows," *Journal of computational physics,* vol. 209, no. 2, pp. 448-476, 2005, doi: 10.1016/j.jcp.2005.03.017.

[11] R. Lynch, "Fundamental Solutions of 9-point Discrete Laplacians; Derivation and Tables," ed. Purdue e-Pubs, 1992.

[12] K. Luo, Z. Wang, J. Fan, and K. Cen, "Full-scale solutions to particle-laden flows: Multidirect forcing and immersed boundary method," *Phys Rev E Stat Nonlin Soft Matter Phys,* vol. 76, no. 6 Pt 2, pp. 066709-066709, 2007, doi: 10.1103/PhysRevE.76.066709.

[13] W. E and J.-G. Liu, "Projection Method I: Convergence and Numerical Boundary Layers," *SIAM journal on numerical analysis,* vol. 32, no. 4, pp. 1017-1057, 1995, doi: 10.1137/0732047.

[14] R. Glowinski, T. W. Pan, T. I. Hesla, D. D. Joseph, and J. Périaux, "A Fictitious Domain Approach to the Direct Numerical Simulation of Incompressible Viscous Flow past Moving Rigid Bodies: Application to Particulate Flow," *Journal of computational physics,* vol. 169, no. 2, pp. 363-426, 2001, doi: 10.1006/jcph.2000.6542.

[15] M. H. Abdol Azis, F. Evrard, and B. van Wachem, "An immersed boundary method for flows with dense particle suspensions," *Acta mechanica,* vol. 230, no. 2, pp. 485-515, 2019, doi: 10.1007/s00707-018-2296-y.

[16] U. Ghia, K. N. Ghia, and C. T. Shin, "High-Re solutions for incompressible flow using the Navier-Stokes equations and a multigrid method," *Journal of computational physics,* vol. 48, no. 3, pp. 387-411, 1982, doi: 10.1016/0021-9991(82)90058-4.

[17] M. Coutanceau and R. Bouard, "Experimental determination of the main features of the viscous flow in the wake of a circular cylinder in uniform translation. Part 2. Unsteady flow," *J. Fluid Mech,* vol. 79, no. 2, pp. 257-272, 1977, doi: 10.1017/S0022112077000147.

[18] J. Zhou and I. Papautsky, "Fundamentals of inertial focusing in microchannels," *Lab Chip,* vol. 13, no. 6, pp. 1121-1132, 2013, doi: 10.1039/c2lc41248a.

5. CONCLUSION

In this thesis, we explored the application of mathematical and computational modeling to three different systems in biomedical engineering: neuronal protein interactions, drug release from unconventional drug delivery devices, and the migration of particles in inertial microfluidics channels. Each application of computational modeling expanded the understanding of the system and offered a new tool to further investigate variations in the system.

5.1 Contributions

5.1.1 Neuronal synapse model

Our computational model for the interaction of key synaptic proteins involved in learning and memory was able to fully capture the calcium dependent response of the system. The model then successfully described the reaction of the system to a SYNGAP1 loss-of-function mutation, which resulted in an oversaturation of TARP anchored at the PSD. Ultimately, the model produced valuable insight into the behavior of the system and the dynamic inhibitory role that synGAP plays. The model also proved to be a useful tool in suggesting potential drug targets that could restore the bidirectionality of the system.

5.1.2 Bioresorbable drug delivery depot model:

The mathematical and computational model for the drug release rate from drug delivery depot was able to accurately predict the drug release rate from three different bioresorbable depots for a sweep of polymer molecular weights. Including both the amount drug lost in the solidification process of the phase inversion, as well as the drug released due to polymer degradation. This model deepened the understanding of the importance acidic byproducts and all four modes of degradation on the system. The model also offers a valuable tool for the rational design of drug delivery devices to meet patient specific need.

5.1.3 Inertial microfluidics model:

Our computational models for the migration of particles within inertial microfluidics devices were able to accurately simulate the motion of particles of varying size within devices of varying geometry. The model accurately predicted the inertial focusing of the particles with an error of less than a micron, the size selective capture of particles within a 400x400 μm well, and the Reynolds number dependent capture 7.32 μm particles. This model offers a tool for the design optimization of inertial microfluidics devices, for a variety of size selective processes. The model will be used to optimize the capture efficiency of circulating tumor cells or malaria infected cells by varying the shape and opening of the well.

5.2 Future Work

Although this thesis developed a series of valuable computational models for exploring each of their respective systems, they ultimately create more questions and future goals than they answer. Both the blessing and curse of science.

5.2.1 Neuronal synapse model

The current model for the post-synapse accounts for synGAP's inhibitory structural role, however, it does not account for synGAP's role in the ERK pathway. SynGAP's signaling pathway has been experimentally determined to be necessary for neuronal plasticity [1]. Experimental data has also observed the migration of critical synaptic proteins: synGAP, AMPAR, and CaMKII in and out of the synapse [2, 3], which will be a crucial component of the next model iteration. This will also require modeling the endocytosis/exocytosis of AMPAR to the PSD, and relevant proteins. Lastly, the applicability of the model could be dramatically increased with the inclusion of an electrophysiological model of the AMPAR- and NMDAR-gated currents.

5.2.2 Bioresorbable drug delivery depot model:

The accuracy of the model could be significantly increased by collecting data on the diffusion of a variety of drugs out of a variety of polymer molecular weights, to further characterize the relationship. The current model also required that both the geometry of the fully solidified polymer, and the initial drug distribution to be known. To increase the applicability of the model the

solidification model will be increased in complexity to accurately simulate the phase inversion of the implant and predict the final geometry and drug distribution.

5.2.3 *Inertial microfluidics model:*

The spatial resolution of the microfluidics devices will be greatly improved by utilizing standard photolithography for all the chip designs. With a higher resolution for the fabrication of microfluidics chips a larger variety of chips designs could be produced, and aid in the better design of these devices. With the computational model well validated it can be used as a tool for design optimization by running numerous variations in the microfluidics chip design. To model more complicated well geometries immersed boundary methods will be employed to model the walls of the microfluidics device. The immersed boundary method can also be used to model the material properties of cells and capture the impact of deformability on inertial focusing. The filtering out of malaria infected RBCs and circulating tumor cells out of a blood sample is an ideal target for the future model iterations.

5.3 References

[1] L. E. Vazquez, H.-J. Chen, I. Sokolova, I. Knuesel, and M. B. Kennedy, "SynGAP Regulates Spine Formation," *J Neurosci,* vol. 24, no. 40, pp. 8862-8872, 2004, doi: 10.1523/JNEUROSCI.3213-04.2004.

[2] Y. Araki, M. Zeng, M. Zhang, and Richard L. Huganir, "Rapid Dispersion of SynGAP from Synaptic Spines Triggers AMPA Receptor Insertion and Spine Enlargement during LTP," *Neuron,* vol. 85, no. 1, pp. 173-189, 2015, doi: 10.1016/j.neuron.2014.12.023.

[3] K. Obashi, J. W. Taraska, and S. Okabe, "The role of molecular diffusion within dendritic spines in synaptic function," *J Gen Physiol*, vol. 153, no. 4, 2021, doi: 10.1085/jgp.202012814.